Low Order Modeling of Load Distribution and Friction in Ball Bearings and Ball Screws – with Application to Electric Power Assisted Steering

by

Bo Lin

A dissertation submitted in partial fulfillment
of the requirements for the degree of
Doctor of Philosophy
(Mechanical Engineering)
in the University of Michigan
2019

Doctoral Committee:

Associate Professor Chinedum E. Okwudire, Chair
Professor James R. Barber
Professor Judy Jin
Dr. Jason S. Wou

Bo Lin

bolin@umich.edu

ORCID iD: 0000-0001-5163-5856

To my parents and brother who always support me.

Acknowledgements

Pursuing the doctoral degree may be the most important decision I have made in my life and the five years at the University of Michigan have certainly shaped who I am today. I sincerely appreciate the help and support I got from so many wonderful people. Here I would like to express my gratitude to all of them.

First of all, I want to thank my advisor, Prof. Chinedum Okwudire, who guided me through my Ph.D. study. Without his patience and encouragement, I would not be able to accomplish it. From him, I learned to always keep the curiosity and passion for research, the optimism and perseverance to overcome obstacles. He is not only an outstanding researcher and a supportive advisor, but also an enthusiastic teacher and a caring friend. It has been a great honor for me to work with him and learned so much from him.

I would like to thank my committee members: Prof. James Barber, Prof. Judy Jin and Dr. Jason Wou for their valuable feedback and guidance. I got many good ideas for my research from the discussion with Prof. James Barber. Prof. Judy Jin also provided very constructive insight for my research. My special thanks goes to Dr. Jason Wou, not only for his input into the research project from the industrial perspective, but also for his guidance and career advice. I am grateful to have worked with him closely.

I also want to thank the collaborators from the Ford Motor Company, especially Garry Smith, Bradley Hochrein and Darin Petrini, who brought the research topic to us and supported my Ph.D. study. They introduced me into the automotive industry, in which I will start my career.

I would like to thank my friends and lab mates for their tremendous support in research and daily life. Many thanks to Molong Duan, Xingye Da, Pengcheng Zhao, Jihyun Lee, Deokkyun Yoon, Keval Ramani, Xin Dong, Nosa Edoimioya, Wami Ogunbi, Xiang Lu, Hengyi Cai, Yunli Shao, Zhenlin Wang, Wei Wu, Duanxiang Zhang, Ding Zhang, Yan Chang, Yiling Zhang, Changbai Tan, Yusen Chen, Tianqu Shao, Junhao Hu, Yuxiang Zhang and Yuan Miao.

Finally, I would like to thank my parents, brother and all the other family members for their unconditional support and endless love.

Table of Contents

List of Tables

List of Figures

List of Appendices

Abstract

Rolling ball machine components like ball bearings and ball screws are used in a wide range of machineries for load bearing and motion transmission. Ball bearings and ball screws are also the two key mechanical components in rack-type electric power assisted steering (rack EPAS) gears in motor vehicles. They are subjected to large multi-directional loads and manufacturing errors in rack EPAS, making it hard to accurately calculate load distribution (i.e., the load borne by individual balls) for the purpose of sizing. Rack EPAS gear also suffers from "stick-slip" (i.e., sticky feel sensed by the driver) mainly due to the friction variation of ball bearings and ball screws, which adversely affects driving experience. Motivated by the industrial application, the objective of this doctoral thesis is to develop low order load distribution and friction models for ball bearings and ball screws to aid analysis, optimal design and manufacturing tolerance specification of rolling ball machine components (used in EPAS).

A low order static load distribution model for ball screw is first proposed incorporating geometric errors and elastic deformation effects. A new way of describing the ball screw groove surfaces with geometric errors using multivariate functions is proposed. A ball-to-groove contact model based on Hertzian Contact Theory including geometric error effects is developed. The proposed load distribution model is validated against high order Finite Element Analysis (FEA) models created in ANSYS and is shown to be accurate but computationally much faster. It is thus applicable to ball screws with multi-directional loading and geometric errors, like those in EPAS.

Two sources of contact-induced friction variation in ball bearings and ball screws are investigated and modeled. Based on a sensitivity analysis of ball-to-groove contact friction due to rolling, sliding and spin motions, the transition between four-point contact operation and two-point contact operation is shown to give rise to significant friction variation in a four-point contact ball bearing. Another source of friction variation is ball-to-ball contact. In this work, low order numerical models for ball-to-ball contact friction in linear ball bearings and ball screws are

proposed, both of which are validated favorably against ANSYS FEA models while being computationally much faster. Based on friction analysis and simplifying approximations, an analytical model for ball-to-ball contact friction in four-point contact linear ball bearings is derived. The insights gained from the analytical model are leveraged to mitigate ball-to-ball contact and thus significantly reduce friction variation.

The developed load distribution and friction models are applied to rack EPAS gear in a few realistic scenarios and proven to be useful for industrial applications. Important insights are derived for ball bearing and ball screw design, inspection and manufacturing tolerance specification based on the developed models.

Chapter 1 Introduction and Literature Review

1.1 Background and Motivation

1.1.1 Rolling Ball Machine Elements

Rolling ball machine elements are widely used in machineries to carry load and transmit motion with low friction [1]. Figure 1.1 shows the common examples of rolling ball machine elements: (rotary) ball bearing, linear ball guide, linear ball bearing (or linear guideway) and ball screw.

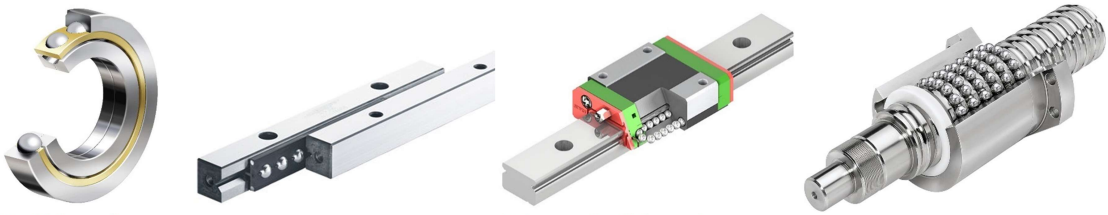

Ball bearing [SKF] | Linear ball guide [Schneeberger] | Linear ball bearing [Hiwin] | Ball screw [Hiwin]

Figure 1.1: Examples of rolling ball machine elements

Applications of rolling ball machine elements can be found in all kinds of industries such as manufacturing, energy, aerospace and automotive, to mention a few. For example, in machine tools used extensively for manufacturing, rotary ball bearings are commonly used in high-speed spindles for metal cutting [2,3]; ball screws are the key components of some machine tool feed drives that deliver the cutting tool and workpiece to the desired location [4]; linear ball bearings are indispensable components in some machine tool guides [4]. In wind turbines, ball bearings are critical parts supporting the main shaft which transmits energy from the blades and rotor to the gearbox and generator [5,6]; they are also used for pitch and yaw control of blades and nacelle (i.e., housing) to fully exploit wind resources [7]. In aircrafts, ball screws are key components of electromechanical actuators used in secondary flight controls (e.g., flaps, slats and trim horizontal stabilizers) and landing gears [8,9]. In vehicles, ball bearings are used extensively in moving parts such as wheel hubs and transmissions [10]; ball screws are the key

mechanical components in electromechanical actuators which are gaining popularity in electric power assisted steering systems, brake boosters and clutch release systems [11].

Since the main functions of rolling ball machine elements are load carrying and motion transmission, load capacity and friction behavior of rolling ball machine elements are very important to their functionality. Load distribution characterizes the load carried by each ball in the ball track, thus it predominantly determines the load capacity and service life of rolling ball machine elements [1]. In machine tools, ball bearings in the spindles are the most susceptible to damages by overload and they must be operated under the maximum allowable load [12]. In wind turbines, bearings are the predominant cause of failure due to excessive loads [6], thus their load distribution is critical and must be determined early in the design stage of wind turbines [7]. In aircrafts, the load distribution in the ball screw affects the life span of electromechanical actuators [8]. On the other hand, friction of rolling ball machine elements affects the accuracy, efficiency and motion smoothness of the machineries. In machine tools, excessive friction-induced heat in spindle bearings result in degradation in accuracy of machined parts [12]. In wind turbines, rolling bearing friction accounts for about 30% of total power loss of wind turbines, thus rolling bearing friction must be understood and compensated to reduce the overall power loss [13]. In aircrafts, the possibility of jamming in mechanical transmission components (mainly from ball screw) hinders the use of electromechanical actuators in safety-critical applications such as primary flight control [9].

1.1.2 Ball Bearings and Ball Screws in Rack Electric Power Assisted Steering (EPAS) System

Power assisted steering systems are used in the vast majority of modern vehicles to reduce driver's steering effort [14]. There are two primary types of power assisted steering systems, namely, hydraulic power assisted steering (HPAS) and electric power assisted steering (EPAS). Figure 1.2 depicts the typical HPAS and EPAS systems for passenger vehicles. Both steering systems typically have a rack and pinion mechanism that helps convert the driver's input at the steering wheel to the translational motion of the rack thus turning the road wheels. In HPAS system, the fluid pressure on either side of the hydraulic piston is differentiated by a rotary valve to provide assist force to the rack, as shown in Figure 1.2 (a). In EPAS system, however, the assist is provided by an electric motor. As depicted in Figure 1.2 (b), a torque sensor signals the electronic control unit (ECU) on when to provide assistance according to the

driver's input from the steering wheel and vehicle speed. The assist torque from the electric motor is then transmitted to assist force on the rack through the ball bearing and ball screw via timing belt. EPAS system has many advantages over HPAS system with regard to fuel efficiency, control flexibility and environmental compatibility, etc. [14,15]. Recent trends towards vehicle electrification, advanced driver-assistance system (ADAS), steer-by-wire (SbW) and autonomous driving have also facilitated the rapid adoption of EPAS compared to HPAS [14,15], mainly due to the low latency and control flexibility of electronics compared to hydraulics. In the EPAS system shown in Figure 1.2 (b), the motor sits parallel to the rack and the assist force is provided at the rack, thus it is called rack EPAS. Depending on the location of the assist motor, there are column EPAS and pinion EPAS as well. Rack EPAS systems provide the most assist force among the three types of EPAS, thus they are usually used in bigger cars [16]. They motivate the key issues studied in this dissertation and are the primary focus of its application.

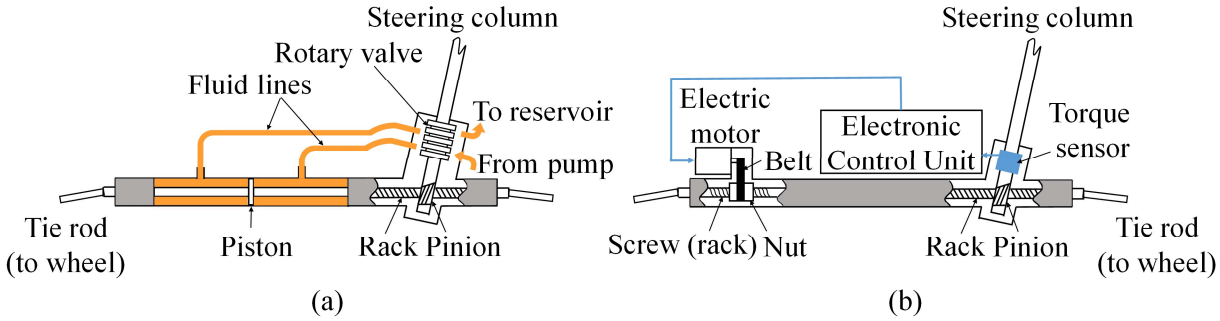

Figure 1.2: Schematics of: (a) hydraulic power assisted steering (HPAS) system; (b) electric power assisted steering (EPAS) system in passenger vehicles

Ball bearings and ball screws are key mechanical components in rack EPAS system as shown in Figure 1.3. Since steering system is safety critical [17], the rack EPAS gear must function under the high external loads to which it is subjected; it must meet certain specifications on "friction roughness" (i.e., friction variation) for smooth and safe operation. Therefore, load distribution and friction behavior of ball bearing and ball screw are important to the safety and performance of rack EPAS gear, much like they are to the afore-mentioned applications of rolling ball machine elements. The harsh operating conditions of EPAS gear in vehicles pose unique challenges: the rack (i.e., ball screw shaft) of the rack EPAS gear experiences very large multi-directional (i.e., axial and lateral) load due to large tire forces at various tie rod angles. At the same time, ball bearing and ball screw in rack EPAS gear inevitably have manufacturing errors. The manufacturing errors in EPAS gear are more pronounced than many other

applications due to the cost constraints of automotive industry. These two features of rack EPAS: large multi-directional loading and relatively large manufacturing errors, make it hard to accurately calculate the load distribution in the ball bearing and ball screw for the purpose of sizing. These two features also make the friction behavior of rack EPAS gear complicated: the rack EPAS gear is well known to suffer from "stick-slip" phenomenon (i.e., sticky feel sensed by the driver), which largely affects the user experience. "Stick-slip" is an extreme case of friction variation, mainly introduced by the ball bearing and ball screw.

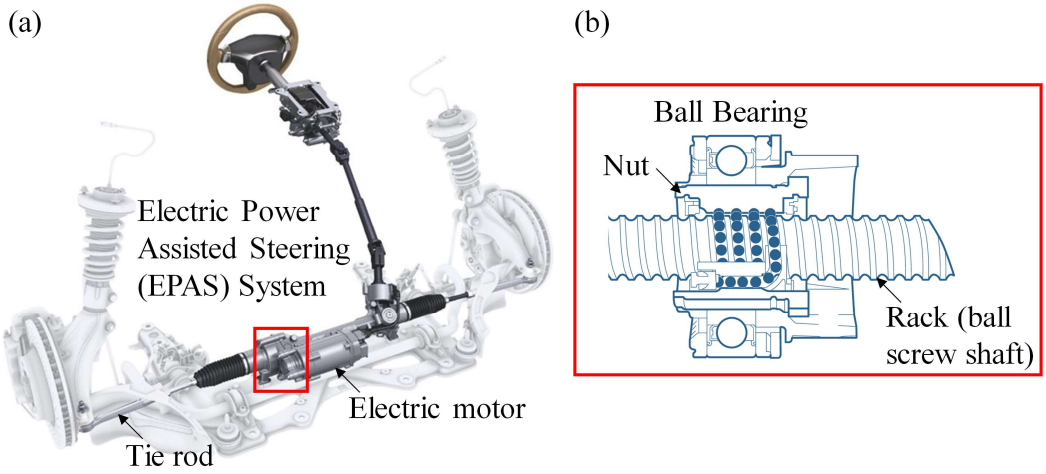

Figure 1.3: (a) Rack EPAS system [photo courtesy of Porsche]; (b) key mechanical components: ball bearing and ball screw [photo courtesy of Bosch]

Modeling load distribution and friction behavior of ball bearing and ball screw plays an important role in the design stage of rack EPAS gear by reducing the testing cost and time. It facilitates analytical design verification (or virtual experiments) of rack EPAS gear for better design, faster troubleshooting and more cost reduction. While it is true that tighter manufacturing tolerances improve the performance of ball bearing and ball screw, it comes at a cost. Therefore, it is very important, especially in the cost-sensitive automotive industry, to identify the key contributing factors in design and manufacturing tolerances for ball bearings and ball screws to ensure their load capacity and friction variation but at the same time keep the cost low. However, there is a lack of appropriate load distribution and friction models for ball bearings and ball screws, especially under the effect of manufacturing errors and multi-directional load.

Since the study is motivated by the application of ball bearings and ball screws in rack EPAS, which is low speed application, only static and quasi-static behaviors are studied. However, dynamic behavior in high speed application can be incorporated to the developed

models if necessary. Besides, the effect of manufacturing errors and multi-directional load on load distribution and friction variation is the main focus, thus the effect of other factors, such as lubricants, thermal effect are out of the scope of this dissertation.

In the next section, the literature on the load distribution and friction modeling of ball bearings and ball screws are reviewed. Based on the deficiencies identified in the literature review, the contributions of this dissertation are summarized at the end of this Chapter.

1.2 Literature Review on Load Distribution and Friction Modeling of Ball Bearings and Ball Screws

1.2.1 Load Distribution Modeling

Load distribution characterizes the load carried by each ball in rolling ball machine elements. It is essential for the load capacity and service life of machine elements [8,18,19]. Therefore, an accurate characterization of load distribution is very important for the rolling ball machine element design and sizing.

It is very difficult to measure the load distribution experimentally in rolling ball machine elements due to sensing difficulties. Biehl, et al. [20] deposited thin film sensors on the groove of a ball bearing to conduct direct contact load measurement. Even though the thickness of thin-film sensors can be made down to a few μm [20–22], it still changes the ball-to-groove interaction which is also μm-level and therefore affects load distribution. Besides, thin film sensors show temperature dependence and do not have good wear resistance; complicated process of depositing multiple layers of material on the substrate (i.e., bearing grooves) also prevents their prevailing use. Biehl, et al. [21], in another work, placed steel pins coated with thin film sensor in drilled holes inside the ball nut to measure the preload in double-nut ball screw. But unlike direct deposition on groove [20], the thin film sensor did not measure the load distribution on each ball. Apart from the attempt to directly measure load distribution, another approach is to conduct indirect (non-contact) measurement. Papadopoulos [23] presented using photoelastic experiments to study the load distribution in roller bearing specimens. Photoelasticity is the phenomenon when the material shows different fringe patterns under stress. It is based on the optical properties of transparent material, and can be utilized to determine load distribution. However, it cannot be applied to real rolling ball machine elements which are usually made of steel. Besides, it cannot be used for specimens with complex geometries such as

ball screws with helical grooves. Bertolaso, et al. [8], with the aim to measure load distribution in ball screw, had to use photoelastic experiments to measure the load distribution in a simplified 2D slice of ball screw made of PMMA (transparent plastic material), because of the pre-described limitations of photoelasticity. Such simplified set-ups grossly misrepresent the three-dimensional force–displacement interactions that take place in the actual ball screw.

Given the difficulties in experimentally measuring load distribution in rolling ball machine elements, most researchers have resorted to models to predict load distribution. Such models could take the form of empirical models. However, empirical models are only available for few simple load cases such as pure axial loading [24]. The empirical models are not accurate either under multi-directional loading condition or when manufacturing errors are present. A more versatile approach is to use high-order 3D finite element (FE) models, often generated using commercial Finite Element Analysis (FEA) software like ANSYS® and Abaqus. Since the scale of contact deformation is μm-level while the dimension of machine elements are mm-level, mesh refinement must be made near the contact region to attain reasonable accuracy and resolution [18,19,25]. As a result, high-order 3D FEA models often have to be very large, consisting of hundreds of thousands of elements and degrees-of-freedom (DOFs) [25]. They consume a lot of computational resources and time to generate [18,19,26–28], and are difficult to use, e.g., for iterative design optimization and parametric studies [26]. For example, the full FEA model of linear ball bearing was too computationally expensive, thus only a slice of it under external force is modeled to study its load distribution and stiffness [28]. Only a fraction (i.e., 3/100 to 1/10 sector) of slewing bearings (i.e., ball bearings with large diameter) was modeled in ANSYS to reduce the computational load when studying their load distribution [19]. To address the computational problem, the mesh-intensive ball-to-groove contact was modeled by super-element [25] or nonlinear traction spring [18,26] in "hybrid FEA models". The special treatment of ball-to-groove contact using super-element decreased number of elements and was shown to reduce computational time significantly [18,26]. But it comes with more pre-processing in the setup process (e.g., predefining elements in FEA software) and is not very flexible to changes in geometry [18,26], e.g., manufacturing errors.

An alternative or complement to using full or hybrid FE models is to employ low order FE models, often consisting of one-dimensional (1D) FEs (e.g., bar and beam elements) with much fewer DOFs than full 3D FE models. Low order FE models have the advantages of lower

complexity, faster computational time and more flexibility compared to full or hybrid FE models. As a result, low order models have been developed and employed in studying various aspects of ball bearing and ball screw behavior, including load distribution.

Low order load distribution models for rotary ball bearings are popular in the literature [24,29–36]. The first comprehensive modeling work of load distribution dates back to the 1960s [24,29], where Jones modeled the load distribution of ball bearings for the purpose of calculating bearing fatigue life. The most critical part of the model was to capture ball-to-groove contact. Jones proposed a geometry-based model where the contact load is determined by the relative distance of the groove curvature centers pertaining to each contacting groove. Static equilibrium of contact forces (and friction [29]) are established to solve for the contact status and load distribution iteratively. The model was able to incorporate changing contact angles under load. Most of the subsequent low order models for ball bearings followed Jones' geometry-based model in establishing the ball-to-groove contact for load distribution and stiffness [30–37]. A lot of low order load distribution models have been proposed for ball screws as well. The most rudimentary low order models assume uniform load distribution for all balls in ball screw and/or ignore interactions between Hertzian contact forces and elastic deformations of the screw/nut by prespecifying the elastic deformations of the screw/nut (e.g., see Refs. [38–40]). However, it is well understood that elastic deformations of the screw interact closely with Hertzian contact forces and thus affect static load distribution. Therefore, more advanced low order models consider interactions between Hertzian contact forces and axial deformation of the screw and nut (e.g., see Refs. [8,41–45]). The implicit assumption in these models is that ball screws are predominantly subjected to axial/torsional loads, which give rise to only axial/torsional deformations. While it is true that ball screws typically bear axial/torsional loads, Slocum [46] and Okwudire and Altintas [47–49] have shown that purely axial/torsional loads give rise to appreciable lateral (bending) deformation in ball screws due to the helical raceway. These induced lateral deformations could significantly influence static load distribution leading to inaccurate predictions by such models. Moreover, there are some applications (e.g., EPAS in automobiles [11,50]) where ball screws are subjected to significant lateral loads. Axial/torsional-deformation-only models are incapable of accurately characterizing static load distribution in such applications.

Another very important factor in accurately predicting load distribution of ball bearing and ball screws is the effect of geometric/manufacturing errors. Geometric errors together with eccentricity in external load cause non-uniform load distribution among balls, resulting in higher load on certain balls and reducing the fatigue life of rolling races [19]. The study of geometric errors are necessary for manufacturing tolerance specification, as too stringent requirements demand sophisticated facilities and hence the manufacturing cost is high, whereas liberal tolerances mean compromise of the performance and life of the rolling ball machine elements [19]. Geometric errors are considered in some low order distribution models for ball bearings. Potočnik, et al. [27] described irregular bearing geometry at raceway centers and studied its effect on load distribution based on a contact model similar to Jones'. In their work, only geometric errors at raceways centers were considered, whereas the geometric errors at the raceways were not incorporated. Aithal, et al. [19] presented various types of geometric errors including surface waviness, and modeled their effects on load distribution in ANSYS FEA. However, all the geometric errors were simplified as offset in the contact surfaces (i.e., equivalent error on ball radius/diameter) in ANSYS. Majda [51] mapped the straightness error of the linear bearing rail as oversize/undersize in the diameter of balls in studying its effect on the accuracy of machine tools. Geometric errors are ignored in most of the existing low order models for ball screws, e.g., see Refs. [8,41–45]. Mei et al. [43] developed a low order model for predicting static load distribution that addresses this issue by assuming that the elongation of the screw/nut, under axial loads, should compensate for the Hertzian contact deformations and geometric errors of the balls and raceways in the axial direction. Xu et al. [44] slightly improved on model of Mei et al. by incorporating effects of contact angle variation due to elastic deformations in the axial direction. However, because both these models [43,44] ignore lateral deformation, their handling of geometric errors is deficient. For instance, they treat geometric errors of groove profile and balls combined as a prespecified axial error term, which does not adequately capture the multi-directional interactions between groove profile errors, contact forces and elastic deformations.

As a result of literature review, the main deficiencies of the existing low order load distribution models for ball bearings and ball screws are identified as: (I) existing low order load distribution models for ball screw do not include lateral deformation which is significant especially under lateral load; (II) there is no comprehensive model to describe the geometric

errors and incorporate them into load distribution calculation for both ball bearing and ball screw.

1.2.2 Friction Modeling

Friction behavior is very important to the functionality of rolling ball machine elements, e.g., accuracy, motion smoothness and service life [1,52], hence it has been studied extensively in the literature.

There are many experimental studies on the friction behavior of ball bearings and ball screws. While experiments are very useful in characterizing the friction behavior in specific operating conditions, they often do not have the breadth of scope and depth of insight provided by physics-based models; they can also be expensive and time consuming to carry out, often requiring specialized jigs [52]. Modeling the friction behavior of ball bearings and ball screws thus plays an important role by reducing the testing cost and time, and yielding more generalizable understandings [1]. There are many contributing factors to friction: ball-to-groove contact, ball-to-ball contact, lubrication, cages, etc. This work is mainly focused on contact-induced friction.

The pioneering work of ball bearing modeling was done by Jones in 1959 [29]. In his model, the relative velocity field between each ball-groove contact is first derived; frictional force and moment are then obtained by integrating infinitesimal frictional stress over the contact area; by establishing the quasi-static equilibrium of frictional force and moment, ball motion and friction are solved iteratively. Building on Jones' work, several physics-based friction models for ball bearings have been proposed [52–56]. Harris and Kotzalas [54] gave a comprehensive summary of various aspect of friction modeling of ball bearings. Recently, Leblanc and Nelias [55] extended Jones' model from two-point contact to three- and four-point contact ball bearings. Joshi [56] simplified the friction model developed by Leblanc and Nelias [55] for high-load low-speed ball bearings with both two-point contact and four-point contact, and validated the simplified model against a specially designed friction torque rig. Halpin and Tran [52] used minimum energy criteria to solve the friction dynamics of four-point contact ball bearings. For ball screws, a different kinematic pattern from ball bearings was found due to helical ball track [57]. Correspondingly, friction models for ball screws were proposed following the similar process predescribed for ball bearings [40,45,58]. The beauty of the described models is that they are low order (from a numerical standpoint) compared to the alternative which is to utilize high-

order finite element analysis (FEA) models that incur much larger computational costs [59]. Moreover, low order models can sometimes be further simplified to yield elegant analytical formulations that provide explicit relationships between friction behavior and system parameters [60,61].

It is well known that generally four-point contact ball bearing has higher friction than two-point contact ones [52,59]. There is a general understanding that four-point contact ball bearing mainly has spin and sliding motion in the contact area and two-point contact ones mainly has rolling [52,59], while spin and sliding have higher friction than rolling due to larger relative velocity at the contact area as illustrated in Figure 1.4. However, there is no dedicated study of friction due to rolling, sliding and spin motions in the literature, which is important for the four-point contact ball bearing used in rack EPAS as the balls experience transition between these motions under different loading conditions.

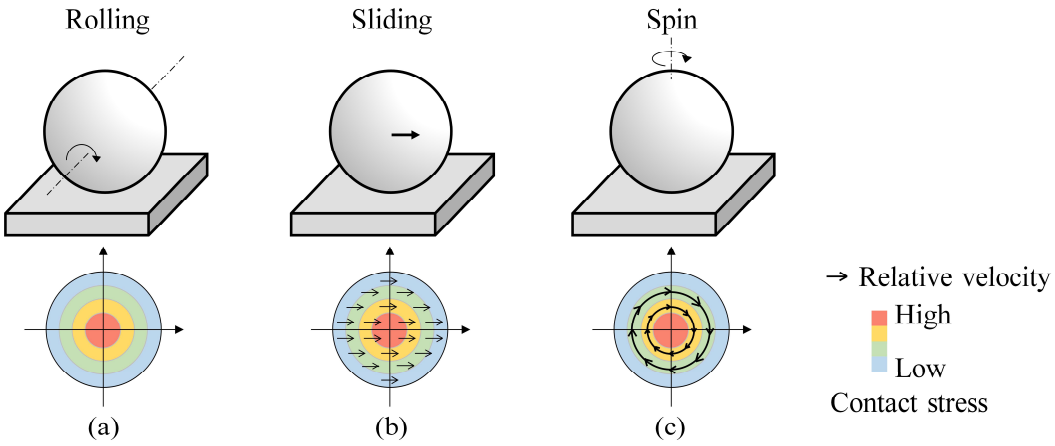

Figure 1.4: Illustration of (a) rolling; (b) sliding and (c) spin and their typical relative velocity field in the contact area

Another problem of the existing models is they focus on modeling ball-to-groove contact friction behavior without considering another important source of friction, i.e., ball-to-ball contact friction. Shimoda and Izawa [62] found, via experiments, that friction torque in oscillatory ball screws can be more than twice larger than usual, due to ball-to-ball contact. Ohta, et al, by observing loaded balls in the ball track of a linear guideway type ball bearing with a camera, proved that significant frictional force occurs due to ball-to-ball contact [63]. When ball-to-ball contact happens, the velocities of the two balls at the ball-to-ball contact interface are usually of the opposite direction (i.e., sliding) as shown in Figure 1.5. Sliding friction is typical

10^2-10^3 times larger than that of rolling according to experimental studies [64–66], making ball-to-ball contact to have significant friction increase.

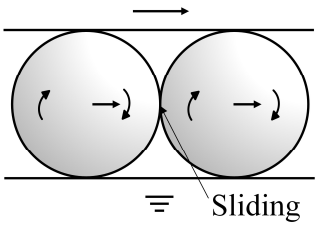

Figure 1.5: Illustration of sliding at the ball-to-ball contact interface

One way to mitigate the friction rising from ball-to-ball contact is to use spacer balls (i.e., smaller-size balls) between adjacent load-carrying balls [62,63]. The spacer balls translate sliding friction between balls into rolling friction thus mitigating ball-to-ball contact friction. However, the adoption of spacer balls has an obvious drawback, i.e., with the same number of balls, load capacity is reduced by half [67]. Therefore, to maintain the same load capacity, the number of balls needs to be doubled – which increases the size and cost of the machine elements. Another way to mitigate ball-to-ball contact is to use cages (or retainers) [68]. While caged balls are commonly adopted in rotary ball bearings, they are not commonly used with linear ball bearings and ball screws mainly because of the complexity related to recirculation and the potential reliability issues they pose [68]. Ohta, et al, continuing their work in [63], showed by using a more deformable (i.e., thinner) carriage, sticking due to ball-to-ball contact is less likely to occur [67]. Given the significance of ball-to-ball contact friction in machine elements like linear ball bearings and ball screws, there is a need for low order numerical or analytical models that consider ball-to-ball contact friction; however, no such works have been found in the literature.

As a result of literature review, it is found out that (I) there is no dedicated study of friction due to rolling, sliding and spin motions in four-point contact ball bearings; (II) ball-to-ball contact gives rise to significant friction increase and friction variation in linear ball bearings and ball screws where cages are not desirable, but there is no model which illustrates the contributing factor and the effect of ball-to-ball contact in the literature.

1.3 Dissertation Contributions and Outline

To address the deficiencies identified in the literature on low order load distribution and friction modeling of ball bearings and ball screws, the following contributions are made in this dissertation:

1) A low order load distribution model for ball screws is proposed which considers the effects of, and the interactions between: (i) Hertzian contact deformations; (ii) axial, torsional and lateral deformations, and (iii) geometric errors of the balls, screw and nut in ball screws. A new and comprehensive way of describing the screw and nut groove surfaces with geometric errors using multivariate functions is proposed. A ball-to-groove contact model based on Hertzian Contact Theory which includes geometric errors is developed.
2) A dedicated study of rolling, sliding and spin motions in four-point contact ball bearing is conducted to illustrate their effect on ball-to-groove contact friction.
3) Low order numerical models for ball-to-ball contact friction in linear ball bearings and ball screws are proposed and validated favorably against FEA models. An analytical model for ball-to-ball contact friction in four-point contact linear ball bearings is proposed, based on friction analysis and simplifying approximations. The use of insights gained from the analytical model for mitigation of ball-to-ball contact is demonstrated.
4) The developed load distribution and ball-to-ball contact friction models are applied to several case studies relevant to rack EPAS. Important insights for inspection, optimal design and manufacturing tolerance specification of ball bearings and ball screws in rack EPAS are derived.

The proposed low order load distribution model for ball screws have been published in [69,70]. The proposed ball-to-ball contact friction models have been published in [71–73]. The applications of the developed load distribution and friction models to rack EPAS gear are presented in [74].

The thesis is organized in the following order: the proposed low order load distribution model for ball screws with ANSYS FEA validation is presented in Chapter 2. In Chapter 3, sensitivity analysis of ball-to-groove friction to rolling, sliding and spin motions in four-point contact rotary ball bearings is first presented. Analytical and low order ball-to-ball contact friction models for linear ball bearings and ball screws with ANSYS FEA validation are then introduced. Chapter 4 presents the applications of the developed load distribution model and

friction model to rack EPAS gear. Conclusions and future work are discussed in Chapter 5. Necessary supplementary material is given in the Appendices.

Chapter 2 Static Load Distribution Modeling of Ball Screws

2.1 Overview

The handling of lateral deformation and geometric errors of ball screw is identified as the main deficiencies of the existing static load distribution models in the literature and is shown to be critical for the application of ball screw in rack EPAS in Chapter 1. This chapter focuses on proposing a low order static load distribution model for ball screw considering the effect of lateral deformation and geometric errors. The model is developed by first describing the groove and ball surfaces mathematically as multivariate functions to allow versatility in describing geometric errors. A contact model based on Hertzian Contact Theory is then introduced to describe the ball-to-groove contact interactions including geometric error effects. The elastic deformation of the ball screw is incorporated into the contact model by low order Finite Element Method (FEM). The resulting linear and nonlinear equations, which take into account Hertzian contact deformations, elastic deformations and geometric errors of the balls, screw and nut, are solved using the Newton-Raphson method to determine the load borne by each ball under static equilibrium. The developed low order load distribution model is benchmarked against high-order Finite Element (FE) model developed in ANSYS in simulation-based case studies, and is shown to be accurate and computationally much more efficient.

Before presenting the developed model, a few assumptions need to be clarified:

(1) There are many configurations of ball screws; however, without loss of generality, a single-start, right-handed, Gothic-arch-groove-type ball screw with a single ball nut is considered in this work. The typical ball screw consisting of a screw, a nut and balls in a helical groove is shown in Figure 2.1.

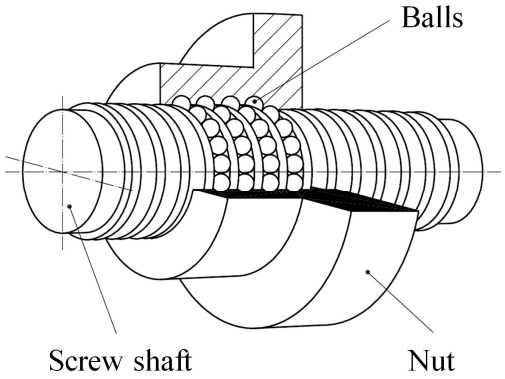

Figure 2.1: Components of a typical ball screw [75]

(2) Contact loads carried by balls in the helical groove of ball screws are the main focus of this work. Hence extraneous features, such as ball recirculation system, end seals, etc., which do not affect the loaded balls are ignored.

(3) The material properties of the screw, nut and balls are assumed to be homogeneous, isotropic and in conformance with Hooke's law (i.e., no plastic deformation) [75].

(4) Since friction coefficients of ball screws are usually small (<5%) [4], frictional forces are neglected because they do not affect contact load distribution significantly. Effects of ball-to-ball contact forces are also neglected by assuming that each ball maintains a gap relative to adjacent balls. Friction and ball-to-ball contact will be discussed in the next chapter.

This chapter is organized as follows: the contact model including geometric error effects is presented in Section 2.2. The incorporation of elastic deformation using low order FEM is shown in Section 2.3. Section 2.4 presented simulation-based case studies and FEA validation against ANSYS, followed by a summary of the chapter in Section 2.5.

2.2 Contact Model Including Geometric Error Effects

To model the contact interactions of balls with screw and nut in a ball screw, the geometry of the balls and groove surfaces needs to be accurately described. The geometric errors were predefined to the raceways' centers in some ball bearings studies [19,27]; while in the ball screw literature, geometric errors were only modeled by pre-specifying them as equivalent errors in ball diameters [43,44]. These approaches do not adequately capture the multi-directional interaction between groove profile errors, contact forces and elastic deformations. In this chapter, groove surfaces are described as multivariate functions to incorporate geometric errors.

2.2.1 Description of Groove and Ball Surfaces Including Geometric Errors

To describe the groove surfaces, a starting point is to define the nominal ball center pathway of the screw, as shown by the helix in Figure 2.2 (a). It represents the path traced by the center of a ball as it travels along the groove of a ball screw in the absence of geometric errors in the ball or groove. Defining a global coordinate system (CS=$\{x, y, z\}$), fixed to the screw as shown in Figure 2.1 (a), the locus of points lying on the ball center pathway, relative to the origin of CS, is given by

$$\bar{\mathbf{q}}_{\mathrm{B}}(\varphi) = \begin{Bmatrix} \bar{R}_{\mathrm{p}} \cos\varphi \\ \bar{R}_{\mathrm{p}} \sin\varphi \\ \bar{r}_{\mathrm{g}}\varphi \end{Bmatrix} \tag{2.1}$$

where φ is the angular distance traversed along the nominal ball center pathway starting from the x-axis to the location of interest on the screw (for the sake of simplicity, φ is referred to as azimuth angle in this work), $\bar{R}_{\mathrm{p}}$ is the nominal pitch circle radius and $\bar{r}_{\mathrm{g}}$ is the nominal gear ratio of the ball screw, given by

$$\bar{r}_{\mathrm{g}} = \frac{\bar{p}}{2\pi} \tag{2.2}$$

with $\bar{p}$ representing the nominal pitch of the ball screw.

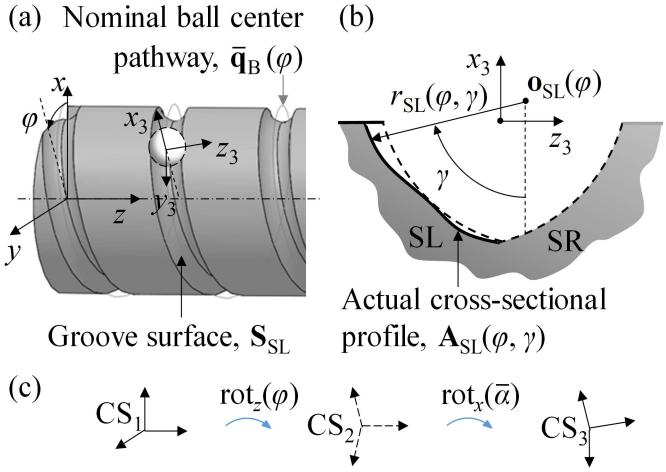

Figure 2.2: (a) Nominal ball center pathway (helix) and coordinate systems of screw; (b) cross-sectional profile of screw's groove in x_3-z_3 plane, highlighting screw left (SL) portion; (c) transformation between the three coordinate systems attached to screw

A moving coordinate system $\mathrm{CS}_3=\{x_3, y_3, z_3\}$, with its origin on the nominal ball center pathway, is established such that its y_3-axis is tangent to the helical path and its x_3-axis points

along the radial line from screw axis to nominal ball center (as shown in Figure 2.2 (a)). Figure 2.2 (b) shows the cross-sectional profile of screw's groove in the x_3-z_3 plane. Ideally, the groove profile should be a Gothic arch formed by the intersection of two circular arcs – one to the left and the other to the right of the origin of CS_3, as shown with the dashed lines. Focusing on the SL (screw left) portion of the groove, due to geometric errors, the actual cross-sectional profile of the groove (shown by the solid curve) will deviate from the nominal one in Figure 2.2 (b). The actual cross section of the groove's SL portion can be described in x_3-z_3 plane of CS_3 as a function, $\mathbf{A}_{SL}(\varphi, \gamma)$, of φ and a new cross-sectional angular variable γ (see Figure 2.2 (b)), given by

$$\mathbf{A}_{SL}(\varphi,\gamma) = \begin{Bmatrix} -r_{SL}(\varphi,\gamma)\cos\gamma \\ -r_{SL}(\varphi,\gamma)\sin\gamma \end{Bmatrix} + \left(\mathbf{o}_{SL}(\varphi)\right)_{2\times 1} \tag{2.3}$$

Here $\mathbf{o}_{SL}(\varphi)$ is the center point of the SL groove cross section (i.e., Gothic arch) measured from the origin of x_3-z_3 plane, while $r_{SL}(\varphi,\gamma)$ is the instantaneous groove radius of the actual SL groove cross section. Note that $\mathbf{A}_{SL}(\varphi,\gamma)$ is assumed to be a C^2 continuous function of both φ and γ, to provide flexibility in describing geometric errors within a given cross section of the groove, as well as from cross section to cross section along the ball pathway; C^2 continuity is needed to allow calculation of gradients which help determine contact angles and contact radii in the presence of geometric errors. In practice, $\mathbf{A}_{SL}(\varphi,\gamma)$ can be generated by fitting C^2 continuous functions of φ and γ to point cloud data obtained through experimental measurements of a screw's groove surface, as demonstrated in Ref. [76]. Note that for ball screw without geometric errors, the groove radius is constant (i.e., $r_{SL}(\varphi,\gamma) = \bar{r}_G$), and the center point $\mathbf{o}_{SL}(\varphi)$ is at a fixed position ($\bar{\mathbf{o}}_{SL}$) relative to CS_3, given by

$$\bar{\mathbf{o}}_{SL} = \begin{Bmatrix} (\bar{r}_G - \bar{r}_B)\cos\bar{\beta} \\ (\bar{r}_G - \bar{r}_B)\sin\bar{\beta} \end{Bmatrix} \tag{2.4}$$

where $\bar{r}_B$ is the nominal ball radius and $\bar{\beta}$ is the nominal contact angle between ball and groove surface.

To describe the cross-sectional profile of the groove (expressed by Eq. (2.3)) with respect to CS, a two-step transformation is carried out. Intermediate coordinate systems CS_1 and CS_2 are set up at the same origin as CS_3 (i.e., on the helix); CS_1 shares exactly the same orientation as CS; CS_2 involves a current-frame rotation of CS_1 about its z-axis by amount φ; and CS_3 involves

a current-frame rotation of CS_2 about its x-axis by amount $\bar{\alpha}$. Angle $\bar{\alpha}$ represents the nominal pitch angle of the ball screw given by

$$\bar{\alpha} = \tan^{-1}\left(\frac{\bar{p}}{2\pi \bar{R}_{\mathrm{p}}}\right) \tag{2.5}$$

Accordingly, the cross-sectional profile of the groove's SL portion is described in CS by the function

$$\mathbf{S}_{\mathrm{SL}}(\varphi,\gamma) = \mathrm{rot}_z(\varphi)\cdot \mathrm{rot}_x(\bar{\alpha})\cdot \mathbf{T}_{3-2}\cdot \mathbf{A}_{\mathrm{SL}}(\varphi,\gamma) + \bar{\mathbf{q}}_{\mathrm{B}}(\varphi) \tag{2.6}$$

where

$$\mathbf{T}_{3-2} = \begin{bmatrix} 1 & 0 \\ 0 & 0 \\ 0 & 1 \end{bmatrix} \tag{2.7}$$

helps transform the groove profile in x_3-z_3 plane to CS_3 and rot $(\cdot)$ represents a current frame rotation operation about the axis specified by its subscript, as further described in Appendix A. The same process of generating $\mathbf{S}_{\mathrm{SL}}(\varphi,\gamma)$ can be applied to the SR (screw right) surface of the groove to get $\mathbf{S}_{\mathrm{SR}}(\varphi,\gamma)$.

In the preceding discussion, geometric errors of the screw's groove have been described by incorporating them into groove surface functions $\mathbf{S}_{\mathrm{SL}}(\varphi,\gamma)$ and $\mathbf{S}_{\mathrm{SR}}(\varphi,\gamma)$. However, in practice, geometric errors are sometimes represented by the actual ball center pathway (i.e., the path traced by the center of a ball of nominal diameter as it travels along the groove of a ball screw having geometric errors) [27]. The locus of points lying on the actual ball center pathway is given by the function

$$\mathbf{q}_{\mathrm{B}}(\varphi) = \begin{Bmatrix} R_{\mathrm{p}}(\varphi)\cos\varphi \\ R_{\mathrm{p}}(\varphi)\sin\varphi \\ r_{\mathrm{g}}(\varphi)\varphi \end{Bmatrix} \tag{2.8}$$

where R_{p} and r_{g} are the actual pitch circle radius and gear ratio of the screw (which may be different from those of the nut and may vary as functions of φ). Notice that Eq. (2.8) converges to Eq. (2.1) in the absence of geometric errors. The expression for $\mathbf{q}_{\mathrm{B}}(\varphi)$ given in Eq. (2.8) can be deduced from $\mathbf{S}_{\mathrm{SL}}(\varphi,\gamma)$ and $\mathbf{S}_{\mathrm{SR}}(\varphi,\gamma)$ by using basic geometry to determine the locus of the center point of a ball of nominal diameter in contact with $\mathbf{S}_{\mathrm{SL}}(\varphi,\gamma)$ and $\mathbf{S}_{\mathrm{SR}}(\varphi,\gamma)$. Note that the

two ways of groove surface description are in essence equivalent. The approach presented here is chosen to keep accordance with practice [76].

Similar to CS applied to the screw, a body-fixed coordinate system, $CS_N=\{x_N, y_N, z_N\}$ is established for the nut as shown in Figure 2.3. The same procedure used for describing $\mathbf{A}_{SL}(\varphi,\gamma)$ for the screw in Eq. (2.3) is then used to describe the NL (nut left) groove profile as $\mathbf{A}_{NL}(\varphi_N,\gamma)$, in the nut's equivalent of CS_3. Note that φ_N is the angular distance traversed along the nominal ball pathway starting from x_N-axis to the location of interest on the nut.

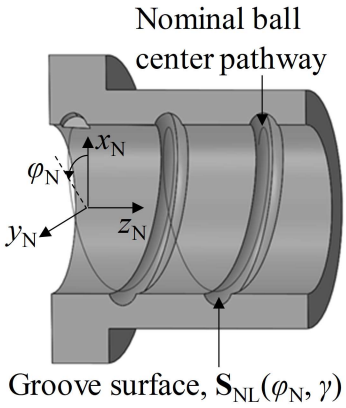

Figure 2.3: Groove profile of the nut

Assuming there is no misalignment between screw and nut and let ψ_N be used to represent the orientation of CS_N relative to CS, such that, at any given point on the nominal ball center pathway, $\varphi=\varphi_N+\psi_N$. Accordingly, the NL groove surface can be described with respect to CS as

$$\mathbf{S}_{NL}(\varphi_N,\gamma)=\mathrm{rot}_z(\varphi_N+\psi_N)\cdot\mathrm{rot}_x(\bar{\alpha})\cdot\mathbf{T}_{3-2}\cdot\mathbf{A}_{NL}(\varphi_N,\gamma)+\bar{\mathbf{q}}_B(\varphi_N+\psi_N) \tag{2.9}$$

The same process can be applied to the NR (nut right) groove surface to get $\mathbf{S}_{NR}(\varphi, \gamma)$.

Let N_B represent the number of balls within the screw/nut grooves and let the position of the i^{th} ball (i = 1, 2, …, N_B) relative to CS be defined by φ_{Bi}, which is the azimuth angle of the i^{th} ball. Each ball i is assumed to have a perfectly spherical surface; but its radius, r_{Bi}, may differ from the nominal ball radius, $\bar{r}_B$, due to geometric errors.

2.2.2 Ball-to-groove Contact Conditions

Using the mathematical description of the contacting surfaces of screw, nut and balls presented in the preceding section, the focus of this section is on describing Hertzian contact conditions for a single ball with grooves, excluding the effects of bulk elastic deformations of

screw and nut. The derived contact model is then used in Section 2.3 to model contact forces for all balls under static equilibrium, including the geometric error effects and bulk elastic deformations of screw and nut.

Within a Gothic-arch-groove-type ball screw, each ball i is typically assumed to contact the SL, SR, NL and NR surfaces of the nut's and screw's grooves at a maximum of one point per surface, resulting in at most four-point contact [4], as shown in Figure 2.4. This assumption is valid if the mathematical description of the surfaces does not include very small features (i.e., features with radius of curvature smaller than the smallest ball radius). Note that this assumption can be relaxed by adopting contact theory for wavy surfaces [77]. For each ball i, ball-to-groove contact is assumed to occur at the cross section of groove (i.e., x_3-z_3 plane of CS_3) with azimuth angle φ_{Bi}. Let us denote the x_3 and z_3 coordinates of the four contact points as $\mathbf{p}_{3SLi}$, $\mathbf{p}_{3SRi}$, $\mathbf{p}_{3NLi}$, $\mathbf{p}_{3NRi}$, respectively, and the coordinates of ball center as $\mathbf{p}_{3Bi}$, where $\mathbf{p}_{3Bi}=\{x_{3Bi},\, z_{3Bi}\}^{T}$. Considering for example the contact point $\mathbf{p}_{3SLi}$ between i^{th} ball and SL portion of groove surface, with corresponding angles γ_{SLi} in the cross section, the following conditions must be satisfied:

(I) The contact point must lie on the groove profile, i.e.,

$$\mathbf{p}_{3SLi}=\mathbf{A}_{SL}(\varphi_{Bi},\gamma_{SLi})=\mathbf{A}_{SLi} \tag{2.10}$$

(II) The contact normal must be tangent to the groove profile at the contact point, i.e.,

$$\hat{\mathbf{n}}_{SLi}\cdot\mathbf{t}_{SLi}=\mathbf{0} \tag{2.11}$$

where $\hat{\mathbf{n}}_{SLi}$ denotes the ball surface contact normal unit vector, pointing from the contact point to the ball center, i.e.,

$$\hat{\mathbf{n}}_{SLi}=\frac{\mathbf{p}_{3Bi}-\mathbf{p}_{3SLi}}{\left\|\mathbf{p}_{3Bi}-\mathbf{p}_{3SLi}\right\|}=\frac{\mathbf{p}_{3Bi}-\mathbf{A}_{SLi}}{\left\|\mathbf{p}_{3Bi}-\mathbf{A}_{SLi}\right\|} \tag{2.12}$$

while $\mathbf{t}_{SLi}$ represents the tangent vector of the groove profile at the cross section. Since the groove profile is parameterized as a multivariate function of real-valued angles, φ and γ, its tangential unit vector at the cross section can be expressed as

$$\mathbf{t}_{SLi}=\left.\frac{\partial\mathbf{A}_{SL}}{\partial\gamma}\right|_{\varphi=\varphi_{Bi},\gamma=\gamma_{SLi}}=\frac{\partial\mathbf{A}_{SLi}}{\partial\gamma_{SLi}} \tag{2.13}$$

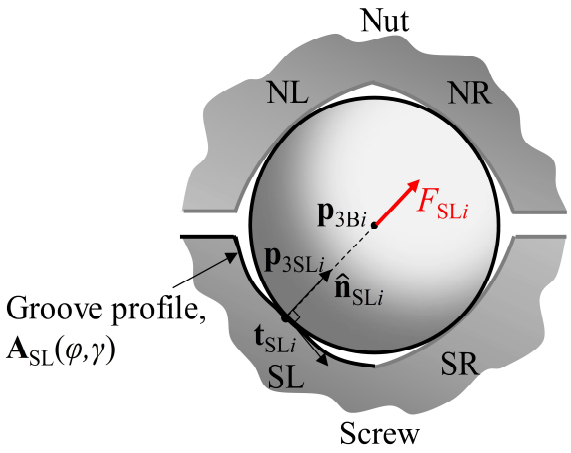

Figure 2.4: A ball in four-point contact with Gothic arch grooves of ball screw

(III) The contact force lies along the contact normal, $\hat{\mathbf{n}}_{SLi}$, and is of magnitude F_{SLi}, determined by Hertzian Contact Theory as [77]

$$F_{SLi}=\begin{cases}\left(\dfrac{1}{C_{SLi}}\delta_{SLi}\right)^{\frac{3}{2}} & \text{if} \quad \delta_{SLi}=r_{Bi}-r_{SLi}>0\\ 0 & \text{if} \quad \delta_{SLi}=r_{Bi}-r_{SLi}\le 0\end{cases} \tag{2.14}$$

where

$$r_{SLi}=\left\|\mathbf{p}_{3Bi}-\mathbf{p}_{3SLi}\right\|=\left\|\mathbf{p}_{3Bi}-\mathbf{A}_{SLi}\right\| \tag{2.15}$$

and δ_{SLi} is the Hertzian contact (elastic) deformation of the ball surface relative to the groove surface. Note that because δ_{SLi} represents localized relative deformation between ball and groove, it can be applied to either ball or groove surface. Therefore it is chosen to apply δ_{SLi} exclusively to the ball surface, thus allowing the assumption that the groove surface is intact (used in establishing Conditions (I) and (II) above). Notice also that conditions for loss of contact are incorporated into the Hertzian force-deformation relationship of Eq. (2.14). The Hertzian constant, C_{SLi}, occurring in Eq. (2.14), is given by the general expression in [77] which is detailed in Appendix B. To reduce the computational load, the Hertzian constant can be approximated based on the nominal geometry of ball screw with minimal error as shown in Appendix B. In this case, $C_{SLi}=C_{SRi}=C_S$ and $C_{NLi}=C_{NRi}=C_N$.

2.3 Incorporation of Elastic Deformations into Contact Model Using Low Order FEM

In the preceding section, only Hertzian contact elastic deformations were considered; bulk elastic deformations of the screw and nut were ignored in establishing contact conditions. However, in reality, the contact forces from each ball, when applied to the screw and nut, induce bulk elastic deformations which in turn change the shape of the groove profile thus affecting contact conditions for other balls. Again, focusing detailed discussions on the SL section of the groove surfaces, the function describing the elastically deformed cross-sectional groove surface, $\tilde{\mathbf{A}}_{\mathrm{SL}}(\varphi, \gamma)$, is given by

$$\tilde{\mathbf{A}}_{\mathrm{SL}}\left(\varphi,\gamma\right)=\mathbf{A}_{\mathrm{SL}}\left(\varphi,\gamma\right)+\mathbf{d}_{\mathrm{SL}}\left(\varphi,\gamma\right) \tag{2.16}$$

where $\mathbf{d}_{\mathrm{SL}}$ is the elastic deformation of any given point on the cross section of SL groove measured in the x_3-z_3 plane of CS_3. It is related to $\mathbf{u}_{\mathrm{SL}}$, the elastic deformations of any given point on the SL groove surface measured in CS as

$$\mathbf{d}_{\mathrm{SL}}(\varphi,\gamma)=\mathbf{T}_{3-2}^{\mathrm{T}}\cdot\left(\mathrm{rot}_{z}(\varphi)\cdot\mathrm{rot}_{x}(\bar{\alpha})\right)^{-1}\cdot\mathbf{u}_{\mathrm{SL}}(\varphi,\gamma) \tag{2.17}$$

While elastic deformations of the screw/nut can be determined by using elaborate 3-D finite element analysis (FEA), it is often preferable to calculate them using low order FEMs [8,41,42,44,47–49,78]. In low order FEMs, the nut is typically treated as a rigid body while the screw is modeled using 1-D FEs like bar or beam elements [47–49,79]. This is because the bulk elastic deformations of the nut are typically negligible compared to those of the screw [47–49,79]. Modeling a screw using 1-D FEs is a very straightforward process which can be found in standard FEM textbooks and several references, e.g., [8,41,42,44,47–49,78,80].

2.3.1 Modeling Elastic Deformation with Low Order FEM

For the purposes of low order FE modeling, the elastic deformation of the screw at the contact point must be transformed to FE nodes of the screw shaft. This involves a coordinate transformation process, much of which has been detailed in prior work [47–49,69]. To avoid unnecessary repetition, the transformation process is briefly summarized.

As discussed previously, the screw is modeled as Timoshenko beam FEs capable of axial, torsional and lateral elastic deformations. Let us for the sake of simplicity focus on the section of the screw within the nut, as shown in Figure 2.5. Without loss of generality, assume that finite

element j is of length $L_{\mathrm{Elm}j}$, having nodes j and j+1 to its left and right, respectively. Each node j has 6 DOFs, i.e., three translational displacements $\mathbf{u}_{\mathrm{S}j}=\{u_{\mathrm{S}xj}, u_{\mathrm{S}yj}, u_{\mathrm{S}zj}\}^{\mathrm{T}}$ and three small-angle rotational displacements $\boldsymbol{\theta}_{\mathrm{S}j}=\{\theta_{\mathrm{S}xj}, \theta_{\mathrm{S}yj}, \theta_{\mathrm{S}zj}\}^{\mathrm{T}}$ – such that the generalized displacement vector of the node is given by $\mathbf{U}_{\mathrm{S}j}=\{\mathbf{u}_{\mathrm{S}j}^{\mathrm{T}}, \boldsymbol{\theta}_{\mathrm{S}j}^{\mathrm{T}}\}^{\mathrm{T}}$.

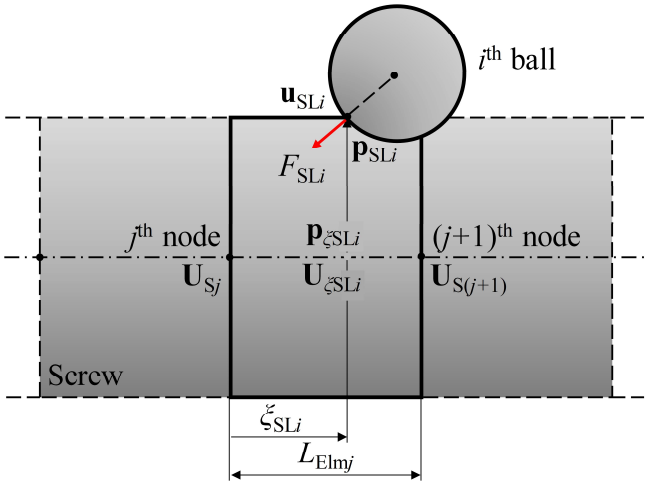

Figure 2.5: Finite element partition of screw and the nodal displacements

Assume that the i^{th} ball is in contact with the SL groove surface within element j at point $\mathbf{S}_{\mathrm{SL}i}=\mathbf{S}_{\mathrm{SL}}(\varphi_{\mathrm{B}i}, \gamma_{\mathrm{SL}i})$, as depicted in Figure 2.5. Let $\mathbf{u}_{\mathrm{SL}i}=\{u_{\mathrm{SL}xi}, u_{\mathrm{SL}yi}, u_{\mathrm{SL}zi}\}^{\mathrm{T}}$ represent the displacements of the groove surface at the contact point, due to elastic deformation. The transformation seeks to relate $\mathbf{u}_{\mathrm{SL}i}$ to the generalized nodal displacements $\mathbf{U}_{\mathrm{S}j}$ and $\mathbf{U}_{\mathrm{S}(j+1)}$. Let $\mathbf{p}_{\xi\mathrm{SL}i}$ represents the projection of $\mathbf{S}_{\mathrm{SL}i}$ onto the axis of the screw as shown in Figure 2.5, with $\xi_{\mathrm{SL}i}\in[0, 1]$ denoting the non-dimensional distance measured from node j to $\mathbf{p}_{\xi\mathrm{SL}i}$. If the generalized displacement vector of point $\mathbf{p}_{\xi\mathrm{SL}i}$ is given by $\mathbf{U}_{\xi\mathrm{SL}i}=\{\mathbf{u}_{\xi\mathrm{SL}i}^{\mathrm{T}}, \boldsymbol{\theta}_{\xi\mathrm{SL}i}^{\mathrm{T}}\}^{\mathrm{T}}$, one can relate $\mathbf{u}_{\mathrm{SL}i}$ and $\mathbf{U}_{\xi\mathrm{SL}i}$ through a transformation matrix, $\mathbf{T}_{\xi}$, by assuming that each cross section of the screw is rigid [48]; i.e.,

$$\mathbf{u}_{\mathrm{SL}i}=\underbrace{\begin{bmatrix}\mathbf{I}_{3\times3} & -\mathbf{D}(\mathbf{r}_{\xi\mathrm{SL}i})\end{bmatrix}}_{\mathbf{T}_{\xi}(\mathbf{r}_{\xi\mathrm{SL}i})}\begin{Bmatrix}\mathbf{u}_{\xi\mathrm{SL}i}\\ \boldsymbol{\theta}_{\xi\mathrm{SL}i}\end{Bmatrix}=\mathbf{T}_{\xi}(\mathbf{r}_{\xi\mathrm{SL}i})\mathbf{U}_{\xi\mathrm{SL}i} \tag{2.18}$$

where $\mathbf{r}_{\xi\mathrm{SL}i}=\mathbf{S}_{\mathrm{SL}i}-\mathbf{p}_{\xi\mathrm{SL}i}$ is the radial component of $\mathbf{S}_{\mathrm{SLi}}$, $\mathbf{I}$ is the identity matrix and $\mathbf{D}(\mathbf{r})$ is the tensorial representation of a vector $\mathbf{r}=\{r_x, r_y, r_z\}^{\mathrm{T}}$ such that

$$\mathbf{D}(\mathbf{r}) = \begin{bmatrix} 0 & -r_z & r_y \\ r_z & 0 & -r_x \\ -r_y & r_x & 0 \end{bmatrix} \tag{2.19}$$

Moreover, $\mathbf{U}_{\xi \mathrm{SL}i}$ is related to the generalized displacements of the adjacent nodes ($\mathbf{U}_{\mathrm{S}j}$ and $\mathbf{U}_{\mathrm{S}(j+1)}$) as

$$\begin{Bmatrix} \mathbf{U}_{\mathrm{S}j} \\ \mathbf{U}_{\mathrm{S}(j+1)} \end{Bmatrix} = \mathbf{T}_{\mathrm{S}-\xi}\left(\xi_{\mathrm{SL}i}\right)\mathbf{U}_{\xi \mathrm{SL}i} \tag{2.20}$$

where $\mathbf{T}_{\mathrm{S}\text{-}\xi}$ is the shape function matrix of the beam FE [48] detailed in Appendix C. Combining Eqs. (2.18) and (2.20), the overall transformation matrix $\mathbf{T}_{\mathrm{S}}$ between $\mathbf{u}_{\mathrm{SL}i}$ and the generalized nodal displacements of the j^{th} element of the screw is

$$\mathbf{u}_{\mathrm{SL}i} = \underbrace{\mathbf{T}_{\xi}\left(\mathbf{r}_{\xi \mathrm{SL}i}\right)\mathbf{T}_{\mathrm{S}-\xi}^{\mathrm{T}}\left(\xi_{\mathrm{SL}i}\right)}_{\mathbf{T}_{\mathrm{S}}\left(\mathbf{r}_{\xi \mathrm{SL}i},\,\xi_{\mathrm{SL}i}\right)} \begin{Bmatrix} \mathbf{U}_{\mathrm{S}j} \\ \mathbf{U}_{\mathrm{S}(j+1)} \end{Bmatrix} \tag{2.21}$$

Accordingly, the contact force $F_{\mathrm{SL}i}$ acting on the groove, opposite to the contact normal direction, can be transformed to equivalent forces acting on the nodes as

$$\begin{Bmatrix} \mathbf{F}_{\mathrm{SL}j} \\ \mathbf{F}_{\mathrm{SL}(j+1)} \end{Bmatrix} = \mathbf{T}_{\mathrm{S}}^{\mathrm{T}}\left(\mathbf{r}_{\xi \mathrm{SL}i}, \xi_{\mathrm{SL}i}\right) \cdot \mathbf{T}_{3-2} \cdot \left(-\hat{\mathbf{n}}_{\mathrm{SL}i} F_{\mathrm{SL}i}\right) \tag{2.22}$$

The similar transformation process can be conducted to SR contact surface to get the equivalent forces of $F_{\mathrm{SR}i}$ acting on the nodes. Together with the external forces/moments applied to the screw, the generalized force vector acting on the nodes of the screw can be formed as $\mathbf{F}_{\mathrm{S}}$. If the screw is partitioned to finite elements with N_{S} nodes, then $\mathbf{F}_{\mathrm{S}}$ is a vector of size $(6\times N_{\mathrm{S}})\times 1$, the same as $\mathbf{U}_{\mathrm{S}}$.

The nodal displacements of the screw $\mathbf{U}_{\mathrm{S}}$, under contact forces and external force, is of interest, as it is related to the groove surface displacement in Eq. (2.21). The nodal displacements must satisfy the static equilibrium as

$$\mathbf{K}_{\mathrm{S}}\mathbf{U}_{\mathrm{S}} - \mathbf{F}_{\mathrm{S}} = \mathbf{0} \tag{2.23}$$

where $\mathbf{K}_{\mathrm{S}}$ represents a nominally statically constrained stiffness matrix of the screw, comprising beam FE stiffness matrices $\mathbf{K}_{\mathrm{Elm}j}$ of the screw using standard finite element procedures [47–49]. The details of $\mathbf{K}_{\mathrm{Elm}j}$ are given in Appendix D. Boundary condition can be incorporated accordingly in the finite element procedure as well.

The nut is treated as a rigid body except for the Hertzian contact deformation at the contact region in this work. Thus the bulk elastic deformation of the nut is always zero.

2.3.2 Iterative Solution Process for Contact Forces

Including effects of elastic deformation, all balls must satisfy contact conditions (I), (II) and (III) in Section 2.2.2, with the description of undeformed surface $\mathbf{A}_{\mathrm{SL}}(\varphi, \gamma)$ replaced by that of deformed surface $\widetilde{\mathbf{A}}_{\mathrm{SL}}(\varphi, \gamma)$. Besides the contact conditions, the net forces on each ball must be zero; i.e.,

$$\mathbf{F}_{\mathrm{SL}i} + \mathbf{F}_{\mathrm{SR}i} + \mathbf{F}_{\mathrm{NL}i} + \mathbf{F}_{\mathrm{NR}i} = \mathbf{0} \tag{2.24}$$

where $\mathbf{F}_{\mathrm{SL}i}=F_{\mathrm{SL}i}\cdot\hat{\mathbf{n}}_{\mathrm{SL}i}$, $\mathbf{F}_{\mathrm{SR}i}=F_{\mathrm{SR}i}\cdot\hat{\mathbf{n}}_{\mathrm{SR}i}$, etc. The screw must be in static equilibrium under contact forces and external force as shown in Eq. (2.23).

As a result, a state vector, $\mathbf{x} = \{\ldots,\mathbf{p}_{3\mathrm{B}i}^{\mathrm{T}}, \gamma_{\mathrm{SL}i},\gamma_{\mathrm{SR}i},\gamma_{\mathrm{NL}i},\gamma_{\mathrm{NR}i},\ldots,\mathbf{U}_{\mathrm{S}}^{\mathrm{T}}\}_{(6\times N_{\mathrm{B}}+6\times N_{\mathrm{S}})\times 1}^{\mathrm{T}}$ is defined together with a function $\boldsymbol{\Phi}(\mathbf{x})$ containing equations for contact conditions, static equilibrium for all balls and screw shaft are formed as

$$\boldsymbol{\Phi}(\mathbf{x}) = \left\{ \begin{array}{c} \vdots \\ \left.\begin{array}{c} \hat{\mathbf{n}}_{\mathrm{SL}i}\cdot\mathbf{t}_{\mathrm{SL}i} \\ \vdots \end{array}\right\} \\ \left.\mathbf{F}_{\mathrm{SL}i} + \mathbf{F}_{\mathrm{SR}i} + \mathbf{F}_{\mathrm{NL}i} + \mathbf{F}_{\mathrm{NR}i}\right\}_{2\times 1} \end{array} \right\} i^{\mathrm{th}}\ \text{ball} \\ \vdots \\ \mathbf{K}_{\mathrm{S}}\mathbf{U}_{\mathrm{S}} - \mathbf{F}_{\mathrm{S}} \Bigg\}_{(6\times N_{\mathrm{B}}+6\times N_{\mathrm{S}})\times 1} = \mathbf{0} \tag{2.25}$$

The state vector $\mathbf{x}$ that makes $\boldsymbol{\Phi}(\mathbf{x}) = \mathbf{0}$ can be solved for iteratively via the Newton-Raphson method according to the expression

$$\mathbf{x}^{q+1} = \mathbf{x}^{q} - \mathbf{J}_{\boldsymbol{\Phi}}(\mathbf{x}^{q})^{-1}\boldsymbol{\Phi}(\mathbf{x}^{q}) \tag{2.26}$$

where the superscript q represents the solution at the q^{th} iteration and $\mathbf{J}_{\boldsymbol{\Phi}}$ is the Jacobian matrix of $\boldsymbol{\Phi}$ with respect to $\mathbf{x}$. In actual implementation, explicit Jacobian $\mathbf{J}_{\boldsymbol{\Phi}}$ is supplied to speed up the computation. The details of explicit Jacobians are presented in Appendix E. As an alternative, *fsolve* function in MATLAB® can also be utilized to solve the problem. Once the state vector that yield static equilibrium is determined, contact forces can be calculated from Eq. (2.14). A summary of the solution process is given in Figure 2.6.

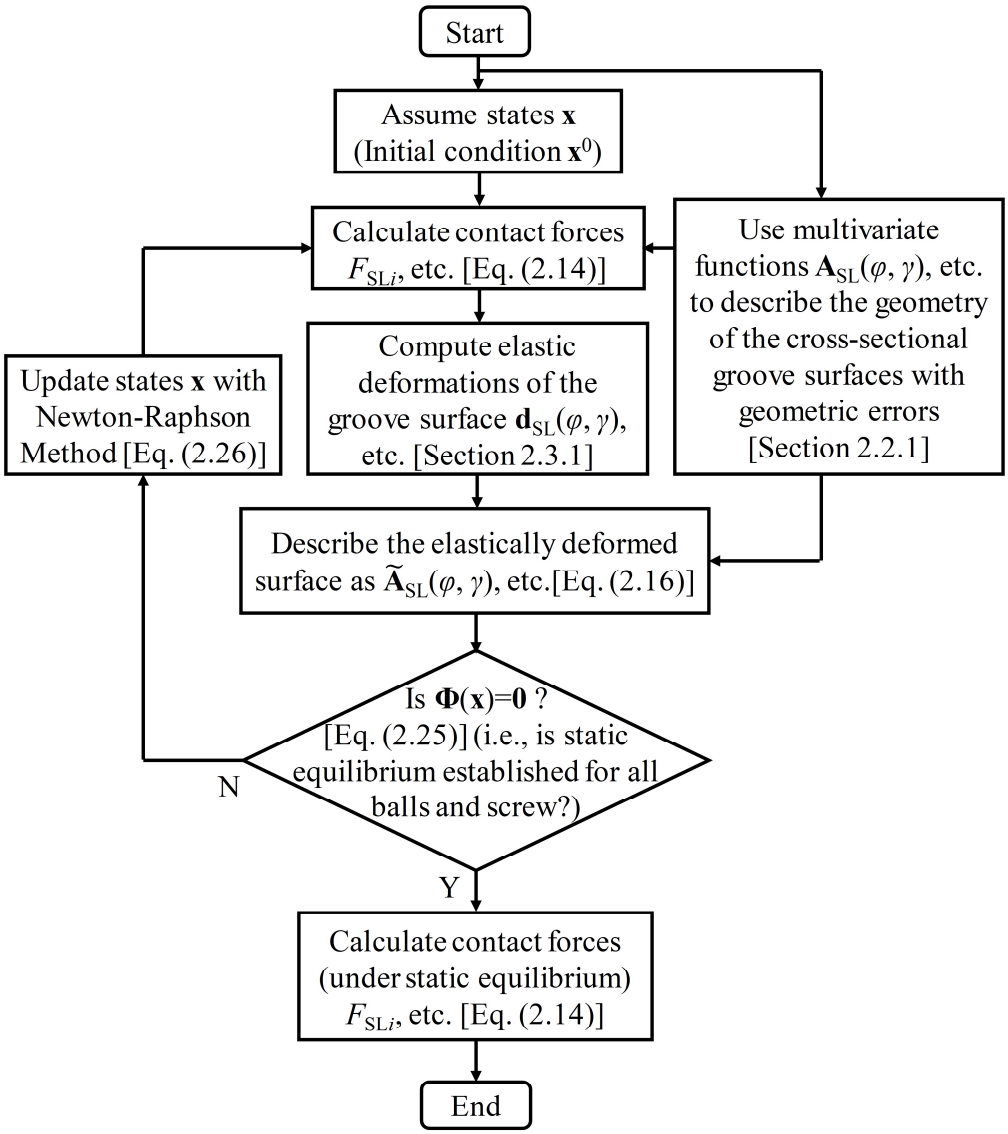

Figure 2.6: Flowchart summarizing the iterative solution process for contact loads under static equilibrium using the proposed low order model

Notice the modeling process described above updates the Journal of Mechanical Design (JMD) paper [70], on which much of this chapter is based, in the following aspects:

(1) The updated model described herein assumes that the azimuth angles of a ball's four contact points are the associated ball's azimuth angle. Thus, in the updated model, the ball center location and contact points are located in one plane, as opposed to the JMD paper where they are in different planes (i.e., in 3D). This update is mainly to keep in accordance with friction modeling in the next chapter. Moreover, the planar model also has better numerical stability and reduced computational time (due to fewer variables) than the 3D model.

(2) Condition (I) for the contact model in Section 2.2.2 is a constraint that always needs to be satisfied. Thus, in the updated model, the variable for contact point location $\mathbf{p}_{3\mathrm{SL}i}$ is replaced with $\widetilde{\mathbf{A}}_{\mathrm{SL}i}$ in establishing contact conditions instead of assuming it as a variable as in the JMD paper. This update leads to the reduction of variables hence computational time.

(3) The elastic deformation of screw, $\mathbf{U}_{\mathrm{S}}$, is solved together with other variables in Eq. (2.25) instead of separately as in the JMD paper.

(4) The indentation of the groove on the screw shaft are factored in calculating the cross sectional area and the second moment of area of screw in low order finite element method (FEM) as detailed in Appendix C.

(5) Explicit Jacobian is implemented to significantly reduce the computational time.

2.4 Simulation-based Case Studies

To validate the proposed low order load distribution model against standard high order FEA models, ANSYS® Workbench is chosen as benchmark because of its reputation in static and dynamic structural analysis.

Simulation-based case studies are presented in this section to validate the proposed low order static load distribution model against ANSYS FEA results, and demonstrate its benefits with regard to computational efficiency, ease-of-use and versatility. The simulation-based case studies are carried out using the parameters of an off-the-shelf NSK ball screw (part number BSS3220-5E) [81] with Gothic-arch groove; its key parameters are summarized in Table 2.1. In all cases studied, the nut is positioned at the middle of the screw and fixed on its left end (see Figure 2.7) to constrain its six rigid body motions, and the screw is fixed at its left end to only allow its axial (i.e., z-directional) translational displacement; the right end of the screw is either free (Case Study 1, 2) or constrained (indicated by dashed line for Case Study 3). An axial force F_{ax}=5000 N is applied to the left end of the screw. The 32 load-bearing balls of the ball screw are assumed to be uniformly distributed along the helical groove within the nut.

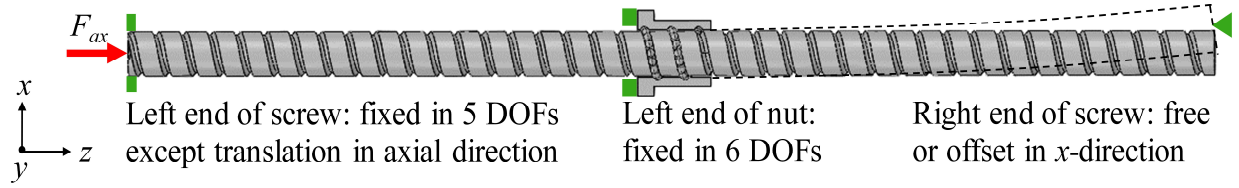

Figure 2.7: Boundary and loading conditions of ball screw used for simulation-based case studies

Table 2.1: Nominal parameters for the ball screw in simulation-based case studies

Parameter (Symbol)	Value [Unit]
Length of screw	800 [mm]
Nominal pitch circle radius ($\bar{R}_p$)	16.5 [mm]
Nominal pitch ($\bar{p}$)	20 [mm]
Nominal contact angle ($\bar{\beta}$)	45 [°]
Nominal ball radius ($\bar{r}_B$)	2.778 [mm]
Number of loaded balls (N_B)	32
Nominal radius of curvature of groove ($\bar{r}_G$)	3.254 [mm]
Outer diameter of nut	48 [mm]
Length of nut	54 [mm]
Young's modulus (E_S=E_N=E_B)	210 [N/mm^2]
Poisson's ratio (ν_S=ν_N=ν_B)	0.28

2.4.1 Comparative Case Studies against ANSYS FEA

The accuracy and computational efficiency of the proposed low order static load distribution model is compared against: (1) A low order model proposed by Mei et al. [78] which considers only axial geometric errors and deformations (using bar FEs); and (2) A high order 3-D FE model created using ANSYS Workbench 16.2. In the proposed model, the screw is modeled using Timoshenko beam FEs [47–49]. Within the nut, each beam element is of length 15 mm; outside the nut, beam elements are of length close to the pitch circle diameter. For the bar elements in Mei et al.'s model [78], the element is of length 1.25 mm within the nut, equal to the distance between the centers of any two consecutive balls; element of length close to the pitch circle diameter outside the nut is adopted. Based on the guidelines provided by ANSYS [82], the ball surface is set as contact surface while the groove surface is set as target surface. All the ball-to-groove contact interfaces are set as frictional contact with 0.01 friction coefficient to stabilize the solution. Augmented Lagrange contact formulations are used for the contact interfaces as recommended by ANSYS because of its robustness and flexibility [82]. The 3-D FE model is meshed with first-order tetrahedral elements, each having 4 nodes and 4 faces. It is common practice to make mesh refinements around the contact region while using coarser mesh elsewhere on the ball screw in order to reduce the number of elements in 3-D FE models. Here, a

mesh refinement technique in ANSYS Workbench, called Body of Influence [83], is used (see Figure 2.8 for example). The fine mesh is roughly of size 0.08 mm while the coarse mesh, applied outside contact regions of the ball screw, is roughly of size 5 mm. The other settings in the finite element model are left at their default values. Upon solution, steady-state ball-to-groove contact forces are extracted from the FEA result using Reaction Force Probe.

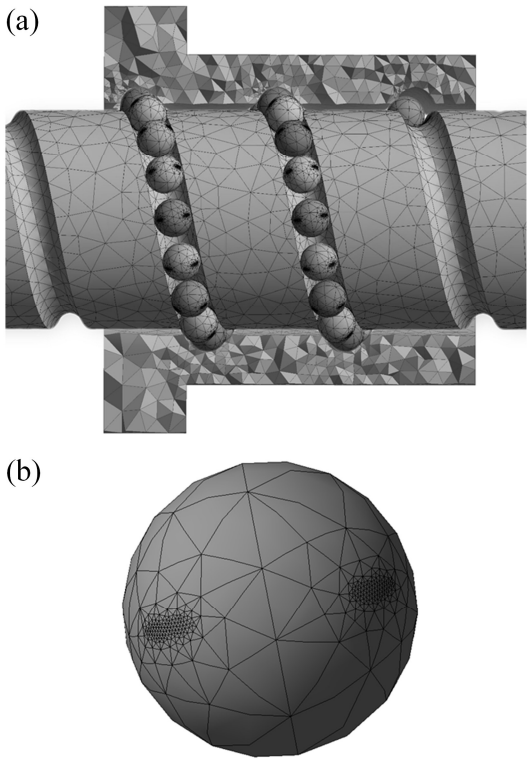

Figure 2.8: (a) 3D mesh of the ball screw and (b) mesh refinement around the contact region

2.4.1.1 Case Study 1: Nominal Case

The goal of the first case study is to exemplify the effect of lateral deformation on the accuracy of the two low order models benchmarked against the high order ANSYS model. Accordingly, the ball screw is assumed to have no geometric errors and no oversized ball preload, contact loads are determined under the influence of the 5000 N axial load. Figure 2.9 shows the load distribution predicted by the three models. Note that, because the balls are not preloaded, each ball only contacts the raceway of the screw and nut at two points instead of four; the contact forces on SR and NL sides of the groove are zero. The load distribution predicted by the 3-D ANSYS model for the SL and NR contact points is in good agreement with that predicted by the proposed model: the maximum error is 5.38% and RMS error is 2.30%. Possible reasons for the discrepancies are: (1) the low order model is able to capture the key features of

ball screw but not all the details; (2) ANSYS FEA results depend on mesh size and can be further improved, at the expense of longer computational time. Both models predict a non-uniform contact load distribution where the maximum load is about 1.34 times the minimum load. However, Mei's model, which only considers the axial deformation, predicts uniformly decreasing contact loads, which is grossly erroneous when benchmarked against the 3-D ANSYS model.

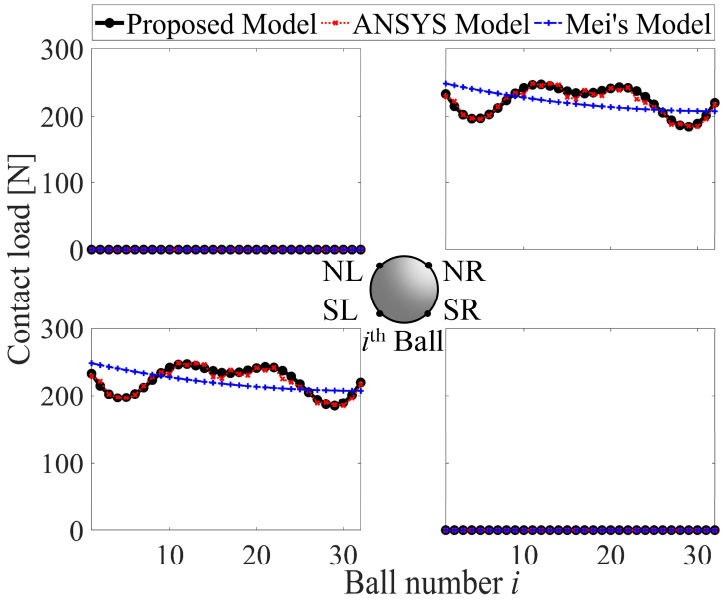

Figure 2.9: Load distribution at four contact points predicted by the three models under study

The prediction error of Mei et al.'s model can be explained by realizing that in ball screw there is coupling between axial, torsional and lateral deformations, such that the purely axial load applied to ball screw leads to non-axial deformation [46–49]. Figure 2.10 compares the screw centerline displacements in the lateral (x and y) directions as predicted by the three models under study. The proposed and ANSYS models again show good agreement in predicting the presence of lateral deformation due to the applied axial load; Mei et al.'s model cannot capture this coupling, hence its prediction of contact loads is erroneous.

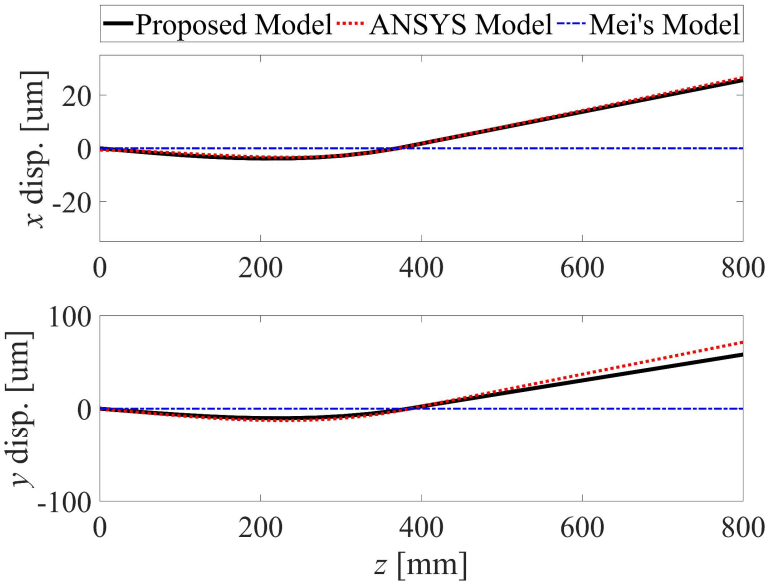

Figure 2.10: Axial-force-induced lateral deformation of ball screw shaft centerline as predicted by the three models under study

2.4.1.2 Case Study 2: Geometric Error

The goal of this case study is to evaluate the accuracy of the proposed model relative to the ANSYS model in predicting effects of geometric errors on load distribution; because of its inaccuracy in errorless case, Mei et al.'s model is not considered further. Keeping the exact same setup as in Case Study 1, in this case study, the 17th ball is assumed to have +1 μm radius error (i.e., it is oversized). The resultant load distribution is shown in Figure 2.11. Both models predict an abrupt increase in the contact load for the 17th ball, with minimal effects on the contact loads of adjacent balls. Similar to Case Study 1, the maximum and RMS prediction errors of the proposed model relative to the ANSYS model are 4.85% and 2.60%, respectively, again confirming the accuracy of the proposed model.

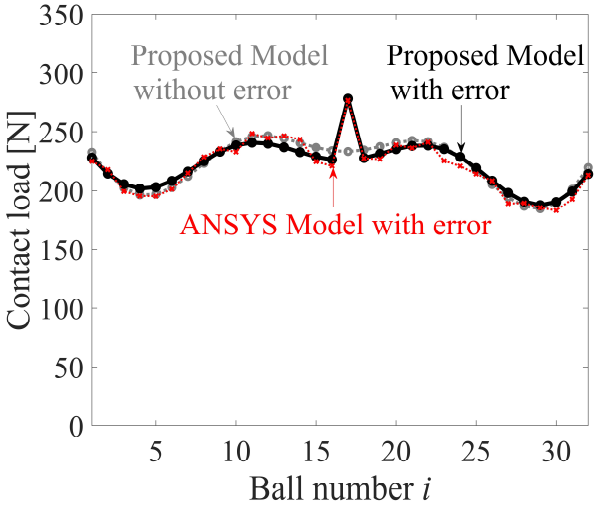

Figure 2.11: Axial-force-induced load distribution with +1 μm ball radius error in 17th ball

2.4.1.3 Case Study 3: Lateral Deformation

This case study aims to show the capability of the proposed model in handling misalignment (which introduces lateral load) and oversized ball preload. The simulation setup is similar to that of Case Study 1 and 2, except (1) all balls have 7 μm oversize in the radius to simulate preload; (2) the right end of the screw shaft is offset by 300 μm in the x-direction as shown in Figure 2.7, which simulates the mounting error in practice. In the proposed low order model, a +300 µm constraint is set to the x-displacement of the last node of the screw shaft in the finite element process.

The resultant load distribution under F_{ax} = 5000 N with and without offset is shown in Figure 2.12. There are contact loads in all four contact points because of the oversized ball preload. Compared to the no offset case, the offset in x-direction changes contact load distribution significantly. The most noticeable change is the increase of contact loads in the SR and NL contact pair for the last few balls because these balls are squeezed due to the bending of the screw shaft. The load distribution predicted by the 3-D ANSYS model is again in good agreement with that predicted by the proposed model, confirming the accuracy of the proposed model.

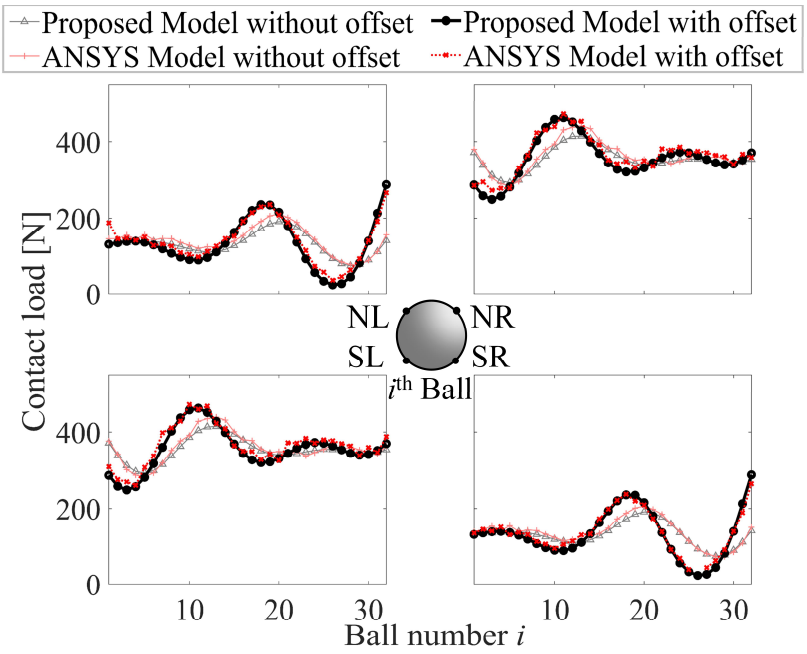

Figure 2.12: Load distribution with and without offset

2.4.1.4 Comparison of Computational Cost

Given the accuracy of the proposed model compared to the ANSYS model, it is of interest to compare the two models with regard to model size and computational cost. As shown in Table 2.2, compared to the ANSYS model which has nearly a million elements, the proposed model has only 27 elements. As a result it takes about 4 seconds to compute the desired load distribution in Case Studies 1, 2 and 3; i.e., over 6800 times faster than the ANSYS model. The proposed low order model is therefore simpler and computationally less expensive than the ANSYS model, thus is much more desirable, e.g., for use in parametric studies and optimal design of ball screws.

Table 2.2: Comparison of number of element and computational time based on the proposed models and ANSYS FEA for ball screw

Model	**No. of Elements**	**Computational Time***		
		Case Study 1	**Case Study 2**	**Case Study 3**
Proposed Model	27	3.87 seconds	3.97 seconds	3.93 seconds
ANSYS FEA Model	961,196	7.35 hours	7.61 hours	7.91 hours

* Both models are run on Intel(R) Core(TM) i7-3770 CPU @3.40GHz with 16 GB RAM.

2.4.2 Demonstration of Versatility and Ease-of-Use

Case 2, above, validated the proposed model against the ANSYS model using a simple case of radius error in a single ball. However, by describing groove surface using a multivariate function (as explained in Section 2.2.1), the proposed model is able to represent a variety of geometric errors that may occur in ball screw. Consider a situation where a ball screw has the following geometric errors:

(1) **Groove Profile Errors:** Due to uneven tool wear during manufacturing of the ball screw, the nominal radius, $\bar{r}_G$, of the SL groove surface is offset inward by amount $\Delta r_{SL}(\gamma) = 3 - \gamma$ μm, $\gamma \in [0.033\pi, 0.417\pi]$ (see Figure 2.13 (a)); similarly, the SR, NL and NR surfaces are offset by $\Delta r_{SR}(\gamma) = 3 - \gamma/2$ μm, $\Delta r_{NL}(\gamma) = 2 - \gamma$ μm and $\Delta r_{NR}(\gamma) = 2 - \gamma/4$ μm, respectively.

(2) **Pitch Errors:** Due to tool positioning precision issues during manufacturing of the ball screw, there is an error in the nominal groove center position for the SL groove surface given by $\mathbf{e}_{SL}(\varphi) = [0 \ 3\sin\varphi]^T$ μm (see Figure 2.13 (b)); similarly the SR, NL and NR surfaces tool center positions have errors $\mathbf{e}_{SR}(\varphi) = \mathbf{e}_{SL}(\varphi)$; $\mathbf{e}_{NL}(\varphi) = [0 \ -2\sin(\varphi/2)]^T$ μm and $\mathbf{e}_{NR}(\varphi) = \mathbf{e}_{NL}(\varphi)$, respectively.

(3) **Ball Radius Errors:** Balls have radial errors with normal (Gaussian) distribution $N(0, \sigma^2)$, where standard deviation $\sigma = 1$ μm.

Note that geometric error categories (1) and (2) above can be applied to the proposed model simply by modifying Eq. (2.3) to

$$\mathbf{A}_{SL}(\varphi,\gamma) = \begin{Bmatrix} -\left(\bar{r}_G - \Delta r_{SL}(\gamma)\right)\cos\gamma \\ -\left(\bar{r}_G - \Delta r_{SL}(\gamma)\right)\sin\gamma \end{Bmatrix} + \bar{\mathbf{o}}_{SL} + \mathbf{e}_{SL}(\varphi) \tag{2.27}$$

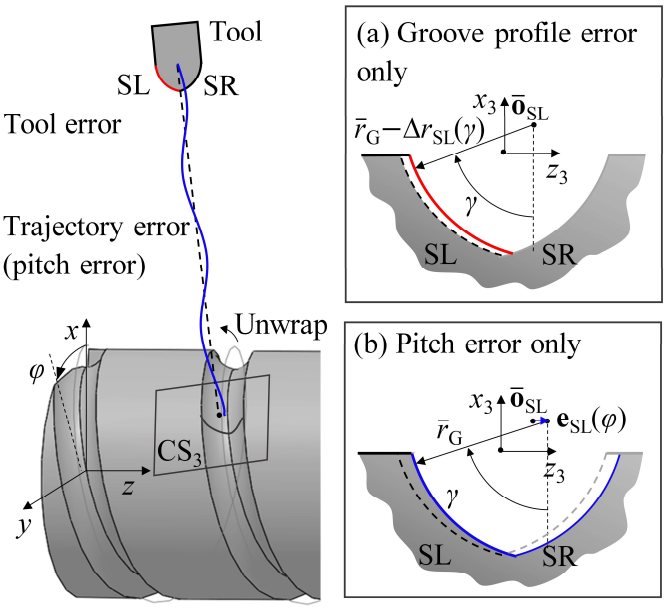

Figure 2.13: Illustration of (a) groove profile error; and (b) pitch error

Figure 2.14 shows the contact force distribution on four contact points as each geometric error category is applied separately to the setup of Case Study 1. The effect of groove profile errors is shown in Figure 2.14 (a); they do not change the load distribution significantly relative to the no-error case. The reason is that the defined groove profile errors are the same for all balls (i.e., it is independent of φ) and all balls are identical (without radial errors). Sinusoidal pitch errors however change the overall load distribution significantly (see Figure 2.14 (a)) because, unlike the defined groove profile errors, pitch errors depend on φ thus affecting the load distribution in a periodic manner, even with errorless balls. The load distribution under normally distributed ball radius errors is shown in Figure 2.14 (a); it causes significant differences in load distribution compared to the errorless case. Notice that with the introduction of each type of geometric error separately, all balls still maintain two-point contact with groove, as in the errorless case. Figure 15(b) shows the load distribution resulting from a combination of all three error types; the contact loads on the SL and NR surfaces are modified to some extent and some balls develop contact forces on their SR and NL surfaces.

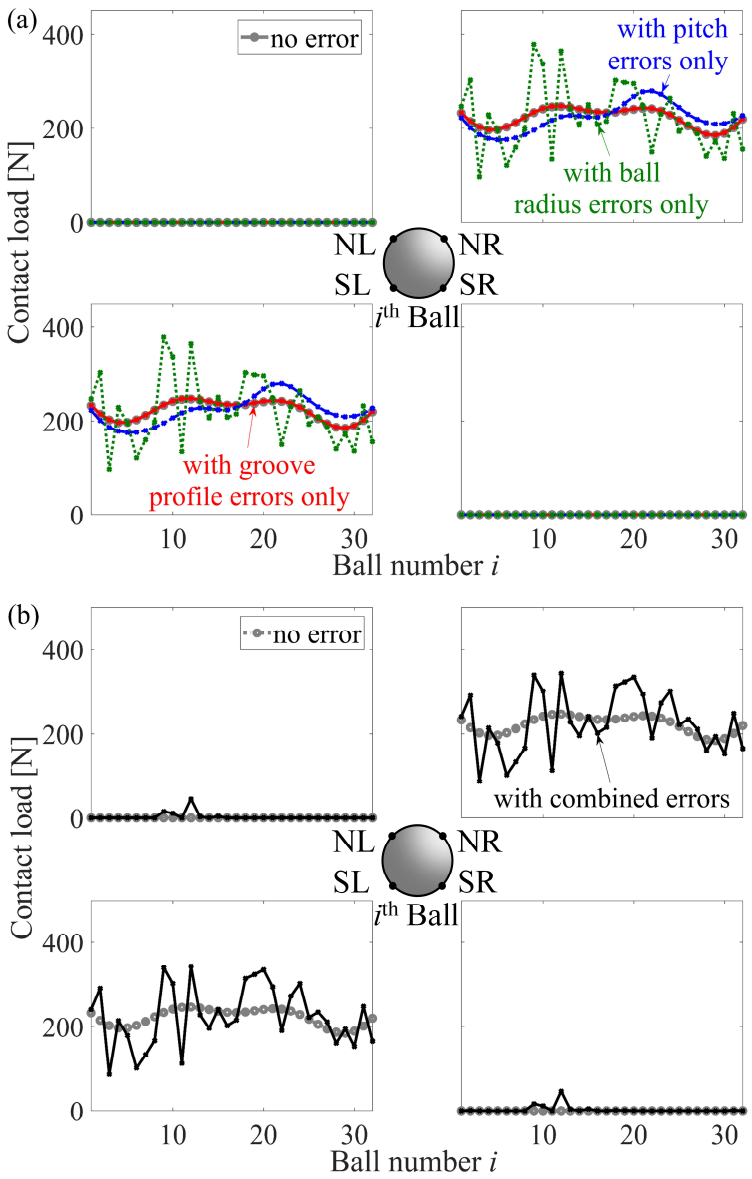

Figure 2.14: The effect of: (a) groove profile errors, sinusoidal pitch errors, normally distributed ball radius errors, each acting separately; (b) all three error types combined on load distribution

This case study shows the relative ease of describing and analyzing various kinds of geometric errors using the proposed low order model, as is possible using parametric 3-D FE models (but with much more tedious modeling effort and computational time).

2.5 Summary

This chapter has presented a low order static load distribution model for ball screw considering the effect of elastic deformations and geometric errors. Groove surfaces of ball screw are described mathematically using multivariate functions, thus providing versatility in

characterizing geometric errors, while balls are assumed to be spherical but capable of ball radius error. A contact model based on Hertzian Contact Theory is used to establish ball-to-groove contact including geometric errors for ball screw. Effects of axial, torsional and lateral elastic deformations are incorporated into the contact model by representing the nut as a rigid body and the screw as beam finite elements.

Benchmarked against an elaborate 3-D finite element (FE) model created in ANSYS Workbench 16.2, the proposed model is shown in case studies to be accurate in predicting load distribution in a ball screw with and without geometric error. However, an existing low order model, which considers axial deformation but not lateral deformation effects, exhibits significant errors in predicting load distribution, even when only axial loads are applied to the ball screw. Moreover, compared to the ANSYS model, the proposed model is shown to be much less complex and computationally expensive, while providing the kind of versatility in describing and analyzing different types of geometric errors tenable in 3-D FE models. It is therefore more convenient for use in parametric studies and design optimization of ball screws.

The developed static load distribution model for ball screw can be applied to ball bearings as well. Ball bearings can be treated as a special ball screw with zero pitch in the groove surface description process. Ball bearing does not have the slender screw shaft, thus the inner ring of it can be treated as a rigid body.

The proposed static load distribution model serves as the starting point for friction dynamics modeling of ball screw in next chapter. Static load distribution predicted by the proposed model is also useful for sizing and optimal design of ball screw, considering effects of various types of manufacturing errors and elastic deformations. The developed load distribution model is applied to ball screw used in EPAS gear in Chapter 4.

Chapter 3 Friction Modeling of Ball Bearings and Ball Screws

3.1 Overview

This chapter focuses on modeling contact-related friction behavior of ball bearings and ball screws. Two sources of friction variation are examined.

The first is ball-to-groove contact friction. A sensitivity analysis of friction to the rolling, sliding and spin motions in four-point contact ball bearing is presented. To do this, a well-established friction modeling process in the literature is followed but a simplifying assumption of planar contact area is applied which leads to elegant analytical formulations. In a case study, sliding and spin in four-point contact operation is shown to result in much higher ball-to-groove friction than two-point contact operation which mainly has rolling.

The second source of friction variation is from ball-to-ball contact typically happening in linear ball bearings and ball screws, which usually do not have cages. A low order velocity difference driven ball-to-ball contact model for linear ball bearings at steady state is first proposed. Based on friction analysis and relevant approximations, an analytical model for velocity deviation and ball-to-ball contact force and friction is derived for four-point contact linear ball bearings. The insight gained from the model is used in a case study to mitigate ball-to-ball contact. The proposed ball-to-ball contact models are also validated against ANSYS FEA results. A similar velocity difference driven ball-to-ball contact model is then derived for ball screws with ANSYS validation. Significant friction increase and variation due to ball-to-ball contact are demonstrated in a case study of ball screw, highlighting the importance of modeling ball-to-ball contact.

The chapter is organized as follows: sensitivity analysis of ball-to-groove friction to rolling, sliding and spin in a ball from four-point contact ball bearing is presented in Section 3.2. Ball-to-ball contact modeling for linear ball bearings is then discussed in Section 3.3, followed by ball-to-ball contact modeling for ball screws in Section 3.4. Finally, Section 3.5 provides a summary of the chapter.

3.2 Sensitivity Analysis of Rolling, Sliding and Spin in Four-point Contact Ball Bearing

The three kinds of motion a ball can have at the contact interface with groove - rolling, sliding and spin have drastically different friction behavior. In this subsection, a sensitivity analysis of ball-to-groove contact friction to rolling, sliding and spin is conducted with a ball from four-point contact ball bearing. The sensitivity analysis has very important implications for the application of four-point contact ball bearing as presented in Section 4.3.1.

3.2.1 Ball Motion and Friction Modeling in Four-point Contact Ball Bearing

There are many friction models in the literature developed for rotary ball bearings [29,52–55]. Here, a brief summary of the modeling process is given with simplifying assumption of planar contact area. Without loss of generality, ball motion and friction modeling are presented using a basic module of a four-point-contact rotary ball bearing as shown in Figure 3.1. The global coordinate system (CS=$\{x, y, z\}$) is established at the center of the ball bearing with its x-axis pointing along the ball bearing axis as shown in Figure 3.1. Relative to CS, the outer ring is fixed and the inner ring is moving at a constant angular velocity of magnitude ω_I about the x-axis (i.e., $\mathbf{\Omega}_I=\{\omega_I, 0, 0\}^T$ in vector form).

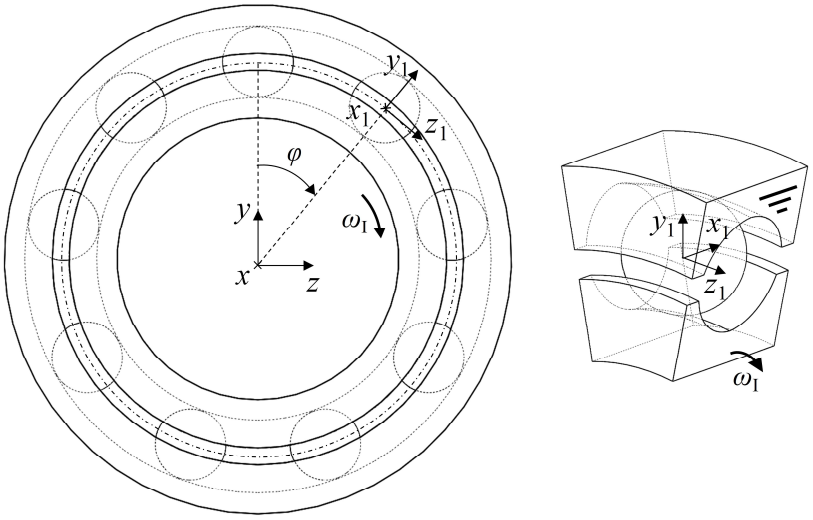

Figure 3.1: Basic module of a ball in a four-point-contact rotary ball bearing

The locus of points lying on the nominal ball center pathway relative to the origin of CS is expressed as

$$\overline{\mathbf{q}}_{\mathrm{B}}(\varphi)=\begin{Bmatrix}0\\ \overline{R}_{\mathrm{P}}\cos\varphi\\ \overline{R}_{\mathrm{P}}\sin\varphi\end{Bmatrix} \tag{3.1}$$

where φ is the angular distance traversed along the nominal ball center pathway starting from the y-axis to the ball location of interest (φ is usually referred to as the azimuth angle); $\overline{R}_{\mathrm{P}}$ is the nominal pitch circle radius of the ball bearing. Ignoring effects of elastic deformations and geometric errors on the grooves, the ball center velocity in the global coordinate system CS is expressed as

$$\mathbf{v}_{\mathrm{B}}(\varphi)=\begin{Bmatrix}0\\ -\overline{R}_{\mathrm{P}}\sin\varphi\omega_{\mathrm{B}}\\ \overline{R}_{\mathrm{P}}\cos\varphi\omega_{\mathrm{B}}\end{Bmatrix} \tag{3.2}$$

where ω_{B} is the orbiting angular velocity of the ball about the ball bearing axis.

A moving coordinate system $\mathrm{CS}_1=\{x_1, y_1, z_1\}$, with its origin on the nominal ball center pathway, is established such that its z_1-axis is tangent to the ball center pathway and its y_1-axis points along the radial line from ball bearing axis to nominal ball center as shown in Figure 3.1. Figure 3.2 depicts the cross section of a single ball in the x_1-y_1 plane. The ball, with radius R_{B}, is in four-point contact with the IL, IR, OR and OL (representing Inner/Outer ring and Left/Right) grooves of the raceway. Contact angles $\beta_{\mathrm{IL}}, \beta_{\mathrm{IR}}, \beta_{\mathrm{OR}}$ and β_{OL} are measured from $\pm y_1$-axis to the corresponding contact normal in the cross section (see Figure 3.2). Local coordinate systems $\mathrm{CS}_{\mathrm{IL}}$, $\mathrm{CS}_{\mathrm{IR}}$, $\mathrm{CS}_{\mathrm{OR}}$ and $\mathrm{CS}_{\mathrm{OL}}$ are established at the corresponding contact centers such that local z-axes are parallel to the z_1-axis and local y-axes lie along the corresponding contact normal, as shown for $\mathrm{CS}_{\mathrm{IL}}$ in Figure 3.2. The contact area is spread over each of the ball-groove contact interface. Since the contact area is relatively small compared to the ball radius, it is assumed to be in the local x-z plane in this work, as shown in Figure 3.2 for x_{IL}-z_{IL}.

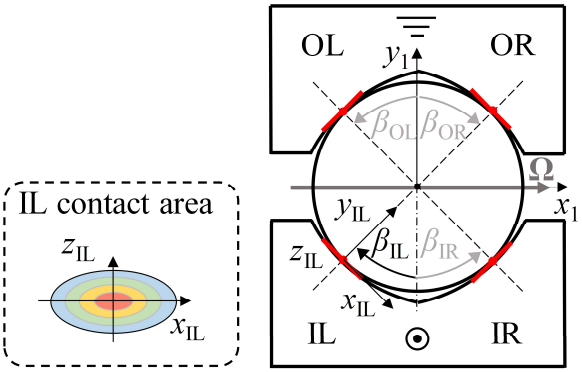

Figure 3.2: Geometry and coordinate systems for a four-point contact rotary ball bearing (highlighting the IL contact area)

The movement of the inner ring at ω_I not only makes the ball to orbit around the ball bearing axis at ω_B, but also makes the ball to rotate about its own axis. Assume, at quasi-static state, that the ball rotates with $\boldsymbol{\omega}$ ($=\{\omega_x, \omega_y, \omega_z\}^T$) about an axis passing through the ball center, measured in CS_1. Velocities of any point in the contact area on both ball side and groove side can be expressed based on rigid body kinematics. Focusing on the IL contact area, $\mathbf{q}_{IL}$ is defined as the vector from the ball center to the IL contact center and is given in CS_1 as

$$\mathbf{q}_{IL} = \begin{Bmatrix} -R_B \sin\beta_{IL} \\ -R_B \cos\beta_{IL} \\ 0 \end{Bmatrix} \tag{3.3}$$

For any point with local coordinates $(x_{IL}, z_{IL})^T$ in the contact area, its position in CS_1 is

$$\mathbf{q}_{IL,B} = \mathbf{q}_{IL} + \mathbf{T}_{CS\text{-}CS_{IL}} \{x_{IL}, 0, z_{IL}\}^T \tag{3.4}$$

where $\mathbf{T}_{CS\text{-}CS_{IL}}$ is the transformation matrix from CS_{IL} to CS given by

$$\mathbf{T}_{CS\text{-}CS_{IL}} = \begin{bmatrix} \cos\beta_{IL} & \sin\beta_{IL} & 0 \\ -\sin\beta_{IL} & \cos\beta_{IL} & 0 \\ 0 & 0 & 1 \end{bmatrix} \tag{3.5}$$

The linear velocity at the IL contact area on the ball side in CS can be expressed as

$$\mathbf{v}_{IL,B} = \mathbf{T}_{CS\text{-}CS_1} \left(\boldsymbol{\omega} \times \mathbf{q}_{IL,B}\right) + \dot{\mathbf{T}}_{CS\text{-}CS_1} \mathbf{q}_{IL,B} + \mathbf{v}_B \tag{3.6}$$

$\mathbf{T}_{CS\text{-}CS_1}$ is the transformation matrix between the global coordinate system CS and the local coordinate system CS_1 given as

$$\mathbf{T}_{CS\text{-}CS_1} = \mathrm{rot}_z(\varphi) \tag{3.7}$$

where rot(·) represents a current frame rotation operation about the axis specified by its subscript, as further described in Appendix A.

The linear velocity at the IL contact area on the groove side in CS is expressed as

$$\mathbf{v}_{\mathrm{IL,G}} = \boldsymbol{\Omega}_{\mathrm{I}} \times \left(\mathbf{T}_{\mathrm{CS\text{-}CS_I}} \mathbf{q}_{\mathrm{IL,B}} + \bar{\mathbf{q}}_{\mathrm{B}} \right) \tag{3.8}$$

Thus the relative velocity at any point in the IL contact area is

$$\Delta\mathbf{v}_{\mathrm{IL,B}} = \mathbf{v}_{\mathrm{IL,B}} - \mathbf{v}_{\mathrm{IL,G}} \tag{3.9}$$

The relative velocity expressed in the contact plane (i.e., x_{IL}-z_{IL} plane) can be calculated by coordinate transformation as

$$\begin{aligned} \left(\Delta\mathbf{v}_{\mathrm{IL,B}}\right)_{\mathrm{IL}} &= \begin{Bmatrix} \left(\Delta\mathbf{v}_{\mathrm{IL,B}}\right)_{\mathrm{IL},x} \\ \left(\Delta\mathbf{v}_{\mathrm{IL,B}}\right)_{\mathrm{IL},z} \end{Bmatrix} = \begin{bmatrix} 1 & 0 & 0 \\ 0 & 0 & 1 \end{bmatrix} \mathbf{T}_{\mathrm{CS\text{-}CS_{IL}}}{}^{-1} \mathbf{T}_{\mathrm{CS\text{-}CS_I}}{}^{-1} \Delta\mathbf{v}_{\mathrm{IL,B}} \\ &= \begin{Bmatrix} \omega_z R_{\mathrm{B}} + \omega_{\mathrm{IL}} z_{\mathrm{IL}} \\ \left(R_{\mathrm{P}} - R_{\mathrm{B}} \cos\beta_{\mathrm{IL}}\right)\left(\omega_{\mathrm{B}} - \omega_{\mathrm{I}}\right) - R_{\mathrm{B}} \cos\beta_{\mathrm{IL}} \omega_x + R_{\mathrm{B}} \sin\beta_{\mathrm{IL}} \omega_y - \omega_{\mathrm{IL}} x_{\mathrm{IL}} \end{Bmatrix}, \\ \omega_{\mathrm{IL}} &= \left(\omega_{\mathrm{B}} - \omega_{\mathrm{I}}\right)\sin\beta_{\mathrm{IL}} + \omega_y \cos\beta_{\mathrm{IL}} + \omega_x \sin\beta_{\mathrm{IL}} \end{aligned} \tag{3.10}$$

Define

$$\begin{aligned} \omega_{\mathrm{IL}} &= \left(\omega_{\mathrm{B}} - \omega_{\mathrm{I}}\right)\sin\beta_{\mathrm{IL}} + \omega_y \cos\beta_{\mathrm{IL}} + \omega_x \sin\beta_{\mathrm{IL}}, \\ c_{\mathrm{IL}} &= \frac{\left(R_{\mathrm{P}} - R_{\mathrm{B}} \cos\beta_{\mathrm{IL}}\right)\left(\omega_{\mathrm{B}} - \omega_{\mathrm{I}}\right) - R_{\mathrm{B}} \cos\beta_{\mathrm{IL}} \omega_x + R_{\mathrm{B}} \sin\beta_{\mathrm{IL}} \omega_y}{\omega_{\mathrm{IL}}}, \\ d_{\mathrm{IL}} &= -\frac{\omega_z R_{\mathrm{B}}}{\omega_{\mathrm{IL}}} \end{aligned} \tag{3.11}$$

The relative velocity field in Eq. (3.10) is rewritten as

$$\begin{Bmatrix} \left(\Delta\mathbf{v}_{\mathrm{IL,B}}\right)_{\mathrm{IL},x} \\ \left(\Delta\mathbf{v}_{\mathrm{IL,B}}\right)_{\mathrm{IL},z} \end{Bmatrix} = \begin{Bmatrix} \omega_{\mathrm{IL}} \left(-d_{\mathrm{IL}} + z_{\mathrm{IL}}\right) \\ \omega_{\mathrm{IL}} \left(c_{\mathrm{IL}} - x_{\mathrm{IL}}\right) \end{Bmatrix} \tag{3.12}$$

Following the same procedure, the relative velocity fields in the corresponding contact planes for other contact area can also be derived as

$$
\begin{aligned}
&\begin{Bmatrix} \left(\Delta\mathbf{v}_{\mathrm{IR,B}}\right)_{\mathrm{IR},x} \\ \left(\Delta\mathbf{v}_{\mathrm{IR,B}}\right)_{\mathrm{IR},z} \end{Bmatrix} = \begin{Bmatrix} \omega_{\mathrm{IR}}\left(-d_{\mathrm{IR}}+z_{\mathrm{IR}}\right) \\ \omega_{\mathrm{IR}}\left(c_{\mathrm{IR}}-x_{\mathrm{IR}}\right) \end{Bmatrix} \\
&= \begin{Bmatrix} R_{\mathrm{B}}\omega_z - \omega_{\mathrm{IR}} z_{\mathrm{IR}} \\ \left(R_{\mathrm{P}}-R_{\mathrm{B}}\cos\beta_{\mathrm{IR}}\right)\left(\omega_{\mathrm{B}}-\omega_{\mathrm{I}}\right) - R_{\mathrm{B}}\cos\beta_{\mathrm{IR}}\omega_x - R_{\mathrm{B}}\sin\beta_{\mathrm{IR}}\omega_y + \omega_{\mathrm{IR}} x_{\mathrm{IR}} \end{Bmatrix}, \\
&\omega_{\mathrm{IR}} = \left(\omega_{\mathrm{B}}-\omega_{\mathrm{I}}\right)\sin\beta_{\mathrm{IR}} - \omega_y\cos\beta_{\mathrm{IR}} + \omega_x\sin\beta_{\mathrm{IR}}, \\
&\begin{Bmatrix} \left(\Delta\mathbf{v}_{\mathrm{OR,B}}\right)_{\mathrm{OR},x} \\ \left(\Delta\mathbf{v}_{\mathrm{OR,B}}\right)_{\mathrm{OR},z} \end{Bmatrix} = \begin{Bmatrix} \omega_{\mathrm{OR}}\left(-d_{\mathrm{OR}}+z_{\mathrm{OR}}\right) \\ \omega_{\mathrm{OR}}\left(c_{\mathrm{OR}}-x_{\mathrm{OR}}\right) \end{Bmatrix} \\
&= \begin{Bmatrix} R_{\mathrm{B}}\omega_z - \omega_{\mathrm{OR}} z_{\mathrm{OR}} \\ \left(R_{\mathrm{P}}+R_{\mathrm{B}}\cos\beta_{\mathrm{OR}}\right)\omega_{\mathrm{B}} + R_{\mathrm{B}}\cos\beta_{\mathrm{OR}}\omega_x - R_{\mathrm{B}}\sin\beta_{\mathrm{OR}}\omega_y + \omega_{\mathrm{OR}} x_{\mathrm{OR}} \end{Bmatrix}, \\
&\omega_{\mathrm{OR}} = \omega_{\mathrm{B}}\sin\beta_{\mathrm{OR}} + \omega_y\cos\beta_{\mathrm{OR}} + \omega_x\sin\beta_{\mathrm{OR}}, \\
&\begin{Bmatrix} \left(\Delta\mathbf{v}_{\mathrm{OL,B}}\right)_{\mathrm{OL},x} \\ \left(\Delta\mathbf{v}_{\mathrm{OL,B}}\right)_{\mathrm{OL},z} \end{Bmatrix} = \begin{Bmatrix} \omega_{\mathrm{OL}}\left(-d_{\mathrm{OL}}+z_{\mathrm{OL}}\right) \\ \omega_{\mathrm{OL}}\left(c_{\mathrm{OL}}-x_{\mathrm{OL}}\right) \end{Bmatrix} \\
&= \begin{Bmatrix} R_{\mathrm{B}}\omega_z + \omega_{\mathrm{OL}} z_{\mathrm{OL}} \\ \left(R_{\mathrm{P}}+R_{\mathrm{B}}\cos\beta_{\mathrm{OL}}\right)\omega_{\mathrm{B}} + R_{\mathrm{B}}\cos\beta_{\mathrm{OL}}\omega_x + R_{\mathrm{B}}\sin\beta_{\mathrm{OL}}\omega_y - \omega_{\mathrm{OL}} x_{\mathrm{OL}} \end{Bmatrix}, \\
&\omega_{\mathrm{OL}} = \omega_{\mathrm{B}}\sin\beta_{\mathrm{OL}} - \omega_y\cos\beta_{\mathrm{OL}} + \omega_x\sin\beta_{\mathrm{OL}}
\end{aligned}
\tag{3.13}
$$

It is observed that the relative velocity field in the elliptical contact area (with semi-major axis a_i and semi-minor axis b_i) is a circular contour centered at (c_i, d_i) as shown in Figure 3.3 (a), with $i \in \{\mathrm{IL,IR,OR,OL}\}$ representing different contact area. Notice that the center of the contour represents the zero-velocity point. Another observation about the velocity field in Eqs. (3.10) and (3.13) is that the offset in the x_i-component (local x-component) are all $R_{\mathrm{B}}\omega_z$, which is induced by the rotation of the ball around the z_1-axis. It can be proven that the same offset gives rise to frictional forces in all positive or all negative local x-direction for all four contact points if $\omega_z \neq 0$. In that case, frictional moment about the z_1-axis is non-zero, which is not feasible for the quasi-static state. In order for the quasi-static state to hold, $\omega_z = 0$ has to be enforced. Thus $d_i = 0$ as shown in Figure 3.3 (b) is the case for all four contact points in rotary ball bearings.

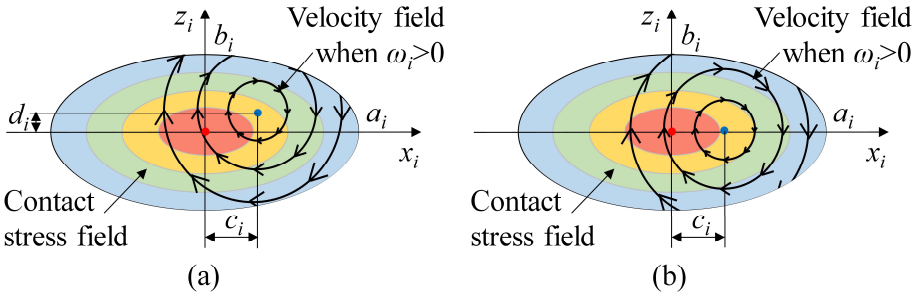

Figure 3.3: Contact area and velocity field: (a) $\omega_z \neq 0$; (b) $\omega_z = 0$ is enforced (rotary ball bearing)

From now on, the discussion for rotary ball bearing will be only focused on the case $d_i = 0$, where velocity center is always on the semi-major axis of the elliptical contact area. The velocity field for the four contact areas in Eqs. (3.10) and (3.13) are represented by a common formula as

$$\begin{Bmatrix} \left(\Delta \mathbf{v}_{i,\mathrm{B}}\right)_{i,x} \\ \left(\Delta \mathbf{v}_{i,\mathrm{B}}\right)_{i,z} \end{Bmatrix} = \begin{Bmatrix} \omega_i z_i \\ \omega_i \left(c_i - x_i\right) \end{Bmatrix}, i \in \{\mathrm{IL}, \mathrm{IR}, \mathrm{OR}, \mathrm{OL}\} \tag{3.14}$$

It is worth noting that the derivation of velocity field in the contact area for ball bearing has been noted in many comprehensive friction models in the literature [29,52–55]. However, with the planar contact area approximation made in this work, an elegant expression of velocity field is obtained as circular contours, which is very helpful for the analysis of friction.

Given the relative velocity field over the assumed planar contact area, friction is calculated by double integrating the infinitesimal frictional stress with normal contact stress distribution. It is a standard process that many friction models have adopted [29,52–55]. But with the planar contact area approximation and the velocity field derived in Eq. (3.14), friction can be analyzed explicitly [72]. The normal contact stress field indicated by the color map in Figure 3.3 is described by Hertzian Contact Theory as

$$\sigma_i = \sigma_{i,0} \left(1 - \frac{x_i^2}{a_i^2} - \frac{z_i^2}{b_i^2}\right)^{1/2}, \sigma_{i,0} = \frac{3F_i}{2\pi a_i b_i} \tag{3.15}$$

where a_i and b_i are determined given the contact surface geometry and normal contact force F_i for each contact area, the details of their calculation are shown for ball screws in Appendix B, but the same process can be applied to ball bearings. In Eq. (3.15), $\sigma_{i,0}$ is the maximum contact pressure. Given the symmetry of the contact stress field and velocity field about the x_i-axis in Figure 3.3 (b), the frictional force along x_i-axis is zero. Frictional force $f_{i,z}$ along z_i-axis,

frictional moment $M_{i,O}$ about contact center and frictional loss P_{fi} measured in power are calculated by double integrating the frictional stress over the contact area as

$$
\begin{aligned}
f_{i,z} &= \operatorname{sgn}(\omega_i)\iint_D \mu\sigma_{i,0}\left(1-\frac{x_i^2}{a_i^2}-\frac{z_i^2}{b_i^2}\right)^{1/2}\frac{x_i-c_i}{\sqrt{(x_i-c_i)^2+z_i^2}}dx_i dz_i \\
&= \operatorname{sgn}(\omega_i)a_i b_i \mu\sigma_{i,0}\iint_D \left(1-t^2-s^2\right)^{1/2}\frac{t-c_i/a_i}{\sqrt{(t-c_i/a_i)^2+(b_i/a_i\cdot s)^2}}dsdt \quad \left(t=\frac{x_i}{a_i}, s=\frac{z_i}{b_i}, D: t^2+s^2\le 1\right) \\
&= \operatorname{sgn}(\omega_i)a_i b_i \mu\sigma_{i,0}\int_0^{2\pi}\int_0^1 \left(1-r^2\right)^{1/2}\frac{r\cos\theta-c_i/a_i}{\sqrt{(r\cos\theta-c_i/a_i)^2+(b_i/a_i\cdot r\sin\theta)^2}}rdrd\theta \quad (r\cos\theta=t, r\sin\theta=s)
\end{aligned}
\tag{3.16}
$$

$$
\begin{aligned}
M_{i,O} &= \operatorname{sgn}(\omega_i)\iint_D \mu\sigma_{i,0}\left(1-\frac{x_i^2}{a_i^2}-\frac{z_i^2}{b_i^2}\right)^{1/2}\left(\frac{x_i-c_i}{\sqrt{(x_i-c_i)^2+z_i^2}}x_i-\frac{-z_i}{\sqrt{(x_i-c_i)^2+z_i^2}}z_i\right)dx_i dz_i \\
&= \operatorname{sgn}(\omega_i)a_i^2 b_i \mu\sigma_{i,0}\iint_D \left(1-t^2-s^2\right)^{1/2}\left(\frac{t^2-c_i/a_i t+b_i^2/a_i^2 s^2}{\sqrt{(t-c_i/a_i)^2+(b_i/a_i\cdot s)^2}}\right)dsdt \\
&= \operatorname{sgn}(\omega_i)a_i^2 b_i \mu\sigma_{i,0}\int_0^{2\pi}\int_0^1 \left(1-r^2\right)^{1/2}\left(\frac{r^2\cos\theta^2-c_i/a_i r\cos\theta+b_i^2/a_i^2 r^2\sin\theta^2}{\sqrt{(r\cos\theta-c_i/a_i)^2+(b_i/a_i\cdot r\sin\theta)^2}}\right)rdrd\theta
\end{aligned}
\tag{3.17}
$$

$$
\begin{aligned}
P_{fi} &= |\omega_i|\iint_D \mu\sigma_{i,0}\left(1-\frac{x_i^2}{a_i^2}-\frac{z_i^2}{b_i^2}\right)^{1/2}\sqrt{(x_i-c_i)^2+z_i^2}\,dx_i dz_i \\
&= |\omega_i|a_i^2 b_i \mu\sigma_{i,0}\iint_D \left(1-t^2-s^2\right)^{1/2}\sqrt{(t-c_i/a_i)^2+(b_i/a_i\cdot s)^2}\,dsdt \\
&= |\omega_i|a_i^2 b_i \mu\sigma_{i,0}\int_0^{2\pi}\int_0^1 \left(1-r^2\right)^{1/2}\sqrt{(r\cos\theta-c_i/a_i)^2+(b_i/a_i\cdot r\sin\theta)^2}\,rdrd\theta
\end{aligned}
\tag{3.18}
$$

Since the frictional forces are in the z_i-direction and the frictional moments are about y_i-axes, friction is decoupled from normal contact forces which lie in the x_1-y_1 plane. Thus the friction can be calculated independently after load distribution is calculated as shown in Chapter 2. It is found that centrifugal and gyroscopic effect is negligible in low speed application (like EPAS) [52,56]. Ignoring centrifugal and gyroscopic effect, the ball needs to be in quasi-static equilibrium under frictional forces and moments as

$$\sum\begin{pmatrix}\mathbf{F}\\ \mathbf{M}\end{pmatrix}_0=\begin{bmatrix}1 & 1 & 1 & 1\\ -\cos\beta_{\mathrm{IL}} & -\cos\beta_{\mathrm{IR}} & \cos\beta_{\mathrm{OR}} & \cos\beta_{\mathrm{OL}}\\ \sin\beta_{\mathrm{IL}} & -\sin\beta_{\mathrm{IR}} & -\sin\beta_{\mathrm{OR}} & \sin\beta_{\mathrm{OL}}\end{bmatrix}\begin{Bmatrix}\mathrm{Sig}(\omega_{\mathrm{IL}}/\Delta\omega)f_{\mathrm{IL},z}\\ \mathrm{Sig}(\omega_{\mathrm{IR}}/\Delta\omega)f_{\mathrm{IR},z}\\ \mathrm{Sig}(\omega_{\mathrm{OR}}/\Delta\omega)f_{\mathrm{OR},z}\\ \mathrm{Sig}(\omega_{\mathrm{OL}}/\Delta\omega)f_{\mathrm{OL},z}\end{Bmatrix}$$
$$+\begin{bmatrix}0 & 0 & 0 & 0\\ \sin\beta_{\mathrm{IL}} & -\sin\beta_{\mathrm{IR}} & -\sin\beta_{\mathrm{OR}} & \sin\beta_{\mathrm{OL}}\\ \cos\beta_{\mathrm{IL}} & \cos\beta_{\mathrm{IR}} & -\cos\beta_{\mathrm{OR}} & -\cos\beta_{\mathrm{OL}}\end{bmatrix}\begin{Bmatrix}-\mathrm{Sig}(\omega_{\mathrm{IL}}/\Delta\omega)M_{\mathrm{IL},O}/R_{\mathrm{B}}\\ -\mathrm{Sig}(\omega_{\mathrm{IR}}/\Delta\omega)M_{\mathrm{IR},O}/R_{\mathrm{B}}\\ -\mathrm{Sig}(\omega_{\mathrm{OR}}/\Delta\omega)M_{\mathrm{OR},O}/R_{\mathrm{B}}\\ -\mathrm{Sig}(\omega_{\mathrm{OL}}/\Delta\omega)M_{\mathrm{OL},O}/R_{\mathrm{B}}\end{Bmatrix}=\begin{Bmatrix}0\\0\\0\end{Bmatrix} \tag{3.19}$$

where the first equation represents equilibrium of frictional forces in the z_1-direction. The second and third equations represent equilibrium of frictional moment about the x_1- and y_1-axis respectively, which are normalized by ball radius R_{B} to be equivalent force equations. It is worth noticing that there is minus sign before $M_{i,O}$ in Eq. (3.19), because $M_{i,O}$ is measured about the corresponding $-y_i$-axis as shown in Figure 3.3 (b). It is also worth noticing that sticking of the two mating surfaces happens when the relative velocity between them is small [52]. Here sticking is modeled by using a modified logistic Sigmoid function formulated as

$$\mathrm{Sig}(\omega_i/\Delta\omega)=2\frac{e^{k_{\mathrm{S}}\omega_i/\Delta\omega}}{e^{k_{\mathrm{S}}\omega_i/\Delta\omega}+1}-1 \tag{3.20}$$

where $\Delta\omega=\Delta\omega_{\mathrm{Br}}=\omega_{\mathrm{I}}\sin\bar{\beta}$ is the approximated relative spin velocity in the same diagonal contact pair (i.e., $|\omega_{\mathrm{IL}}-\omega_{\mathrm{OR}}|$ or $|\omega_{\mathrm{IR}}-\omega_{\mathrm{OL}}|$); k_{S} is a scaling factor. The modified logistic Sigmoid function with different k_{S} is plotted in Figure 3.4, it takes a value very close to 1 except when the spin velocity ω_i is close to zero. In near zero spin velocity, the frictional force, moment and loss are discounted to represent the stick phenomenon. Different values of k_{S} indicates different sensitivity level of the stick region to the relative spin velocity. The larger the k_{S} is, the closer the friction behavior is to Coulomb friction. However, the kinematic problem is also harder to solve because it is closer to a step function. In this work, k_{S}=100 is selected to facilitate stability of the numerical solver.

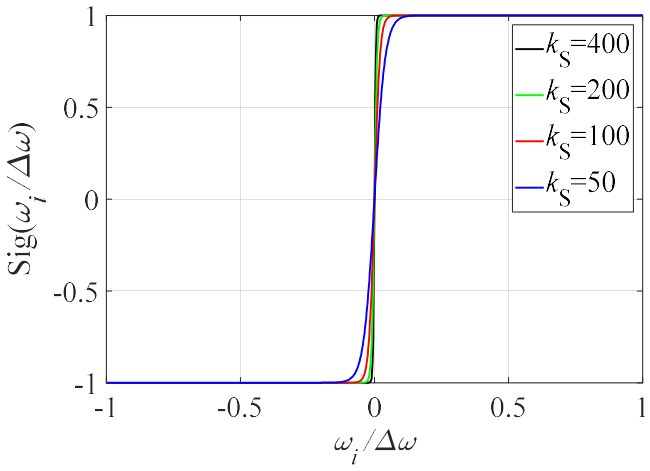

Figure 3.4: Modified logistic Sigmoid function with different scaling factors

With the three equations in Eq. (3.19), the three kinematic variables ω_B, ω_x and ω_y are solved in an iterative process using the *fsolve* function in MATLAB®. Maps of frictional force/moment/loss are built beforehand as functions of c_i/a_i according to equations presented in Eqs. (3.16)-(3.18). In the solution process, linear interpolation is used to retrieve the values to speed up the calculation instead of performing numerical integration. In summary, the process can be described by the flowchart as shown in Figure 3.5.

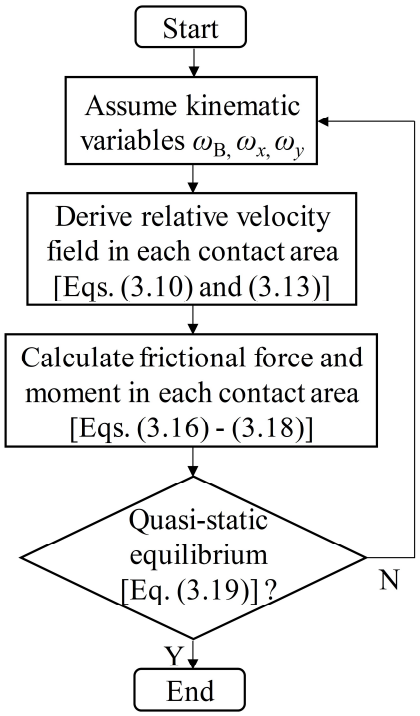

Figure 3.5: Flowchart for the solution process of ball motion and friction in rotary ball bearing

Upon the solution of the kinematic variables, frictional force/moment and loss in each contact area are determined according to Eqs. (3.16)-(3.18). The torque applied at the ball bearing axis to counter the friction (i.e., friction torque) is calculated as

$$M_f = \frac{\sum_i \mathrm{Sig}(\omega_i/\Delta\omega) P_{fi}}{\omega_1} \tag{3.21}$$

3.2.2 Sensitivity Analysis of Friction to Rolling, Sliding and Spin Motions

Now that the friction model is established for rotary ball bearing in the preceding subsection, a case study is conducted to show the sensitivity of ball-to-groove contact friction to rolling, sliding and spin motions. The loading and boundary conditions of the basic four-point contact module for the case study are shown in Figure 3.6: the inner ring is subjected to a constant lateral force F_x; at the same time it is offset by a displacement u_y in the vertical direction. The ball starts with two-point (2P) contact (i.e., in IL and OR contact points); as the vertical displacement u_y increases, four-point (4P) contact takes place. Since load distribution and friction are decoupled in rotary ball bearing, a two-step approach is taken to determine friction. Contact forces are calculated as a first step by adopting a load distribution model, similar to the one for ball screw presented in Chapter 2. Once the contact forces and contact angles are obtained, the kinematic states and friction are calculated in the second step following the procedure presented in Section 3.2.1.

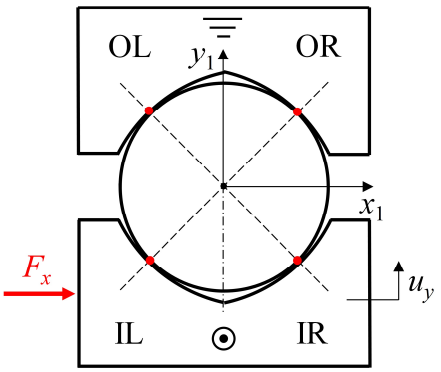

Figure 3.6: Loading and boundary conditions for rotary ball bearing case study

Parameters of the rotary ball beaaring for the case study are shown in Table 3.1, which are based on an actual ball bearing.

Table 3.1: Parameters for the rotary ball bearing case study

Parameter (Symbol)	Value [Unit]
Ball radius (R_B)	6.25 [mm]
Conformity ratio of groove (conf.= $R_G/2R_B$)	0.54
Pitch circle radius of ball bearing (R_P)	35 [mm]
Nominal contact angle (β)	45 [°]
Lateral force (F_x)	100 [N]
Angular velocity of the inner ring (ω_I)	10 [rps]
Friction coefficient (μ)	0.1
Young's modulus	2.1×10^{11} [N/m^2]
Poisson's ratio	0.28

The sum of contact forces as a function of the vertical displacement u_y of the inner ring is shown in Figure 3.7 (a) while the friction torque is shown in Figure 3.7 (b). It is observed in Figure 3.7 (a) that the sum of contact force remains nearly constant in the beginning because there is two-point contact and gradually builds up as four-point takes place. However, friction increases significantly as four-point contact happens. Figure 3.8 illustrates the relative velocity at the contact areas for three scenarios (i.e., case (I), (II) and (III) in Figure 3.7). Table 3.2 summarizes the contact forces, friction loss, friction torque and ball motion for the three scenarios. Compared to case (I), the sum of contact forces increases 5.48% in case (II) but the friction torque increases 4.22 times. In case (II), the transition from two-point contact to four-point contact happens, and sliding motion in IR and OL contact areas with higher relative velocity takes place as shown in Figure 3.8 (b). The sum of contact forces increases 67.58% but the friction torque increases 12.68 times in case (III) compared to case (I), due to the spin motion in all the four contact areas as shown in Figure 3.8 (c). As sliding turns into spin between case (II) and (III), the friction torque curve changes slope in Figure 3.7 (b). Based on the sensitivity analysis, friction torque increases significantly during the transition of two-point contact to four-point contact as sliding and spin motion with larger relative velocity (and higher friction loss) takes place.

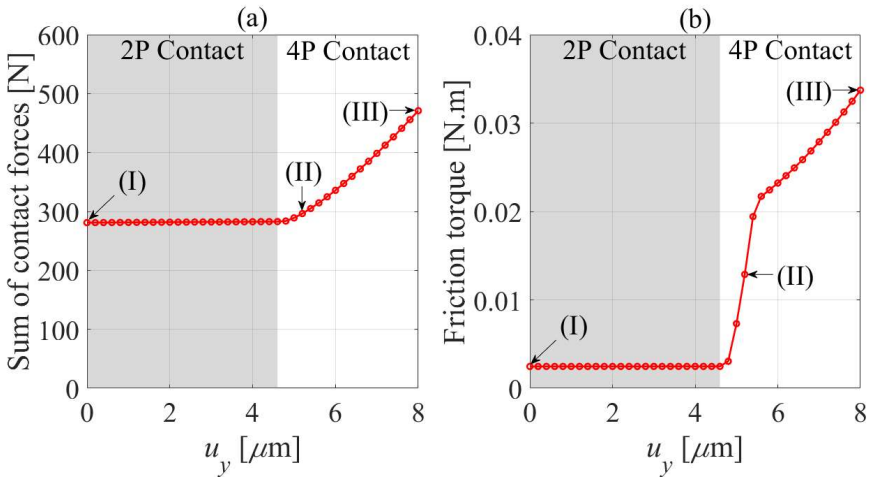

Figure 3.7: (a) Sum of contact forces; (b) friction torque

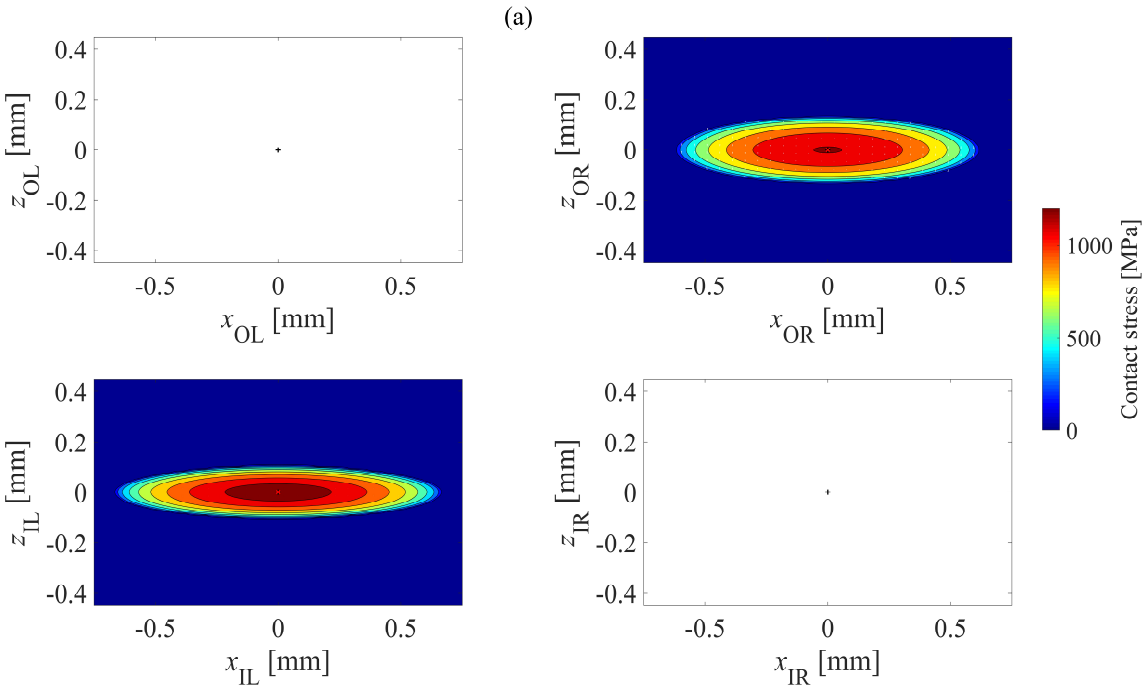

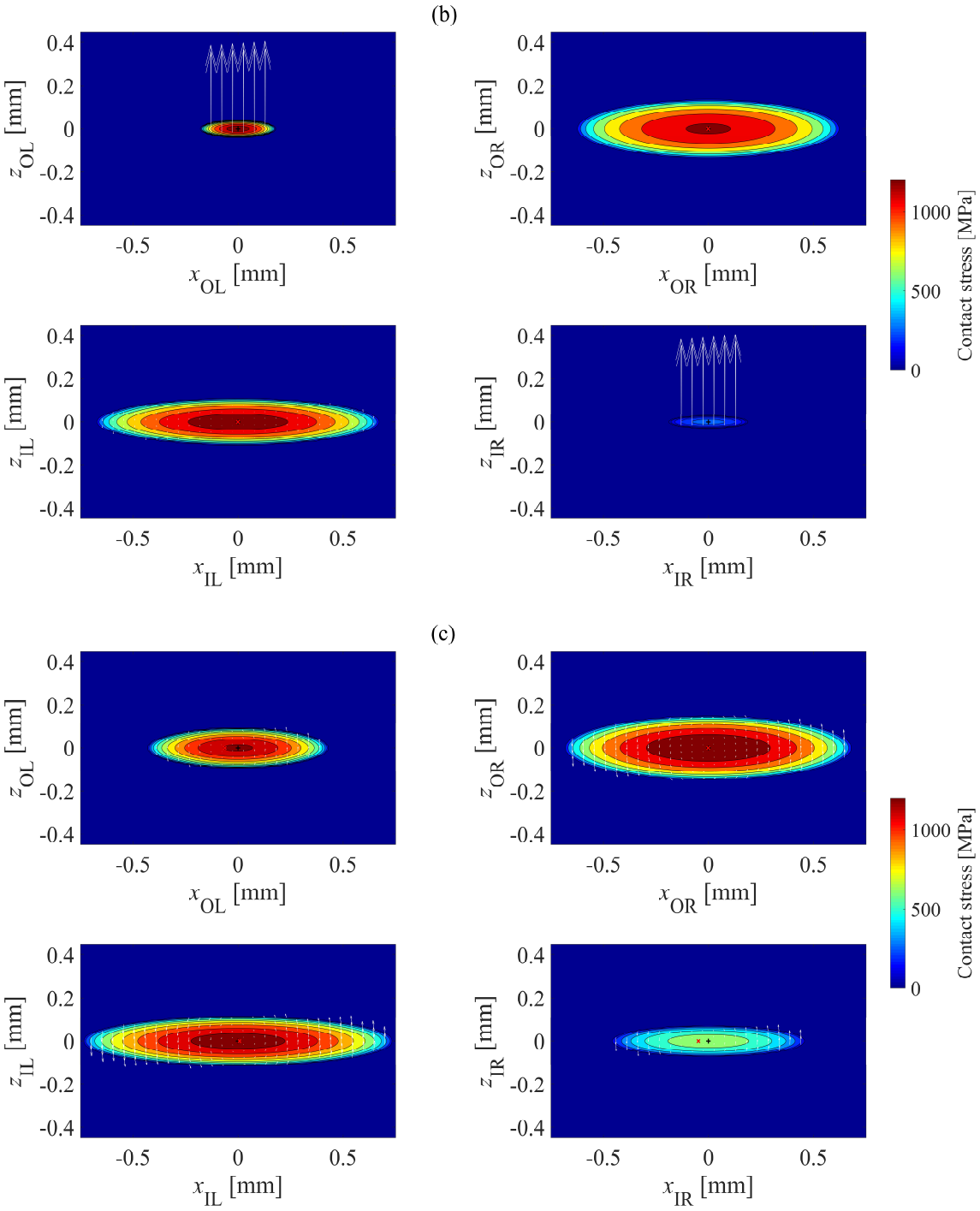

Figure 3.8: Velocity field in the four contact areas for: (a) two-point contact in Case (I); (b) four-point contact with sliding in Case (II) and (c) four-point contact with spin in Case (III) (Arrows represent relative velocity between ball and groove)

Table 3.2: Contact forces, friction loss, friction torque and ball motion for the three scenarios

	Case (I)	Case (II)	Case (III)
Contact forces [N]	F_{IL}=140.4945	F_{IL}=144.8352	F_{IL}=188.5374
	F_{IR}=0	F_{IR}=3.3582	F_{IR}=46.8926
	F_{OL}=0	F_{OL}=3.3643	F_{OL}=46.9413
	F_{OR}=140.4945	F_{OR}=144.8371	F_{OR}=188.5689
	$\sum_i F_i$ =280.9890	$\sum_i F_i$ =296.3948	$\sum_i F_i$ =434.8236
Friction loss [W]	$P_{f,IL}$= 0.0056	$P_{f,IL}$=0.1690	$P_{f,IL}$=1.0518
	$P_{f,IR}$=0	$P_{f,IR}$=0.3193	$P_{f,IR}$=0.1690
	$P_{f,OL}$=0	$P_{f,OL}$=0.3207	$P_{f,OL}$=0.1269
	$P_{f,OR}$=0.1493	$P_{f,OR}$=0.0000	$P_{f,OR}$=0.7709
	$\sum_i P_{f,i}$ =0.1549	$\sum_i P_{f,i}$ =0.8091	$\sum_i P_{f,i}$ =2.1186
Friction torque [N.mm]	2.4650	12.8769	33.7180
Ball motion [rad/s]	ω_B=27.4754	ω_B=27.4469	ω_B=27.4115
	ω_x=−104.8742	ω_x=−136.2569	ω_x=−242.2681
	ω_y=139.7872	ω_y=108.5585	ω_y=1.6094

The transition between rolling, sliding and spin in four-point contact bearing is shown to contribute to significant friction variation of four-point contact ball bearing in operation in Chapter 4.

3.3 Ball-to-ball Contact Modeling for Linear Ball Bearings

Cages are commonly adopted in rotary ball bearings to separate balls from contacting each other, but they are not commonly used in linear ball bearings and ball screws. As a result, ball-to-ball can happen and contribute to significant friction increase and variation [62,63]. It is of interest to model what contributes to ball-to-ball contact and how to mitigate it.

3.3.1 Ball Motion and Friction Modeling in Linear Ball Bearings

In order to model ball-to-ball contact between multiple balls in a linear ball bearing, a first step is to model the motion and friction of a single ball. Linear ball bearings share many common features as rotary ball bearings, and the modeling process presented in the preceding subsection applies to linear ball bearings with some modifications. Here, a brief summary is given.

Without loss of generality, ball motion and friction modeling are presented in the basic module of a four-point-contact linear ball bearing as shown in Figure 3.9. In the setup, the bottom groove is fixed and the top groove is moving at a constant velocity of magnitude v.

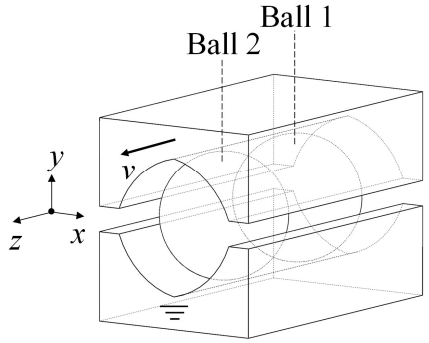

Figure 3.9: Basic module of two balls in a four-point-contact linear ball bearing

To analyze ball motion and friction, coordinate systems need to be established. Figure 3.10 depicts the cross section of a single ball in Figure 3.9. Define a global coordinate system (CS=$\{x,y,z\}$), fixed in space as shown in Figure 3.10, with its z-axis passing through the ball center pathway and its x-y plane parallel to the cross section of the raceway. The ball, with radius R_B, is in four-point contact with the BL, BR, TR and TL (representing Bottom/Top and Left/Right) grooves of the raceway. Contact angles β_{BL}, β_{BR}, β_{TR} and β_{TL} are measured from $\pm y$-axis to the corresponding contact normal in the cross section (see Figure 3.10). Notice the similarities between Figure 3.10 and Figure 3.2 for rotary ball bearing.

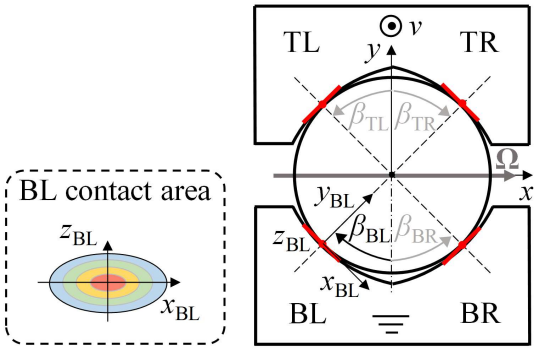

Figure 3.10: Geometry and coordinate systems for four-point contact

The movement of the top groove in the global z-direction at constant velocity v makes the ball to translate and rotate. Assume, at quasi-static state, that the ball translates with linear velocity v_B in the global z-direction (i.e., $\mathbf{v}_B=\{0,\ 0,\ v_B\}^T$ in vector form) and rotates with $\boldsymbol{\Omega}$ $(=\{\omega_x,\ \omega_y,\ 0\}^T)$ about an axis passing through the ball center. Velocities of any point in the contact area on both ball side and groove side can be expressed based on rigid body kinematics detailed in [72]. The process is very similar to the rotary ball bearing, thus it is not presented here for the sake of brevity. Taking the BL contact interface as an example, the relative velocity between the ball and the BL groove (denoted as $\Delta\mathbf{v}_{BL,B}$) at any point with local coordinates (x_{BL}, z_{BL}) in the contact plane is expressed as

$$\begin{Bmatrix}\left(\Delta\mathbf{v}_{BL,B}\right)_{BL,x}\\ \left(\Delta\mathbf{v}_{BL,B}\right)_{BL,z}\end{Bmatrix}=\begin{Bmatrix}R_B\omega_z+\left(\omega_x\sin\beta_{BL}+\omega_y\cos\beta_{BL}\right)z_{BL}\\ v_B-\left(\omega_x\cos\beta_{BL}-\omega_y\sin\beta_{BL}\right)R_B-\left(\omega_x\sin\beta_{BL}+\omega_y\cos\beta_{BL}\right)x_{BL}\end{Bmatrix} \tag{3.22}$$

For the same reason as in rotary ball bearing, the angular velocity of the ball about the z-axis should always be zero (i.e. $\omega_z=0$) in order for the frictional moment about the z-axis to be balanced [72].

Define

$$\begin{aligned}\omega_{BL}&=\omega_x\sin\beta_{BL}+\omega_y\cos\beta_{BL},\\ c_{BL}&=\frac{v_B-\left(\omega_x\cos\beta_{BL}-\omega_y\sin\beta_{BL}\right)R_B}{\omega_{BL}}\end{aligned} \tag{3.23}$$

the relative velocity field in Eq. (3.22) is rewritten as

$$\begin{Bmatrix}\left(\Delta\mathbf{v}_{BL,B}\right)_{BL,x}\\ \left(\Delta\mathbf{v}_{BL,B}\right)_{BL,z}\end{Bmatrix}=\begin{Bmatrix}\omega_{BL}z_{BL}\\ \omega_{BL}\left(c_{BL}-x_{BL}\right)\end{Bmatrix} \tag{3.24}$$

Following the same procedure, the relative velocity fields for the BR, TL and TR contact areas are also derived as shown in Appendix F. They take exactly the same general form as rotary ball bearing: they all appear as circular contours centered at (c_i, 0) as shown in Figure 3.3 (b), with $i \in$ {BL, BR, TR, TL}. Thus frictional force, moment and loss can be calculated the same as rotary ball bearing in Eqs. (3.16)-(3.18). Quasi-static equilibrium can be established ignoring gyroscopic effect, meaning that the ball needs to be in quasi-static equilibrium under frictional forces and moments as

$$\begin{aligned}\sum\begin{pmatrix}\mathbf{F}\\ \mathbf{M}\end{pmatrix}_0 &= \begin{bmatrix} 1 & 1 & 1 & 1 \\ -\cos\beta_{\mathrm{BL}} & -\cos\beta_{\mathrm{BR}} & \cos\beta_{\mathrm{TR}} & \cos\beta_{\mathrm{TL}} \\ \sin\beta_{\mathrm{BL}} & -\sin\beta_{\mathrm{BR}} & -\sin\beta_{\mathrm{TR}} & \sin\beta_{\mathrm{TL}} \end{bmatrix}\begin{Bmatrix} f_{\mathrm{BL},z} \\ f_{\mathrm{BR},z} \\ f_{\mathrm{TR},z} \\ f_{\mathrm{TL},z} \end{Bmatrix} \\ &+\begin{bmatrix} 0 & 0 & 0 & 0 \\ \sin\beta_{\mathrm{BL}} & -\sin\beta_{\mathrm{BR}} & -\sin\beta_{\mathrm{TR}} & \sin\beta_{\mathrm{TL}} \\ \cos\beta_{\mathrm{BL}} & \cos\beta_{\mathrm{BR}} & -\cos\beta_{\mathrm{TR}} & -\cos\beta_{\mathrm{TL}} \end{bmatrix}\begin{Bmatrix} -M_{\mathrm{BL},O}/R_{\mathrm{B}} \\ -M_{\mathrm{BR},O}/R_{\mathrm{B}} \\ -M_{\mathrm{TR},O}/R_{\mathrm{B}} \\ -M_{\mathrm{TL},O}/R_{\mathrm{B}} \end{Bmatrix} = \begin{Bmatrix} 0 \\ 0 \\ 0 \end{Bmatrix}\end{aligned} \tag{3.25}$$

3.3.2 Low Order Numerical Model of Ball-to-ball Contact for Linear Ball Bearings

The linear velocities of individual balls differ depending on their contact angles and loading conditions. Ball-to-ball contact develops: (1) when the linear velocity $v_{\mathrm{B},10}$ of the ball behind (Ball 1 in Figure 3.9) is larger than $v_{\mathrm{B},20}$ of the ball in front, i.e., $v_{\mathrm{B},10} > v_{\mathrm{B},20}$; and (2) when the distance between the two ball centers d_{12} is small enough ($d_{12} \le 2R_{\mathrm{B}}$). Note that "1" and "2" in the subscript denote the velocities pertaining to Ball 1 and 2 respectively; "0" is used to denote the velocity before ball-to-ball contact. After contact, ball-to-ball contact causes the two balls to eventually have the same linear velocity (i.e., $v_{\mathrm{B},1} = v_{\mathrm{B},2}$). Because the relative velocities of the two contacting balls at their contact interface are usually of opposite direction, large sliding friction loss occurs [63]. Since the contact deformations are in the μm-level, the transient process of ball-to-ball contact is ignored and only the quasi-steady states before and after contact are modeled.

After ball-to-ball contact stabilizes (i.e., when $v_{\mathrm{B},1} = v_{\mathrm{B},2}$), the relative velocity between the balls at the ball-to-ball contact interface measured on Ball 1 is expressed as

$$\begin{Bmatrix} \left(\Delta\mathbf{v}_{\mathrm{B2B}}\right)_x \\ \left(\Delta\mathbf{v}_{\mathrm{B2B}}\right)_y \end{Bmatrix} = \begin{Bmatrix} \left(\omega_{y,1}+\omega_{y,2}\right)R_{\mathrm{B}} \\ -\left(\omega_{x,1}+\omega_{x,2}\right)R_{\mathrm{B}} \end{Bmatrix} \tag{3.26}$$

Denoting the normal contact force in the ball-to-ball contact interface as F_{B2B} (i.e., in the global z-direction), the ball-to-ball contact frictional force in the contact interface parallel to the x-y plane is

$$\begin{Bmatrix} f_{\mathrm{B2B},x} \\ f_{\mathrm{B2B},y} \end{Bmatrix} = \begin{Bmatrix} -\left(\Delta\mathbf{v}_{\mathrm{B2B}}\right)_x \big/ \left|\Delta\mathbf{v}_{\mathrm{B2B}}\right| \cdot \mu F_{\mathrm{B2B}} \\ -\left(\Delta\mathbf{v}_{\mathrm{B2B}}\right)_y \big/ \left|\Delta\mathbf{v}_{\mathrm{B2B}}\right| \cdot \mu F_{\mathrm{B2B}} \end{Bmatrix}, \left|\Delta\mathbf{v}_{\mathrm{B2B}}\right| = \sqrt{\left(\Delta\mathbf{v}_{\mathrm{B2B}}\right)_x^2 + \left(\Delta\mathbf{v}_{\mathrm{B2B}}\right)_y^2} \tag{3.27}$$

where μ represents friction coefficient between contacting balls. The frictional loss measured in power is

$$P_{f\,\mathrm{B2B}} = \mu F_{\mathrm{B2B}} \left|\Delta\mathbf{v}_{\mathrm{B2B}}\right| \tag{3.28}$$

It can be proven that there is no relative spin at the ball-to-ball contact interface, otherwise the frictional moment about the z-axis cannot be balanced quasi-statically for each ball. Notice that the ball-to-ball contact frictional forces are parallel to the x-y plane and they should influence the ball-to-groove contact forces in theory. However, due to the small value of μ for typical linear ball bearings with metallic balls (around 0.1 according to experimental measurement in [56]), ball-to-ball contact frictional forces are at least one order of magnitude smaller than the ball-to-groove contact forces. Therefore, it is reasonable to assume that in practice ball-to-groove contact forces are not significantly affected by ball-to-ball contact friction and the calculation of ball-to-ball contact force and friction is decoupled from ball-to-groove contact forces. Based on this assumption, the new quasi-static equilibrium of Ball 1 considering ball-to-ball contact force and friction becomes

$$\sum \begin{pmatrix} \mathbf{F} \\ \mathbf{M} \end{pmatrix}_0 + \begin{bmatrix} -1 & 0 & 0 \\ 0 & 0 & -1 \\ 0 & 1 & 0 \end{bmatrix} \begin{Bmatrix} F_{\mathrm{B2B}} \\ f_{\mathrm{B2B},x} \\ f_{\mathrm{B2B},y} \end{Bmatrix} = \begin{Bmatrix} 0 \\ 0 \\ 0 \end{Bmatrix} \tag{3.29}$$

Notice the last two equations represent the equilibrium of normalized frictional moments. Similar equations hold for Ball 2, only that ball-to-ball contact force and friction are in the opposite direction.

Besides satisfying their own quasi-static equilibrium, the two balls need to satisfy ball-to-ball contact conditions: if the two balls are in contact, then they need to move in the same linear velocity at the quasi-static state; otherwise the ball-to-ball contact force is zero.

$$\begin{cases} v_{\mathrm{B},1} = v_{\mathrm{B},2}, \text{ if } v_{\mathrm{B},10} \geq v_{\mathrm{B},20} \text{ and } d_{12} \leq 2R_{\mathrm{B}} \\ F_{\mathrm{B2B}} = 0, \text{ otherwise} \end{cases} \tag{3.30}$$

Put together, Eq. (3.29) for quasi-static equilibrium of Ball 1, similar equations for Ball 2 and Eq. (3.30) for ball-to-ball contact, the motion of the two balls and ball-to-ball contact force F_{B2B} are determined iteratively. Upon solution, ball-to-ball contact friction and loss are obtained according to Eqs. (3.27) and (3.28).

Ball-to-ball contact between two balls can be generalized to multi-ball-to-ball contact as

$$\begin{cases} \text{Quasi-static equilibrium for Ball } j \text{ (similar to Eq. (3.25))} \\ \text{B2B contact between Ball } j \text{ and } j+1: \begin{cases} v_{\mathrm{B},j} = v_{\mathrm{B},(j+1)}, \text{ if } v_{\mathrm{B},j0} \geq v_{\mathrm{B},(j+1)0} \text{ and } d_{j(j+1)} \leq 2R_{\mathrm{B}} \\ F_{\mathrm{B2B},j} = 0, \text{ otherwise} \end{cases} \end{cases} \tag{3.31}$$

For N_{B} balls in contact, there are 3 kinematic variables for each of them; in addition there are ($N_{\mathrm{B}}-1$) variables for ball-to-ball contact. Accordingly, each ball needs to be in quasi-static equilibrium with 3 equations, and ($N_{\mathrm{B}}-1$) equations for ball-to-ball contact condition. In total there are $4(N_{\mathrm{B}}-1)$ variables and equations, so the multi-ball-to-ball contact problem is solvable. Again, *fsolve* function in MATLAB® is adopted to solve the problem.

3.3.3 Analytical Model of Ball-to-ball Contact

In the preceding subsection, a low order numerical model for ball-to-ball contact with iterative solution process was proposed. Wherever possible, it is desirable to have analytical models to gain more insight into the relationship between friction and the associated parameters. This subsection derives analytical formulas for linear velocity of an individual ball, ball-to-ball contact force and friction in four-point contact linear ball bearings with proper approximations.

3.3.3.1 Analysis of frictional force and moment

The frictional force $f_{i,z}$ and moment $M_{i,O}$ in each contact area are functions of c_i/a_i, an indicator for the deviation of velocity center from contact center. Extreme values of $f_{i,z}$ and $M_{i,O}$ are achieved at c_i/a_i=0 as

$$\begin{aligned} & f_{i,z}\,|_{c_i/a_i=0} = 0, \\ & M_{i,O}\,|_{c_i/a_i=0} = \frac{3}{8}\operatorname{sgn}(\omega_i)\mu F_i a_i \cdot \operatorname{Ellip}\left(\frac{\sqrt{a_i^2 - b_i^2}}{a_i}\right) \end{aligned} \tag{3.32}$$

where Ellip(·) represents the complete elliptic integral of the second kind. The case of c_i/a_i=0 represents pure spin about the contact center. The other set of extreme values are achieved when $c_i/a_i \to \pm\infty$ as

$$\begin{aligned} f_{i,z}\,|_{c_i/a_i\to\pm\infty} &= \mp \operatorname{sgn}(\omega_i)\mu F_i, \\ M_{i,O}\,|_{c_i/a_i\to\pm\infty} &= 0 \end{aligned} \tag{3.33}$$

where pure sliding happens.

The frictional force and moment in each contact area are also affected by b_i/a_i, which is the same for four contact points in a linear ball bearing and is solely determined by the conformity ratio (conf. = $R_G/2R_B$, with R_G representing the radius of the cross-sectional groove profile) of the groove [52,55]. To normalize $f_{i,z}$, it is divided by its extreme value $\operatorname{sgn}(\omega_i)\mu F_i$; while $M_{i,O}$ is normalized by dividing it by the product of $\operatorname{sgn}(\omega_i)\mu F_i$ and moment arm R_B in order to make it comparable in magnitude to $f_{i,z}$ in the equations of force and moment equilibrium. The numerical results of normalized $f_{i,z}$ and $M_{i,O}$ as functions of c_i/a_i under four typical conformity ratios of ball bearings are shown in Figure 3.11.

Observing from Figure 3.11, there is no significant difference among the plots of the four typical conformity ratios, thus they are not distinguished in the discussion. It is observed that the normalized frictional moment is very small compared to the normalized frictional force over a wide range as shown in Figure 3.11 (a). Frictional moment is only comparable to frictional force when c_i/a_i is very close to zero. When $|c_i/a_i|<0.5$, $f_{i,z}$ is almost linear with respect to c_i/a_i as shown in Figure 3.11 (b). While in the same region, the change of normalized $M_{i,O}$ is negligible compared to that of $f_{i,z}$. In fact, $|c_i/a_i|$ is usually very small in four-point contact as observed from the results presented in [55,59]. Small $|c_i/a_i|$ condition breaks down only when there is two-point contact or near two-point contact (i.e., contact forces on one diagonal pair are significantly larger than those on the other pair). Thus to simplify the analysis for four-point contact, frictional force is approximated to be linear with respect to c_i/a_i while frictional moment is approximated to always take its extreme value given in Eq. (3.32).

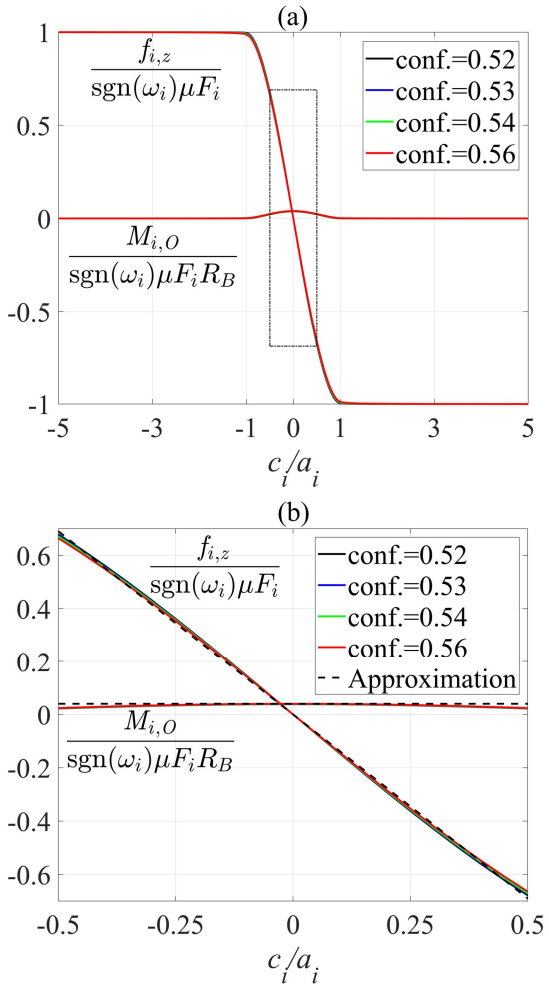

Figure 3.11: Frictional force and moment as functions of c_i/a_i: (a) full plot; (b) zoomed in plot near c_i/a_i=0

3.3.3.2 Analytical Formula for Ball Velocity

Based on the approximation of the frictional force and moment, an analytical formula for linear velocity of a single ball can be obtained. To aid the analysis, an additional variable $\Delta\eta_i$ is introduced for each contact area (see Figure 3.12 for $\Delta\eta_{\mathrm{BL}}$), indicating the angular deviation of the velocity center from the contact center in the cross section (i.e., along semi-major axis of the contact area). Thus

$$\Delta\eta_i = s_i \frac{c_i}{R_{\mathrm{B}}}, \begin{cases} s_i = 1, \text{ when } i = \mathrm{BR}, \mathrm{TL} \\ s_i = -1, \text{ when } i = \mathrm{BL}, \mathrm{TR} \end{cases} \tag{3.34}$$

Notice s_i accounts for the sign of $\Delta\eta_i$ in the definition. With the linear approximation, the frictional force becomes

$$f_{i,z} = -\mathrm{sgn}(\omega_i)\mu F_i k_f \frac{c_i}{a_i} = -\mathrm{sgn}(\omega_i)\mu F_i k_f \frac{R_\mathrm{B}}{a_i}\frac{\Delta\eta_i}{s_i} \tag{3.35}$$

Based on the plot in Figure 3.11, k_f=1.38 is picked. It is shown in Appendix G that for the linear approximation to be valid, $\Delta\eta_i$ must be a small value ($-6.25° < \Delta\eta_i < 6.25°$). The length of semi-major axis a_i is related with normal contact force F_i according to Hertzian Contact Theory [77] as

$$a_i = \Psi R_\mathrm{B}^{1/3} F_i^{1/3} \tag{3.36}$$

where Ψ is a constant determined by the geometry and material properties.

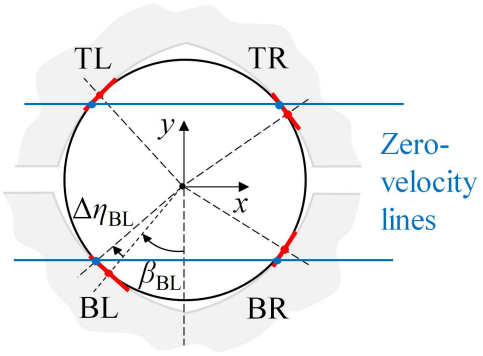

Figure 3.12: Angular deviation of velocity center from contact center

In four-point contact, it is observed that typically $\omega_{BL}>0$, $\omega_{BR}<0$, $\omega_{TR}<0$ and $\omega_{TL}>0$. Substituting the approximated frictional force and moment to the quasi-static equilibrium in Eq. (3.25), it becomes

$$\begin{bmatrix} 1 & 1 & 1 & 1 \\ -\cos\beta_{\mathrm{BL}} & -\cos\beta_{\mathrm{BR}} & \cos\beta_{\mathrm{TR}} & \cos\beta_{\mathrm{TL}} \\ \sin\beta_{\mathrm{BL}} & -\sin\beta_{\mathrm{BR}} & -\sin\beta_{\mathrm{TR}} & \sin\beta_{\mathrm{TL}} \end{bmatrix} \begin{Bmatrix} \frac{k_f}{\Psi}\mu\left(R_{\mathrm{B}}F_{\mathrm{BL}}\right)^{2/3}\Delta\eta_{\mathrm{BL}} \\ \frac{k_f}{\Psi}\mu\left(R_{\mathrm{B}}F_{\mathrm{BR}}\right)^{2/3}\Delta\eta_{\mathrm{BR}} \\ -\frac{k_f}{\Psi}\mu\left(R_{\mathrm{B}}F_{\mathrm{TR}}\right)^{2/3}\Delta\eta_{\mathrm{TR}} \\ -\frac{k_f}{\Psi}\mu\left(R_{\mathrm{B}}F_{\mathrm{TL}}\right)^{2/3}\Delta\eta_{\mathrm{TL}} \end{Bmatrix}$$
$$+\begin{bmatrix} 0 & 0 & 0 & 0 \\ \sin\beta_{\mathrm{BL}} & -\sin\beta_{\mathrm{BR}} & -\sin\beta_{\mathrm{TR}} & \sin\beta_{\mathrm{TL}} \\ \cos\beta_{\mathrm{BL}} & \cos\beta_{\mathrm{BR}} & -\cos\beta_{\mathrm{TR}} & -\cos\beta_{\mathrm{TL}} \end{bmatrix} \begin{Bmatrix} -\frac{3}{8}\Psi\mathrm{Ellip}\mu R_{\mathrm{B}}^{-2/3}F_{\mathrm{BL}}^{4/3} \\ \frac{3}{8}\Psi\mathrm{Ellip}\mu R_{\mathrm{B}}^{-2/3}F_{\mathrm{BR}}^{4/3} \\ \frac{3}{8}\Psi\mathrm{Ellip}\mu R_{\mathrm{B}}^{-2/3}F_{\mathrm{TR}}^{4/3} \\ -\frac{3}{8}\Psi\mathrm{Ellip}\mu R_{\mathrm{B}}^{-2/3}F_{\mathrm{TL}}^{4/3} \end{Bmatrix} = \begin{Bmatrix} 0 \\ 0 \\ 0 \end{Bmatrix} \tag{3.37}$$

Besides equilibrium of frictional force and moment presented in Eq. (3.37), one more relationship comes from the kinematic constraint. It was found that the two "zero-velocity lines" that pass through the zero-velocity points (i.e., velocity center c_i) on the same side of the groove (see blue lines in Figure 3.12) are parallel [60]. It still holds true in this work with $\beta_i+\Delta\eta_i$ representing the angle of zero-velocity point, which means that [60]

$$\begin{aligned} &\sin\left(\beta_{\mathrm{BL}}+\Delta\eta_{\mathrm{BL}}+\beta_{\mathrm{TL}}+\Delta\eta_{\mathrm{TL}}\right)+\sin\left(\beta_{\mathrm{BR}}+\Delta\eta_{\mathrm{BR}}-\beta_{\mathrm{TL}}-\Delta\eta_{\mathrm{TL}}\right) \\ &=\sin\left(\beta_{\mathrm{BR}}+\Delta\eta_{\mathrm{BR}}+\beta_{\mathrm{TR}}+\Delta\eta_{\mathrm{TR}}\right)+\sin\left(\beta_{\mathrm{BL}}+\Delta\eta_{\mathrm{BL}}-\beta_{\mathrm{TR}}-\Delta\eta_{\mathrm{TR}}\right) \end{aligned} \tag{3.38}$$

For contact angles β_i, there is a nominal value β_0. However, the actual contact angle deviates from β_0 due to the presence of geometric error and/or misalignment. We define

$$\Delta\beta_i=\beta_i-\beta_0 \tag{3.39}$$

where $\Delta\beta_i$ is the contact angle deviation and is usually very small (typically $-3°<\Delta\beta_i<3°$). Under the assumption of small $\Delta\beta_i+\Delta\eta_i$, (3.38) is approximated as

$$\left(\Delta\beta_{\mathrm{BL}}+\Delta\eta_{\mathrm{BL}}\right)+\left(\Delta\beta_{\mathrm{TL}}+\Delta\eta_{\mathrm{TL}}\right)-\left(\Delta\beta_{\mathrm{BR}}+\Delta\eta_{\mathrm{BR}}\right)-\left(\Delta\beta_{\mathrm{TR}}+\Delta\eta_{\mathrm{TR}}\right)=0 \tag{3.40}$$

Putting Eqs. (3.37) and (3.40) together, the angular deviation $\Delta\eta_i$ can be analytically determined. The linear velocity of the ball center is formulated as [60]

$$v_{\mathrm{B}}=\frac{\sin\left(\beta_{\mathrm{BL}}+\Delta\eta_{\mathrm{BL}}+\beta_{\mathrm{BR}}+\Delta\eta_{\mathrm{BR}}\right)v}{\sin\left(\beta_{\mathrm{BL}}+\Delta\eta_{\mathrm{BL}}+\beta_{\mathrm{BR}}+\Delta\eta_{\mathrm{BR}}\right)+\sin\left(\beta_{\mathrm{BL}}+\Delta\eta_{\mathrm{BL}}+\beta_{\mathrm{TL}}+\Delta\eta_{\mathrm{TL}}\right)+\sin\left(\beta_{\mathrm{BR}}+\Delta\eta_{\mathrm{BR}}-\beta_{\mathrm{TL}}-\Delta\eta_{\mathrm{TL}}\right)} \tag{3.41}$$

With small $\Delta\beta_i+\Delta\eta_i$ approximation, Eq. (3.41) reduces to

$$v_{\mathrm{B}}\approx\left(1+\underbrace{\left(1-\cos\left(2\beta_0\right)\right)\frac{-\Delta\beta_{\mathrm{BR}}-\Delta\eta_{\mathrm{BR}}+\Delta\beta_{\mathrm{TL}}+\Delta\eta_{\mathrm{TL}}}{2}}_{\varepsilon}\right)\frac{v}{2} \tag{3.42}$$

where ε is the deviation of ball center velocity from the nominal ball center velocity $v/2$. Substituting the solution of $\Delta\eta_i$ from Eqs. (3.37) and (3.40) into Eq. (3.42), ε is obtained as a function of four contact angle deviations $\Delta\beta_i$ and four normal contact forces F_i. The expression for ε is still cumbersome, but there is one more approximation to be made. Since the contact angle deviations $\Delta\beta_i$ are small, the contact forces on the same diagonal pair (i.e., BL and TR pair, BR and TL pair) are very close under external load in four-point contact [59]. With the approximation that $F_{\mathrm{BL}}\approx F_{\mathrm{TR}}\triangleq F_{\mathrm{U}}$ and $F_{\mathrm{BR}}\approx F_{\mathrm{TL}}\triangleq F_{\mathrm{D}}$, the ball center velocity deviation is simplified to

$$\varepsilon\approx\left(1-\cos\left(2\beta_0\right)\right)\frac{\left(-\Delta\beta_{\mathrm{BL}}+\Delta\beta_{\mathrm{TR}}\right)F_{\mathrm{U}}^{2/3}+\left(-\Delta\beta_{\mathrm{BR}}+\Delta\beta_{\mathrm{TL}}\right)F_{\mathrm{D}}^{2/3}}{2\left(F_{\mathrm{U}}^{2/3}+F_{\mathrm{D}}^{2/3}\right)} \tag{3.43}$$

This formula explicitly shows the effect of contact angle deviations and contact forces on the ball linear velocity deviation ε. A few insights from the analytical formula are: (1) ball center velocity deviation differs under different contact angle deviations and loading conditions; (2) ball linear velocity is not affected by external loading in the absence of contact angle deviations; (3) ball linear velocity is not affected by external loading under certain combinations of contact angle deviations, i.e., when $\Delta\beta_{\mathrm{BL}}=\Delta\beta_{\mathrm{TR}}$ and $\Delta\beta_{\mathrm{BR}}=\Delta\beta_{\mathrm{TL}}$.

Compared to the low order friction models described in Section 3.3.1, four major approximations are made in the analytical derivation presented above: (I) $\omega_{\mathrm{BL}}>0$, $\omega_{\mathrm{BR}}<0$, $\omega_{\mathrm{TR}}<0$ and $\omega_{\mathrm{TL}}>0$; (II) $\Delta\beta_i+\Delta\eta_i$ for each contact point is small; (III) contact forces on the same diagonal pair are approximated to be the same; (IV) contact areas are planar. Four-point contact is a necessary condition for all the four approximations. If there are only two contact points or near two-point contact (i.e., contact forces on one diagonal pair are significantly larger than those on the other pair), the angular deviation of velocity center from contact center $\Delta\eta_i$ becomes large so

that small $\Delta\beta_i+\Delta\eta_i$ assumption becomes invalid; approximations (I) and (III) also become obsolete.

3.3.3.3 Analytical Formula for Ball-to-ball Contact Force and Friction

So far, the analytical formula for ball center velocity of individual balls has been derived. According to the ball-to-ball contact model: if the two balls in Figure 3.9 with $v_{B,10}=(1+\varepsilon_1)v/2$ and $v_{B,20}=(1+\varepsilon_2)v/2$ satisfy $\varepsilon_1>\varepsilon_2$, ball-to-ball contact will happen when the distance between the two ball centers d_{12} is small enough. Ball-to-ball contact force and friction change the equilibrium of each ball. On top of $\Delta\eta_i$, assume due to ball-to-ball contact force that the additional angular contact deviation of contact center is $\Delta\zeta_i$ for each contact area. If the deviation still falls in the linear region of frictional force in Figure 3.11, the frictional force is approximated as

$$f_{i,z}=-\mathrm{sgn}(\omega_i)\mu F_i k_f \frac{R_\mathrm{B}}{a_i}\frac{\Delta\eta_i+\Delta\zeta_i}{s_i} \tag{3.44}$$

and the frictional moment is still approximated to take its maximum value given in Eq. (3.32). The new quasi-static equilibrium of Ball 1 considering ball-to-ball contact force becomes

$$\begin{bmatrix} 1 & 1 & 1 & 1 \\ -\cos\beta_{\mathrm{BL}} & -\cos\beta_{\mathrm{BR}} & \cos\beta_{\mathrm{TR}} & \cos\beta_{\mathrm{TL}} \\ \sin\beta_{\mathrm{BL}} & -\sin\beta_{\mathrm{BR}} & -\sin\beta_{\mathrm{TR}} & \sin\beta_{\mathrm{TL}} \end{bmatrix} \begin{Bmatrix} \frac{k_f}{\Psi}\mu\left(R_\mathrm{B}F_{\mathrm{BL}}\right)^{2/3}\left(\Delta\eta_{\mathrm{BL}}+\Delta\zeta_{\mathrm{BL}}\right) \\ \frac{k_f}{\Psi}\mu\left(R_\mathrm{B}F_{\mathrm{BR}}\right)^{2/3}\left(\Delta\eta_{\mathrm{BR}}+\Delta\zeta_{\mathrm{BR}}\right) \\ -\frac{k_f}{\Psi}\mu\left(R_\mathrm{B}F_{\mathrm{TR}}\right)^{2/3}\left(\Delta\eta_{\mathrm{TR}}+\Delta\zeta_{\mathrm{TR}}\right) \\ -\frac{k_f}{\Psi}\mu\left(R_\mathrm{B}F_{\mathrm{TL}}\right)^{2/3}\left(\Delta\eta_{\mathrm{TL}}+\Delta\zeta_{\mathrm{TL}}\right) \end{Bmatrix}$$
$$+\begin{bmatrix} 0 & 0 & 0 & 0 \\ \sin\beta_{\mathrm{BL}} & -\sin\beta_{\mathrm{BR}} & -\sin\beta_{\mathrm{TR}} & \sin\beta_{\mathrm{TL}} \\ \cos\beta_{\mathrm{BL}} & \cos\beta_{\mathrm{BR}} & -\cos\beta_{\mathrm{TR}} & -\cos\beta_{\mathrm{TL}} \end{bmatrix} \begin{Bmatrix} -\frac{3}{8}\Psi\mathrm{Ellip}\mu R_\mathrm{B}^{-2/3}F_{\mathrm{BL}}^{4/3} \\ \frac{3}{8}\Psi\mathrm{Ellip}\mu R_\mathrm{B}^{-2/3}F_{\mathrm{BR}}^{4/3} \\ \frac{3}{8}\Psi\mathrm{Ellip}\mu R_\mathrm{B}^{-2/3}F_{\mathrm{TR}}^{4/3} \\ -\frac{3}{8}\Psi\mathrm{Ellip}\mu R_\mathrm{B}^{-2/3}F_{\mathrm{TL}}^{4/3} \end{Bmatrix} = \begin{Bmatrix} F_{\mathrm{B2B}} \\ 0 \\ 0 \end{Bmatrix} \tag{3.45}$$

Notice here the frictional force at ball-to-ball contact interface is not included in the equations, which is a reasonable approximation because ball-to-ball frictional forces are typically at least

one order of magnitude smaller than ball-to-ball contact force. Subtracting Eq. (3.37), Eq. (3.45) becomes

$$\begin{bmatrix} 1 & 1 & 1 & 1 \\ -\cos\beta_{\mathrm{BL}} & -\cos\beta_{\mathrm{BR}} & \cos\beta_{\mathrm{TR}} & \cos\beta_{\mathrm{TL}} \\ \sin\beta_{\mathrm{BL}} & -\sin\beta_{\mathrm{BR}} & -\sin\beta_{\mathrm{TR}} & \sin\beta_{\mathrm{TL}} \end{bmatrix} \begin{Bmatrix} \frac{k_f}{\Psi}\mu\left(R_{\mathrm{B}}F_{\mathrm{BL}}\right)^{2/3}\Delta\zeta_{\mathrm{BL}} \\ \frac{k_f}{\Psi}\mu\left(R_{\mathrm{B}}F_{\mathrm{BR}}\right)^{2/3}\Delta\zeta_{\mathrm{BR}} \\ -\frac{k_f}{\Psi}\mu\left(R_{\mathrm{B}}F_{\mathrm{TR}}\right)^{2/3}\Delta\zeta_{\mathrm{TR}} \\ -\frac{k_f}{\Psi}\mu\left(R_{\mathrm{B}}F_{\mathrm{TL}}\right)^{2/3}\Delta\zeta_{\mathrm{TL}} \end{Bmatrix} = \begin{Bmatrix} F_{\mathrm{B2B}} \\ 0 \\ 0 \end{Bmatrix} \tag{3.46}$$

which relates $\Delta\zeta_i$ to ball-to-ball contact force F_{B2B}.

With the additional angular deviation $\Delta\zeta_i$, the ball still needs to satisfy kinematic constraint similar to Eq. (3.40) as

$$\left(\Delta\beta_{\mathrm{BL}}+\Delta\eta_{\mathrm{BL}}+\Delta\zeta_{\mathrm{BL}}\right)+\left(\Delta\beta_{\mathrm{TL}}+\Delta\eta_{\mathrm{TL}}+\Delta\zeta_{\mathrm{TL}}\right)-\left(\Delta\beta_{\mathrm{BR}}+\Delta\eta_{\mathrm{BR}}+\Delta\zeta_{\mathrm{BR}}\right)-\left(\Delta\beta_{\mathrm{TR}}+\Delta\eta_{\mathrm{TR}}+\Delta\zeta_{\mathrm{TR}}\right)=0 \tag{3.47}$$

Subtracting Eq. (3.40), Eq. (3.47) becomes

$$\Delta\zeta_{\mathrm{BL}}+\Delta\zeta_{\mathrm{TL}}-\Delta\zeta_{\mathrm{BR}}-\Delta\zeta_{\mathrm{TR}}=0 \tag{3.48}$$

The new velocity of the ball is expressed similar to Eq. (3.42) as

$$v_{\mathrm{B}} \approx \left(1+\underbrace{\left(1-\cos\left(2\beta_0\right)\right)\frac{-\Delta\beta_{\mathrm{BR}}-\Delta\eta_{\mathrm{BR}}+\Delta\beta_{\mathrm{TL}}+\Delta\eta_{\mathrm{TL}}}{2}}_{\varepsilon}+\underbrace{\left(1-\cos\left(2\beta_0\right)\right)\frac{-\Delta\zeta_{\mathrm{BR}}+\Delta\zeta_{\mathrm{TL}}}{2}}_{\Delta\varepsilon}\right)\frac{v}{2} \tag{3.49}$$

Let us denote the additional velocity deviation caused by ball-to-ball contact as $\Delta\varepsilon_1$ and $\Delta\varepsilon_2$ respectively. Two contacting balls need to have the same velocity at quasi-static states, thus

$$v_{\mathrm{B},1}=(1+\varepsilon_1+\Delta\varepsilon_1)v/2=v_{\mathrm{B},2}=(1+\varepsilon_2+\Delta\varepsilon_2)v/2 \text{ or } \varepsilon_1+\Delta\varepsilon_1=\varepsilon_2+\Delta\varepsilon_2 \tag{3.50}$$

Like the approximation made in last subsection, contact forces on the same diagonal pair are very close under external loading. So the following approximation is made: $F_{\mathrm{BL},1}\approx F_{\mathrm{TR},1}\triangleq F_{1\mathrm{U}}$ and $F_{\mathrm{BR},1}\approx F_{\mathrm{TL},1}\triangleq F_{1\mathrm{D}}$, $F_{\mathrm{BL},2}\approx F_{\mathrm{TR},2}\triangleq F_{2\mathrm{U}}$ and $F_{\mathrm{BR},2}\approx F_{\mathrm{TL},2}\triangleq F_{2\mathrm{D}}$ with 1 and 2 in subscript indicating Ball 1 and Ball 2 respectively. Putting together Eqs. (3.46), (3.48), (3.49) for Ball 1, the similar set of equations for Ball 2 and Eq. (3.50) for ball-to-ball contact, the ball-to-ball contact force F_{B2B} is analytically determined as

$$F_{\mathrm{B2B}}=\frac{2k_f\mu}{\Psi\left(1-\cos\left(2\beta_0\right)\right)}R_{\mathrm{B}}^{2/3}\frac{\left(F_{1\mathrm{U}}{}^{2/3}+F_{1\mathrm{D}}{}^{2/3}\right)\left(F_{2\mathrm{U}}{}^{2/3}+F_{2\mathrm{D}}{}^{2/3}\right)}{\left(F_{1\mathrm{U}}{}^{2/3}+F_{1\mathrm{D}}{}^{2/3}\right)+\left(F_{2\mathrm{U}}{}^{2/3}+F_{2\mathrm{D}}{}^{2/3}\right)}\left(\varepsilon_1-\varepsilon_2\right),\ \text{if}\ \varepsilon_1>\varepsilon_2\ \text{and}\ d_{12}\le 2R_{\mathrm{B}} \tag{3.51}$$

The analytical formula for ball-to-ball contact force shows that ball-to-ball contact force is proportional to the velocity difference between the two balls. It is also affected by the normal contact loads on the two balls, friction coefficient and constants related to Hertzian contact.

At the ball-to-ball contact interface of four-point contact linear ball bearings, the relative velocity (i.e., sliding velocity) of the two balls can be approximated as

$$\left|\Delta\mathbf{v}_{\mathrm{B2B}}\right|=\frac{v}{\cos\beta_0} \tag{3.52}$$

by assuming both balls rotate about x-axis with nominal contact angle β_0. It is observed to be a reasonable approximation in typical four-point contact linear ball bearing. As a result, the sliding friction loss measured in power in Eq. (3.28) due to ball-to-ball contact friction is explicitly expressed as

$$P_{f\mathrm{B2B}}=\mu F_{\mathrm{B2B}}\left|\Delta\mathbf{v}_{\mathrm{B2B}}\right|=\mu F_{\mathrm{B2B}}\frac{v}{\cos\beta_0} \tag{3.53}$$

3.3.4 Case Studies

3.3.4.1 Effect of Ball-to-ball on Friction

To show the effect of ball-to-ball contact on friction and compare the derived analytical formulas to the proposed low order numerical model, a case study is conducted in the setup as shown in Figure 3.13. In the setup, nominal contact angle β_0 is set to be 45°; contact angle deviation θ (<3°), induced by manufacturing error and/or misalignment, only takes place on the bottom groove (usually a long rail). External loading is represented by N_x and N_y applied to the top groove. It is assumed that the same N_y is applied to Ball 1 and Ball 2 but N_x on the two balls are of opposite direction. This kind of loading condition represents a yaw moment applied to the top groove, which accelerates ball-to-ball contact [63]. According to the definition of contact angle deviations in this work, $\Delta\beta_{\mathrm{BL}}=-\theta$, $\Delta\beta_{\mathrm{BR}}=\theta$ and $\Delta\beta_{\mathrm{TL}}=\Delta\beta_{\mathrm{TR}}=0$. Since the contact angle deviations are small, it is reasonable to approximate the four contact forces as $F_{\mathrm{BL},1}\approx F_{\mathrm{TR},1}\triangleq F_{1\mathrm{U}}=\sqrt{2}/2(N_y-N_x)$, $F_{\mathrm{BR},1}\approx F_{\mathrm{TL},1}\triangleq F_{1\mathrm{D}}=\sqrt{2}/2(N_y+N_x)$, $F_{\mathrm{BL},2}\approx F_{\mathrm{TR},2}\triangleq F_{2\mathrm{U}}=\sqrt{2}/2(N_y+N_x)$ and $F_{\mathrm{BR},2}\approx F_{\mathrm{TL},2}\triangleq F_{2\mathrm{D}}=\sqrt{2}/2(N_y-N_x)$. Define $\rho=N_x/N_y$ as the side force ratio and substitute all the

parameters into Eq. (3.43), velocity deviation of the two balls from nominal value is formulated as

$$\varepsilon_1 \approx \frac{\theta F_{1U}^{2/3} - \theta F_{1D}^{2/3}}{2\left(F_{1U}^{2/3} + F_{1D}^{2/3}\right)} = \frac{\left(1-\left(\frac{1+\rho}{1-\rho}\right)^{2/3}\right)}{\left(1+\left(\frac{1+\rho}{1-\rho}\right)^{2/3}\right)}\frac{\theta}{2},\ \varepsilon_2 \approx \frac{\theta F_{2U}^{2/3} - \theta F_{2D}^{2/3}}{2\left(F_{2U}^{2/3} + F_{2D}^{2/3}\right)} = -\frac{\left(1-\left(\frac{1+\rho}{1-\rho}\right)^{2/3}\right)}{\left(1+\left(\frac{1+\rho}{1-\rho}\right)^{2/3}\right)}\frac{\theta}{2} \tag{3.54}$$

Since the loading conditions on the two balls are centrally symmetric, the velocity deviations of the two balls are of opposite sign. Thus the velocity difference of the two balls, ε_1–ε_2, is twice the velocity deviation of a single ball.

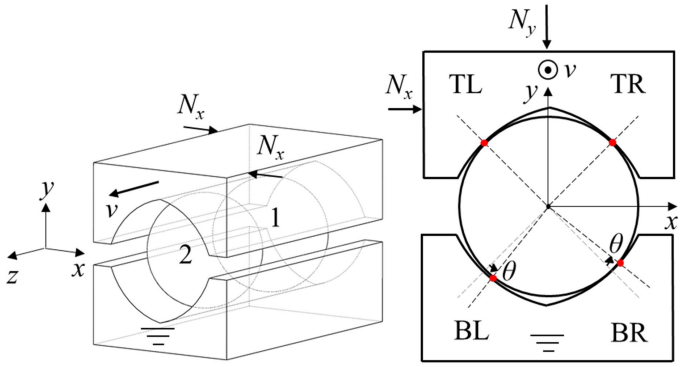

Figure 3.13: Contact angle deviations and external loading conditions in the case study

Parameters used in the case study are shown in Table 3.3.

Table 3.3: Parameters for the linear ball bearing case studies

Parameter (Symbol)	**Value [Unit]**
Ball radius (R_B)	5 [mm]
Conformity ratio of groove (conf.)	0.56
Constant related to the semi-major axis length (Ψ)	5.307×10^{-4} $[(m^2/N)^{1/3}]$
Vertical force on each ball (N_y)	100 [N]
Velocity of the top groove (v)	10 [mm/s]
Friction coefficient (μ)	0.1
Young's modulus	2.1×10^{11} $[N/m^2]$
Poisson's ratio	0.28

The velocity difference (ε_1–ε_2) of the two balls predicted by the low order numerical model as a function of θ and ρ is shown in Figure 3.14 (a). As the magnitude of the contact angle

deviation $|\theta|$ increases, the velocity difference of the two balls also increases; the same trend is observed for the side force ratio ρ. Results of $(\varepsilon_1-\varepsilon_2)$ based on the analytical formulas derived in Eq. (3.54) are shown in Figure 3.14 (b), which are observed to match closely with the proposed low order numerical model (see Figure 3.14 (a)). The difference of the low order numerical model and the analytical model only becomes noticeable when $|\rho|$ and $|\theta|$ are large. Large $|\rho|$ and $|\theta|$ are exactly where the approximations summarized at the end of Section 3.3.3.2 for the analytical formula of velocity deviation fails: four-point contact tends to be (near) two-point contact when $|\rho|$ is large, thus the small $\Delta\beta_i+\Delta\eta_i$ assumption becomes untenable, making the analytical formula inaccurate.

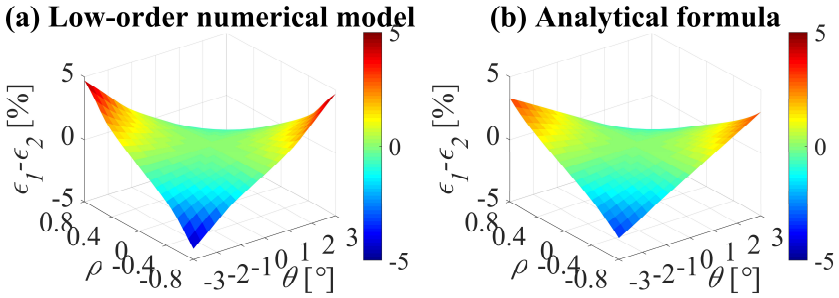

Figure 3.14: Velocity difference of two balls as functions of side force ratio and contact angle deviation

Ball-to-ball contact force and additional friction loss based on the proposed low order numerical model and the derived analytical formulas are presented in Figure 3.15. Ball-to-ball contact only happens when $\varepsilon_1-\varepsilon_2>0$; otherwise the two balls depart from each other instead of approaching and there is zero ball-to-ball contact force as shown in Figure 3.15 (a) and (b). For the non-zero contact force region, ball-to-ball contact force F_{B2B} increases with increasing $|\rho|$ and $|\theta|$; so are the total friction loss (with ball-to-ball friction loss $P_{f\mathrm{B2B}}$) versus baseline friction loss (ball-to-groove friction loss P_f). The difference between $F_{\mathrm{B2B}}/P_{f\mathrm{B2B}}$ predicted by the low order numerical model in (a)/(c) and by the analytical formula in (b)/(d) again only becomes noticeable at large $|\rho|$ and $|\theta|$ region. Since the analytical formulas in Eq. (3.51) for F_{B2B} and Eq. (3.53) for $P_{f\mathrm{B2B}}$ are both linear functions of $(\varepsilon_1-\varepsilon_2)$, the difference in $(\varepsilon_1-\varepsilon_2)$ calculation shown in Figure 3.14 carries over in the calculation of F_{B2B} and $P_{f\mathrm{B2B}}$ here. But overall, the analytical formula still predicts ball-to-ball contact force and additional friction loss very well compared to the low order numerical model. Ball-to-ball contact gives rise to significant increase of friction: the additional friction loss from ball-to-ball contact contribute to more than 185.2% increase

compared to the baseline friction (i.e., ball-to-groove contact) in the worst case scenario according to the low order numerical model as shown in Figure 3.15 (c).

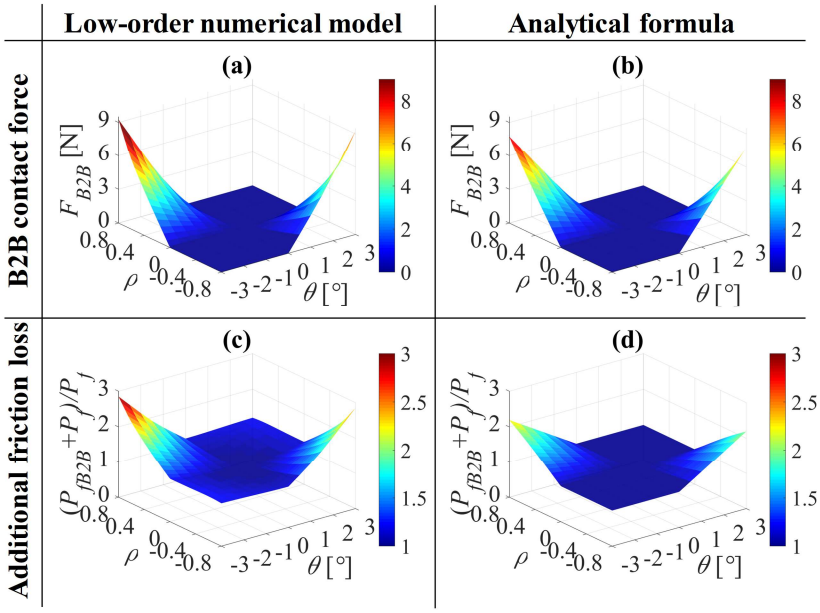

Figure 3.15: Ball-to-ball contact forces and friction loss as functions of side force ratio and contact angle deviation

3.3.4.2 Using the Analytical Model to Mitigate Ball-to-ball Contact

Ball-to-ball contact gives rise to significant friction increase as shown in last subsection. Since ball-to-ball contact develops quickly, there is significant friction variation. Thus it is desirable to avoid or at least mitigate ball-to-ball contact.

Take a particular case for example: with θ=2° and ρ=−0.6 in last subsection's setup, the two balls have different velocities summarized as Case (a) in Table 3.4. The two balls will develop ball-to-ball contact since Ball 1 is moving faster than Ball 2. Figure 3.16 (a) shows the simulated relative displacement of the two balls using the velocity calculated based on the analytical formulas in Eq. (3.54), when the initial gap between the two balls is $0.1R_B$. Insights gained from the analytical formula for velocity deviation of balls can be used to mitigate ball-to-ball contact by reducing velocity difference of balls. Given the contact angle deviations on the bottom groove (usually a long rail), if the contact angle deviations on the top groove (short and sturdy carriage) can be controlled or mated in the manufacturing or assembly processes, the velocity difference of balls can be minimized and ball-to-ball contact can be mitigated. From Eq. (3.43), it is found that if $\Delta\beta_{TR}=\Delta\beta_{BL}$ and $\Delta\beta_{TL}=\Delta\beta_{BR}$, then the velocity deviation would always

be zero irrespective of external loading. This optimized design based on the analytical formula is simulated with the results shown in Table 3.4 as Case (b) and plotted in Figure 3.16 (b), the two balls remain constant distance because of the optimized design. This highlights a benefit of the proposed analytical formula – it provides explicit relationships between variables and parameters that can be used to guide analysis and design optimization. However, as a reminder, the analytical model is only useful if the assumptions summarized in Section 3.3.3.2 are valid.

Table 3.4: Contact angle deviations and velocity deviation of balls in four-point contact linear ball bearings

	Contact angle deviations ($-\Delta\beta_{BL}=\Delta\beta_{BR}=\theta=2°$)		**Velocity deviation**		
	$\Delta\beta_{TR}$	$\Delta\beta_{TL}$		Low order numerical model	Analytical formula
Case (a)	0	0	ε_1	0.87%	0.75%
			ε_2	−0.79%	−0.75%
Case (b)	$-\theta$	θ	ε_1	0	0
			ε_2	0	0

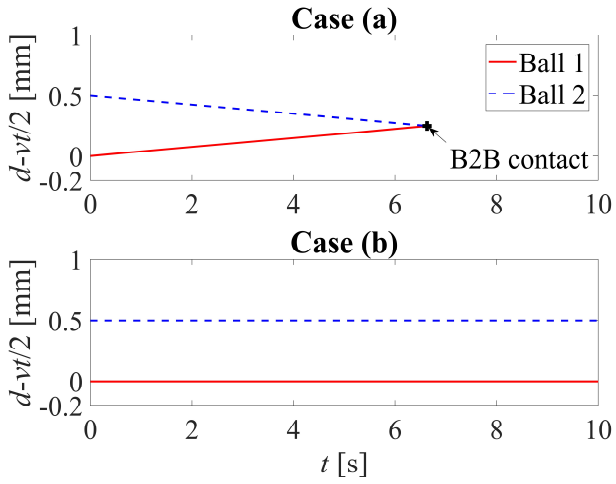

Figure 3.16: Example of ball-to-ball contact and its avoidance by optimized design

3.3.5 Validation by ANSYS FEA

In order to validate the low order numerical model and analytical model of ball-to-ball contact, and to show the validity of using the insight gained from analytical model to mitigate ball-to-ball contact, the results for Case (a) and (b) in the preceding subsection are compared to those from Finite Element Analysis (FEA) in ANSYS.

As a benchmark, dynamic simulation of ball-to-ball contact in linear ball bearing is conducted in ANSYS Workbench 16.2. The model of two balls in contact with two rails is shown in Figure 3.17 with mesh. Based on the guidelines provided by ANSYS [82], the ball surface is set as contact surface while the groove surface is set as target surface. For the ball-to-ball contact interface, Ball 1 is set as target surface while Ball 2 is set as contact surface. All the ball-to-groove and ball-to-ball contact interfaces are set as frictional contact with 0.1 friction coefficient. Augmented Lagrange contact formulations are used for the contact interfaces as recommended by ANSYS because of its robustness and flexibility [82]. All the parts are meshed with tetrahedral elements. It is common practice to make mesh refinement around the contact region while use coarse mesh elsewhere to reduce the overall number of elements. Here, a mesh refinement technique in ANSYS Workbench called body of influence is used. The fine mesh is set to be of size 0.13 mm and the coarse mesh of size 1 mm, giving the FE model 294,114 elements in total. The mesh refinement of size 0.13mm is picked after mesh sensitivity analysis. The bottom groove is fixed and the top groove is made to move at 10 mm/s. Yaw moment of 600 N·mm is applied to create the loading condition in Section 3.3.4. The two balls are placed at an initial distance of 1 μm to accelerate ball-to-ball contact such that the top rail does not move out of the mesh-refined area. A total simulation time of 0.1 second is split into 10 time steps to simulate the dynamic process from no ball-to-ball contact to the development of ball-to-ball contact and finally stabilized ball-to-ball contact. The force convergence tolerance is set to be 0.1% to balance accuracy and computational efficiency. The other settings in the finite element model are left at their default values. The solver type is also program-controlled, and it was found out that preconditioned conjugate gradient solver was adopted. Upon solution, steady-state ball-to-ball contact force is extracted from the FEA result using Reaction Force Probe.

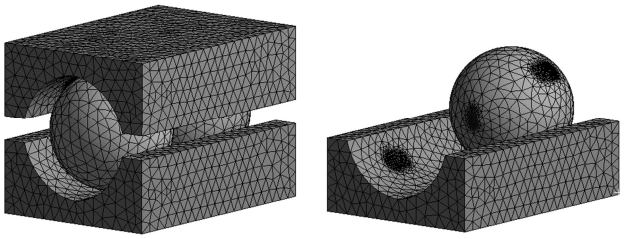

Figure 3.17: Mesh for linear ball bearing in ANSYS

The ball-to-ball contact force results are compared in Table 3.5. From the results of Case (a), it can be observed that ball-to-ball contact force predicted by the low order numerical model matches very well to that of ANSYS FEA, with only 1.26% difference. While the result based on the analytical formula shows larger error because of the approximations made in the derivation. But the error is still within 6%. For Case (b), ANSYS FEA result shows that ball-to-ball contact does not happen just as analytical formula had predicted, thus the insight gained from analytical model for ball-to-ball contact mitigation is also validated in ANSYS FEA. Given the accuracy of the proposed low order numerical model and analytical formula compared to the ANSYS FEA, it is of interest to compare their computational time. As shown in Table 3.5, the low order numerical model is three orders of magnitude faster than ANSYS FEA; while analytical formula with explicit form is another two orders of magnitude faster. The proposed low order model and analytical formula for ball-to-ball contact are therefore computationally much less expensive than the ANSYS FEA model with comparable accuracy, thus is much more desirable, e.g., for use in parametric studies and optimal design of linear ball bearings.

Table 3.5: Comparison of ball-to-ball contact forces and computational time based on the proposed models and ANSYS FEA for linear ball bearing*

		Low order numerical model	Analytical formula	ANSYS FEA
B2B Contact Force [N]	Case (a)	4.01	3.74	3.96
	Case (b)	0	0	0
Computation Time	Case (a)	0.74 sec.	6.67 msec.	5.11 hr.
	Case (b)	1.46 sec.	5.54 msec.	3.51 hr.

*All models are run on a desktop computer with Intel(R) Core(TM) i7-3770 CPU of 3.40 GHz and 16 GB RAM.

3.4 Ball-to-ball Contact Modeling for Ball Screws

In this section, ball-to-ball contact modeling for linear ball bearings presented in the preceding subsection is generalized to ball screws.

3.4.1 Ball Motion and Friction Modeling for a Single Ball in Ball Screw

Just like in linear ball bearings, modeling ball motion and friction of a single ball in ball screw is the first step towards modeling ball-to-ball contact. The same single-start, right-handed, Gothic-arch-groove-type ball screw with a single ball nut in Chapter 2 is considered. Without loss of generality, ball motion and friction modeling is presented using a two-ball module of a four-point contact ball screw as shown in Figure 3.18. The global coordinate system (CS={x, y, z}) is fixed to the screw shaft with its z-axis pointing along the axis of the screw shaft as shown in Figure 3.18 (a). Relative to CS, the inner groove of the two-ball module (representing the screw shaft) in Figure 3.18 (b), is fixed; while the outer groove representing the ball nut rotate with angular velocity ω_{N} about the z-axis and at the same time translate at velocity v_{N} along the z-axis because of the helix. According to the kinematic relationship,

$$v_{\mathrm{N}} = \bar{r}_g \omega_{\mathrm{N}}, \bar{r}_g = \frac{\bar{p}}{2\pi} \tag{3.55}$$

where $\bar{r}_{\mathrm{g}}$ is the nominal gear ratio and $\bar{p}$ represents the nominal lead of the ball screw.

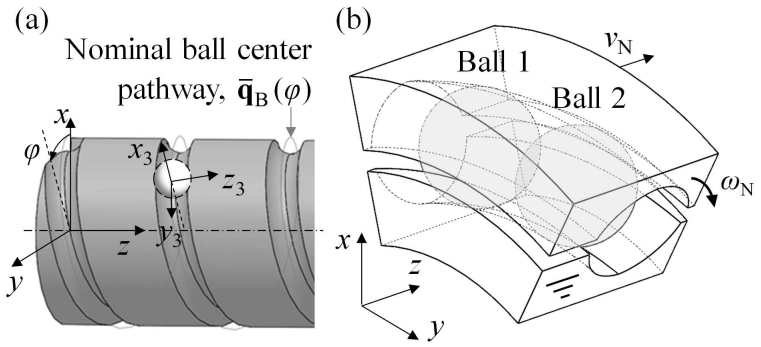

Figure 3.18: (a) Nominal ball center pathway (helix) and coordinate systems of ball screw; (b) two-ball module in ball screw

The locus of points lying on the nominal ball center pathway relative to the origin of CS is expressed as

$$\bar{\mathbf{q}}_{\mathrm{B}}(\varphi)=\begin{Bmatrix}\bar{R}_{\mathrm{P}}\cos\varphi\\ \bar{R}_{\mathrm{P}}\sin\varphi\\ \bar{r}_g\varphi\end{Bmatrix} \tag{3.56}$$

where φ is the angular distance traversed along the nominal ball center pathway starting from the x-axis to the ball location of interest on the screw (φ is referred to as azimuth angle in this work for the sake of simplicity). $\bar{R}_{\mathrm{P}}$ is the nominal pitch circle radius of the ball screw. Ignoring effects of elastic deformations and geometric errors on the grooves, the ball center velocity in the global coordinate system CS is expressed as

$$\mathbf{v}_{\mathrm{B}}(\varphi)=\begin{Bmatrix}-\bar{R}_{\mathrm{P}}\sin\varphi\omega_{\mathrm{B}}\\ \bar{R}_{\mathrm{P}}\cos\varphi\omega_{\mathrm{B}}\\ \bar{r}_g\omega_{\mathrm{B}}\end{Bmatrix} \tag{3.57}$$

where ω_{B} is the orbiting angular velocity of the ball about the ball screw axis.

A moving coordinate system $\mathrm{CS}_3=\{x_3, y_3, z_3\}$, with its origin on the nominal ball center pathway, is established such that its y_3-axis is tangent to the helical path and its x_3-axis points along the radial line from screw axis to nominal ball center as shown in Figure 3.18 (a). Figure 3.19 shows the cross-sectional profile of the ball screw in the z_3-x_3 plane. A ball, with radius R_{B}, is in four-point contact with SL, SR, NR and NL (representing Screw/Nut and Left/Right) grooves. Focusing on the SL (screw left) portion of the groove, contact angles β_{SL} are measured from $-x_3$-axis to the contact normal in the cross section. Contact coordinate system $\mathrm{CS}_{\mathrm{SL}}$ is established at the contact center such that the y_{SL}-axis is parallel to the y_3-axis and the x_{SL}-axis lies along the contact normal as shown in Figure 3.19. Similar to linear ball bearings, the contact area is assumed to be in the local z_{SL}-y_{SL} plane in this work, as shown in Figure 3.19, since the contact area is relatively small compared to the ball radius.

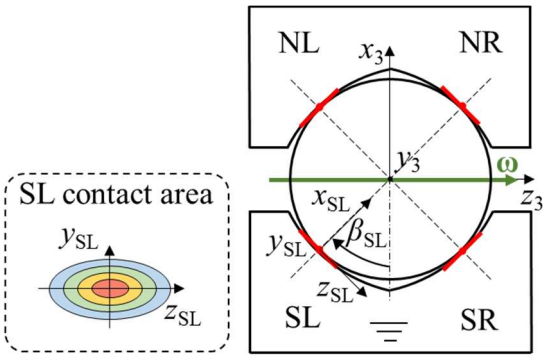

Figure 3.19: Geometry and coordinate systems for a four-point contact ball screw (highlighting the SL contact area)

Besides the gross motion, the ball also rotates about its own axis. Assume that the ball is moving at $\boldsymbol{\omega}=[\omega_x, \omega_y, \omega_z]^{\mathrm{T}}$ measured from the local coordinate system CS_3 about an axis passing through the ball center. Velocities of any point in the contact area on both ball side and groove side can be determined based on rigid body kinematics. Focusing on the SL contact area, $\mathbf{q}_{\mathrm{SL}}$ is defined as the vector from the ball center to the SL contact center, and is given in local coordinate system CS_3 as

$$\mathbf{q}_{\mathrm{SL}} = \begin{Bmatrix} -R_{\mathrm{B}} \cos\beta_{\mathrm{SL}} \\ 0 \\ -R_{\mathrm{B}} \sin\beta_{\mathrm{SL}} \end{Bmatrix} \tag{3.58}$$

For any point with local coordinates $(y_{\mathrm{SL}}, z_{\mathrm{SL}})^{\mathrm{T}}$ in the contact area, its position $\mathbf{q}_{\mathrm{SL,B}}$ in CS_3 is

$$\mathbf{q}_{\mathrm{SL,B}} = \mathbf{q}_{\mathrm{SL}} + \mathbf{T}_{\mathrm{CS_3\text{-}CS_{SL}}} \left[0, y_{\mathrm{SL}}, z_{\mathrm{SL}}\right]^{\mathrm{T}} \tag{3.59}$$

where $\mathbf{T}_{\mathrm{CS3\text{-}CS_{SL}}}$ is the transformation matrix from $\mathrm{CS}_{\mathrm{SL}}$ to CS_3 given by

$$\mathbf{T}_{\mathrm{CS_3\text{-}CS_{SL}}} = \begin{bmatrix} \cos\beta_{\mathrm{SL}} & 0 & -\sin\beta_{\mathrm{SL}} \\ 0 & 1 & 0 \\ \sin\beta_{\mathrm{SL}} & 0 & \cos\beta_{\mathrm{SL}} \end{bmatrix} \tag{3.60}$$

The velocity at the SL contact area on the ball side expressed in the global coordinate system CS is

$$\mathbf{v}_{\mathrm{SL,B}} = \mathbf{T}_{\mathrm{CS\text{-}CS_3}} \left(\boldsymbol{\omega} \times \mathbf{q}_{\mathrm{SL,B}}\right) + \dot{\mathbf{T}}_{\mathrm{CS\text{-}CS_3}} \mathbf{q}_{\mathrm{SL,B}} + \mathbf{v}_{\mathrm{B}} \tag{3.61}$$

$\mathbf{T}_{\mathrm{CS\text{-}CS_3}}$ is the transformation matrix between the global coordinate system CS and the local coordinate system CS_3 given as

$$\mathbf{T}_{\mathrm{CS\text{-}CS_3}} = \mathrm{rot}_z(\varphi) \cdot \mathrm{rot}_x(\bar{\alpha}) \tag{3.62}$$

where rot(·) represents a current-frame rotation operation about the axis specified by its subscript, as further described in Appendix A. Angle $\bar{\alpha}$ represents the nominal lead angle of the ball screw given by

$$\bar{\alpha} = \tan^{-1}\left(\frac{\bar{p}}{2\pi \bar{R}_{\mathrm{P}}}\right) \tag{3.63}$$

Since the screw is fixed, the velocity at the SL contact area on the groove side is zero. Thus the relative velocity at any point in the SL contact area is

$$\Delta\mathbf{v}_{\mathrm{SL,B}} = \mathbf{v}_{\mathrm{SL,B}} - \mathbf{0} = \mathbf{v}_{\mathrm{SL,B}} \tag{3.64}$$

The relative velocity expressed in the contact plane (i.e., z_{SL}-y_{SL}) can be formulated as

$$\begin{aligned}\left(\Delta\mathbf{v}_{\mathrm{SL,B}}\right)_{\mathrm{SL}} &= \begin{Bmatrix}\left(\Delta\mathbf{v}_{\mathrm{SL,B}}\right)_{\mathrm{SL},y}\\ \left(\Delta\mathbf{v}_{\mathrm{SL,B}}\right)_{\mathrm{SL},z}\end{Bmatrix} = \begin{bmatrix}0 & 1 & 0\\ 0 & 0 & 1\end{bmatrix}\left(\mathbf{T}_{\mathrm{CS_3\text{-}CS_{SL}}}\right)^{-1}\left(\mathbf{T}_{\mathrm{CS\text{-}CS_3}}\right)^{-1}\Delta\mathbf{v}_{\mathrm{SL,B}}\\ &= \begin{Bmatrix}\dfrac{L^2-4\pi^2 R_{\mathrm{B}}\bar{R}_{\mathrm{P}}\cos\beta_{\mathrm{SL}}}{2\pi L}\omega_{\mathrm{B}} - \left(\cos\beta_{\mathrm{SL}}\omega_z - \sin\beta_{\mathrm{SL}}\omega_x\right)R_{\mathrm{B}} - \left(\left(\dfrac{2\pi\bar{R}_{\mathrm{P}}}{L}\omega_{\mathrm{B}}+\omega_z\right)\sin\beta_{\mathrm{SL}} + \omega_x\cos\beta_{\mathrm{SL}}\right)z_{\mathrm{SL}}\\ R_{\mathrm{B}}\omega_y + \dfrac{R_{\mathrm{B}}\bar{p}}{L}\omega_{\mathrm{B}} + \left(\dfrac{2\pi\bar{R}_{\mathrm{P}}}{L}\omega_{\mathrm{B}}\sin\beta_{\mathrm{SL}} + \omega_x\cos\beta_{\mathrm{SL}} + \omega_z\sin\beta_{\mathrm{SL}}\right)y_{\mathrm{SL}}\end{Bmatrix}\end{aligned} \tag{3.65}$$

where

$$L = \sqrt{\left(2\pi\bar{R}_{\mathrm{P}}\right)^2 + \bar{p}^2} \tag{3.66}$$

Let

$$\begin{aligned}\omega_{\mathrm{SL}} &= \left(\frac{2\pi\bar{R}_{\mathrm{P}}}{L}\omega_{\mathrm{B}} + \omega_z\right)\sin\beta_{\mathrm{SL}} + \omega_x\cos\beta_{\mathrm{SL}},\\ c_{\mathrm{SL}} &= \frac{\dfrac{L^2 - 4\pi^2 R_{\mathrm{B}}\bar{R}_{\mathrm{P}}\cos\beta_{\mathrm{SL}}}{2\pi L}\omega_{\mathrm{B}} - \left(\cos\beta_{\mathrm{SL}}\omega_z - \sin\beta_{\mathrm{SL}}\omega_x\right)R_{\mathrm{B}}}{\omega_{\mathrm{SL}}},\\ d_{\mathrm{SL}} &= -\frac{R_{\mathrm{B}}\omega_y + \dfrac{R_{\mathrm{B}}\bar{p}}{L}\omega_{\mathrm{B}}}{\omega_{\mathrm{SL}}}\end{aligned} \tag{3.67}$$

The relative velocity field in Eq. (3.65(3.65) is rewritten as

$$\begin{Bmatrix}\left(\Delta\mathbf{v}_{\mathrm{SL,B}}\right)_{\mathrm{SL},y}\\ \left(\Delta\mathbf{v}_{\mathrm{SL,B}}\right)_{\mathrm{SL},z}\end{Bmatrix} = \begin{Bmatrix}\omega_{\mathrm{SL}}\left(c_{\mathrm{SL}} - z_{\mathrm{SL}}\right)\\ \omega_{\mathrm{SL}}\left(-d_{\mathrm{SL}} + y_{\mathrm{SL}}\right)\end{Bmatrix} \tag{3.68}$$

Following the same procedure, the velocity field for other contact areas is derived (see Appendix F for details). It is observed that the relative velocity field in the elliptical contact area is a circular contour centered at (c_i, d_i) as shown in Figure 3.8 (b), with $i \in$ {SL, SR, NR, NL} representing different contact areas. Notice that the center of the contour represents the zero-velocity point.

With the velocity field expressed over the contact area, friction can be calculated given normal contact stress distribution similar to that in linear ball bearings. The frictional force $f_{i,y}$ along y_i-axis and $f_{i,z}$ along z_i-axis, frictional moment $M_{i,O}$ about contact center, and friction loss are calculated by double integrating the frictional stress over the contact area. Comparing the relative velocity field of ball screw in Figure 3.8 to that of rotary and linear ball bearing in Figure 3.8 (b), the major difference is that the helix of ball screw introduces relative rotation between the screw and nut about the y_3-axis. Thus there are frictional forces in z_{SL}-direction, which lie in the cross-sectional plane, making frictional forces (from a given contact surface) and normal contact forces (from other contact surfaces) coupled for individual balls in ball screw. As a result, friction and contact load distribution for individual balls need to be calculated together in ball screw. A low order static load distribution model for ball screw is presented in Chapter 3. Here it is augmented to include friction.

Since the frictional forces are small compared to the normal contact forces, it is assumed that the bulk elastic deformation of the ball screw shaft (i.e., $\mathbf{U}_{\mathrm{S}}$ in Eq. (2.23)) calculated in the static load distribution model is not affected.

For individual balls, the friction calculation is conducted together with load distribution. Neglecting gyroscopic effect, each ball needs to be in quasi-static equilibrium under normal load, frictional force and moment as

$$
\sum\begin{pmatrix}\mathbf{F}\\ \mathbf{M}\end{pmatrix}_0 =
\begin{bmatrix}
\cos\beta_{\mathrm{SL}} & \cos\beta_{\mathrm{SR}} & -\cos\beta_{\mathrm{NR}} & -\cos\beta_{\mathrm{NL}}\\
0 & 0 & 0 & 0\\
\sin\beta_{\mathrm{SL}} & -\sin\beta_{\mathrm{SR}} & -\sin\beta_{\mathrm{NR}} & \sin\beta_{\mathrm{NL}}\\
0 & 0 & 0 & 0\\
0 & 0 & 0 & 0\\
0 & 0 & 0 & 0
\end{bmatrix}
\begin{Bmatrix}F_{\mathrm{SL}}\\ F_{\mathrm{SR}}\\ F_{\mathrm{NR}}\\ F_{\mathrm{NL}}\end{Bmatrix}
$$

$$
+\begin{bmatrix}
0 & 0 & 0 & 0\\
1 & 1 & 1 & 1\\
0 & 0 & 0 & 0\\
R_{\mathrm{B}}\sin\beta_{\mathrm{SL}} & -R_{\mathrm{B}}\sin\beta_{\mathrm{SR}} & -R_{\mathrm{B}}\sin\beta_{\mathrm{NR}} & R_{\mathrm{B}}\sin\beta_{\mathrm{NL}}\\
0 & 0 & 0 & 0\\
-R_{\mathrm{B}}\cos\beta_{\mathrm{SL}} & -R_{\mathrm{B}}\cos\beta_{\mathrm{SR}} & R_{\mathrm{B}}\cos\beta_{\mathrm{NR}} & R_{\mathrm{B}}\cos\beta_{\mathrm{NL}}
\end{bmatrix}
\begin{Bmatrix}
\mathrm{Sig}(\omega_{\mathrm{SL}}/\Delta\omega)f_{\mathrm{SL},y}\\
\mathrm{Sig}(\omega_{\mathrm{SR}}/\Delta\omega)f_{\mathrm{SR},y}\\
\mathrm{Sig}(\omega_{\mathrm{NR}}/\Delta\omega)f_{\mathrm{NR},y}\\
\mathrm{Sig}(\omega_{\mathrm{NL}}/\Delta\omega)f_{\mathrm{NL},y}
\end{Bmatrix}
$$

$$
+\begin{bmatrix}
-\sin\beta_{\mathrm{SL}} & \sin\beta_{\mathrm{SR}} & \sin\beta_{\mathrm{NR}} & \sin\beta_{\mathrm{NL}}\\
0 & 0 & 0 & 0\\
\cos\beta_{\mathrm{SL}} & \cos\beta_{\mathrm{SR}} & -\cos\beta_{\mathrm{NR}} & -\cos\beta_{\mathrm{NL}}\\
0 & 0 & 0 & 0\\
R_{\mathrm{B}} & R_{\mathrm{B}} & R_{\mathrm{B}} & R_{\mathrm{B}}\\
0 & 0 & 0 & 0
\end{bmatrix}
\begin{Bmatrix}
\mathrm{Sig}(\omega_{\mathrm{SL}}/\Delta\omega_{\mathrm{BS}})f_{\mathrm{SL},z}\\
\mathrm{Sig}(\omega_{\mathrm{SR}}/\Delta\omega_{\mathrm{BS}})f_{\mathrm{SR},z}\\
\mathrm{Sig}(\omega_{\mathrm{NR}}/\Delta\omega_{\mathrm{BS}})f_{\mathrm{NR},z}\\
\mathrm{Sig}(\omega_{\mathrm{NL}}/\Delta\omega_{\mathrm{BS}})f_{\mathrm{NL},z}
\end{Bmatrix}
$$

$$
+\begin{bmatrix}
0 & 0 & 0 & 0\\
0 & 0 & 0 & 0\\
0 & 0 & 0 & 0\\
\cos\beta_{\mathrm{SL}} & \cos\beta_{\mathrm{SR}} & -\cos\beta_{\mathrm{NR}} & -\cos\beta_{\mathrm{NL}}\\
0 & 0 & 0 & 0\\
\sin\beta_{\mathrm{SL}} & -\sin\beta_{\mathrm{SR}} & -\sin\beta_{\mathrm{NR}} & \sin\beta_{\mathrm{NL}}
\end{bmatrix}
\begin{Bmatrix}
\mathrm{Sig}(\omega_{\mathrm{SL}}/\Delta\omega_{\mathrm{BS}})M_{\mathrm{SL},O}\\
\mathrm{Sig}(\omega_{\mathrm{SR}}/\Delta\omega_{\mathrm{BS}})M_{\mathrm{SR},O}\\
\mathrm{Sig}(\omega_{\mathrm{NR}}/\Delta\omega_{\mathrm{BS}})M_{\mathrm{NR},O}\\
\mathrm{Sig}(\omega_{\mathrm{NL}}/\Delta\omega_{\mathrm{BS}})M_{\mathrm{NL},O}
\end{Bmatrix}
=\begin{Bmatrix}0\\0\\0\\0\\0\\0\end{Bmatrix}
\tag{3.69}
$$

where modified logistic Sigmoid function defined in (3.20) is used to deal with the potential stick region in two-point contact. Here

$$
\Delta\omega_{\mathrm{BS}} = \frac{2\pi\bar{R}_{\mathrm{P}}}{L}\omega_{\mathrm{N}}\sin\bar{\beta} \tag{3.70}
$$

is the approximated relative spin velocity in the same diagonal contact pair (i.e., $|\omega_{\mathrm{SL}}-\omega_{\mathrm{NR}}|$ or $|\omega_{\mathrm{SR}}-\omega_{\mathrm{NL}}|$).

Together with the contact conditions presented in Chapter 2, a new state vector $\mathbf{x}_i' = [\mathbf{p}_{3\mathrm{B}i}^{\mathrm{T}}, \gamma_{\mathrm{SL}i},\gamma_{\mathrm{SR}i},\gamma_{\mathrm{NL}i},\gamma_{\mathrm{NR}i},\omega_{\mathrm{B}i},\omega_{xi},\omega_{yi},\omega_{zi}]_{10\times1}^{\mathrm{T}}$ is defined for each ball with subscript i indicating the i^{th} ball. The function $\mathbf{\Phi}_i'(\mathbf{x}_i')$ containing conditions for quasi-static equilibrium of the ball is formulated as

$$\boldsymbol{\Phi}_i^{'}(\mathbf{x}_i^{'}) = \begin{Bmatrix} \begin{Bmatrix} (\hat{\mathbf{n}}_{\mathrm{SL}i} \cdot \mathbf{t}_{\mathrm{SL}i})_{1\times 1} \\ \vdots \end{Bmatrix}_{4\times 1} \\ \sum \begin{Bmatrix} \mathbf{F} \\ \mathbf{M} \end{Bmatrix}_{0\ 6\times 1} \end{Bmatrix}_{10\times 1} = \mathbf{0} \tag{3.71}$$

The same conditions hold for all the balls. The new state vector $\mathbf{x}_i^{'}$ can be solved in an iterative process using the *fsolve* function in MATLAB®.

3.4.2 Low Order Numerical Model of Ball-to-ball Contact for Ball Screws

The orbiting angular velocities of individual balls in ball screw differ depending on contact angles and loading conditions. Similar to linear ball bearing, ball-to-ball contact develops when the orbiting angular velocity of the ball behind is faster than the ball in front ($\omega_{\mathrm{B},10} > \omega_{\mathrm{B},20}$) and when the angular distance between the two balls $\Delta\varphi_{12}$ is close enough ($\Delta\varphi_{12} = \varphi_{\mathrm{B},1} - \varphi_{\mathrm{B},2} \leq 2\beta_{\mathrm{B2B}}$); β_{B2B} is ball-to-ball contact angle as shown in Figure 3.20 and is defined as

$$\beta_{\mathrm{B2B}} = \sin^{-1}\left(\frac{2\pi R_{\mathrm{B}}}{L}\right) \tag{3.72}$$

Notice that the radius for ball-to-ball contact in Figure 3.20 is not the pitch circle radius R_{P}, but L defined in Eq. (3.66) with the lead of the ball screw factored in.

At the ball-to-ball contact interface between Ball 1 and Ball 2, another coordinate system CS_4 is established: z_4-x_4 plane is where ball-to-ball contact happens. Similar to the linear ball bearing case, the relative velocity at the ball-to-ball contact interface measured on Ball 1 is expressed as

$$\begin{Bmatrix} (\Delta\mathbf{v}_{\mathrm{B2B}})_{z_4} \\ (\Delta\mathbf{v}_{\mathrm{BL}})_{x_4} \end{Bmatrix} = \begin{Bmatrix} (\omega_{x,1} + \omega_{x,2}) R_{\mathrm{B}} \cos\beta_{\mathrm{B2B}} + (\omega_{y,1} - \omega_{y,2}) R_{\mathrm{B}} \sin\beta_{\mathrm{B2B}} \\ -(\omega_{z,1} + \omega_{z,2}) R_{\mathrm{B}} \end{Bmatrix} \tag{3.73}$$

Denoting the normal contact force at the ball-to-ball contact interface as F_{B2B} (i.e., in y_4-direction), the ball-to-ball contact frictional force in the contact interface (z_4-x_4 plane) is

$$\begin{Bmatrix} f_{\mathrm{B2B},z_4} \\ f_{\mathrm{B2B},x_4} \end{Bmatrix} = \begin{Bmatrix} -(\Delta\mathbf{v}_{\mathrm{B2B}})_{z_4} / |\Delta\mathbf{v}_{\mathrm{B2B}}| \cdot \mu F_{\mathrm{B2B}} \\ -(\Delta\mathbf{v}_{\mathrm{B2B}})_{x_4} / |\Delta\mathbf{v}_{\mathrm{B2B}}| \cdot \mu F_{\mathrm{B2B}} \end{Bmatrix}, |\Delta\mathbf{v}_{\mathrm{B2B}}| = \sqrt{(\Delta\mathbf{v}_{\mathrm{B2B}})_{z_4}^2 + (\Delta\mathbf{v}_{\mathrm{B2B}})_{x_4}^2} \tag{3.74}$$

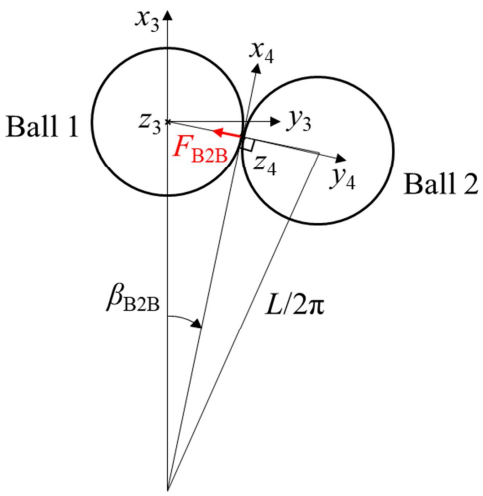

Figure 3.20: Ball-to-ball contact between two balls in ball screw

Under ball-to-ball contact, Ball 1 needs to be in quasi-static equilibrium with the addition of ball-to-ball contact force and friction to Eq. (3.69) as

$$\sum \begin{pmatrix} \mathbf{F} \\ \mathbf{M} \end{pmatrix}_0 + \begin{bmatrix} \sin\beta_{B2B} & 0 & \cos\beta_{B2B} \\ -\cos\beta_{B2B} & 0 & \sin\beta_{B2B} \\ 0 & 1 & 0 \\ 0 & R_B\cos\beta_{B2B} & 0 \\ 0 & R_B\sin\beta_{B2B} & 0 \\ 0 & 0 & -R_B \end{bmatrix} \begin{Bmatrix} F_{B2B} \\ f_{B2B,z_4} \\ f_{B2B,x_4} \end{Bmatrix} = \begin{Bmatrix} 0 \\ 0 \\ 0 \\ 0 \\ 0 \\ 0 \end{Bmatrix} \tag{3.75}$$

Similar equations hold for Ball 2, only that ball-to-ball contact force and friction are in the opposite direction.

Besides satisfying their own quasi-static equilibrium, the two balls need to satisfy ball-to-ball contact conditions: if the two balls are in contact, then they need to move at the same orbiting angular velocity at quasi-static states; otherwise the ball-to-ball contact force is 0.

$$\begin{cases} \omega_{B,1} = \omega_{B,2}, \text{ if } \omega_{B,10} \geq \omega_{B,20} \text{ and } \Delta\varphi_{12} = \varphi_1 - \varphi_2 \leq 2\beta_{B2B} \\ F_{B2B} = 0, \text{ otherwise} \end{cases} \tag{3.76}$$

Put together Eq. (3.75) for quasi-static equilibrium of Ball 1, similar equations for Ball 2 and Eq. (3.76) for ball-to-ball contact, the motion of two balls and ball-to-ball contact force (if there is any) are determined. Upon solution, ball-to-ball contact friction and loss are calculated accordingly.

Similar to that in linear ball bearings, ball-to-ball contact between two balls in ball screws can be generalized to multi-ball-to-ball contact as

$$\begin{cases} \text{Quasi-static equilibrium for Ball } j \\ \text{B2B contact between Ball } j \text{ and } j+1: \begin{cases} \omega_{\mathrm{B},j}=\omega_{\mathrm{B},(j+1)}, \text{ if } \omega_{\mathrm{B},j0}\geq\omega_{\mathrm{B},(j+1)0} \text{ and } \varphi_j-\varphi_{j+1}\leq 2\beta_{\mathrm{B2B}} \\ F_{\mathrm{B2B},j}=0, \text{otherwise} \end{cases} \end{cases} \quad (3.77)$$

3.4.3 FEA Validation of Ball-to-ball Contact Model

To validate the low order numerical model of ball-to-ball contact for ball screws, the results are compared to those from ANSYS FEA in the same ball-to-ball contact module between two balls as shown in Figure 3.18. The reasons for validation in two-ball module instead of the whole ball screw are: (1) ball-to-ball contact modeling is the main focus of this work, thus validation of ball-to-ball contact is the priority; (2) the dynamic simulation of a full ball screw with enough accuracy using FEA is computationally too demanding.

Parameters for ball screw used in this validation study are shown in Table 3.6. The geometry and material properties are similar to those in Section 2.4. The groove profile on the screw side has contact angle deviation θ as shown in Figure 3.21. Two cases are simulated to demonstrate the effect of different contact angle deviation: θ=0° is set for Ball 1 in both cases; for Ball 2, θ=2° is set in case (a) and θ=3° is used in case (b). This kind of contact angle deviation induces different orbiting angular velocities of balls and results in ball-to-ball contact in both case (a) and (b).

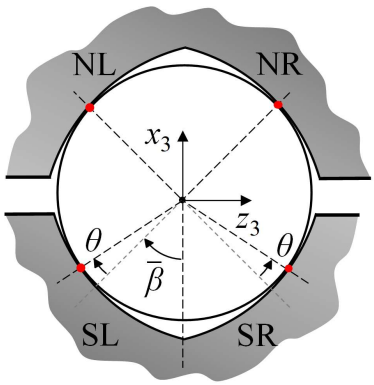

Figure 3.21: Contact angle deviation at the cross section of ball screw grooves

Table 3.6: Parameters for ball-to-ball contact simulation in ball screw

Parameter (Symbol)	Value [Unit]
Ball radius (R_{B})	2.778 [mm]
Conformity ratio of groove (conf.)	0.56
Pitch radius of ball screw (R_{P})	16.5 [mm]

Lead of ball screw (p)	20 [mm]
Nominal contact angle (β_0)	45 [°]
Angular velocity of the nut (ω_N)	2π [rad/s]
Friction coefficient (μ)	0.1
Young's modulus	210 [N/mm^2]
Poisson's ratio	0.28

As a benchmark, dynamic simulation of ball-to-ball contact in ball screw is conducted in ANSYS Workbench 16.2. The CAD model of the two-ball module for case (a) is shown in Figure 3.22, which are meshed with tetrahedral elements of size 0.05 mm around the contact area and 1 mm elsewhere, giving the FE model 230,816 elements in total. Mesh refinement of size 0.05 mm is picked after mesh sensitivity analysis. Similarly, the FEA model of case (b) has 231,931 elements. The ball nut is made to rotate about the ball screw axis at ω_N. The screw shaft is constrained by frictionless support to only translate along axial direction with external force 50 N in both cases. The two balls are placed at an initial distance of 1 μm apart to accelerate ball-to-ball contact. A total simulation time of 0.005 second is split into 10 time steps to simulate the dynamic process from no ball-to-ball contact to the development of ball-to-ball contact and finally stabilized ball-to-ball contact under quasi static equilibrium. The other important settings in ANSYS FEA are kept the same as in the linear ball bearing case in Section 3.3.5. The contact problem is solved using the same desktop computer as used for the linear ball bearing case study.

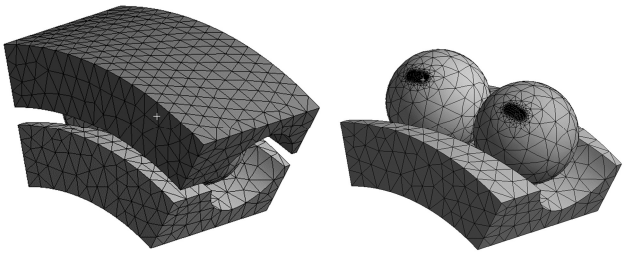

Figure 3.22: Mesh for ball screw in ANSYS

The ball-to-ball contact forces from the low order numerical model and ANSYS FEA are compared in Table 3.7. It is observed that ball-to-ball contact forces predicted by the low order numerical model are reasonably close to those from ANSYS FEA, with 6.67% and 6.64% difference for case (a) and (b) respectively. As shown in the comparison of computational time in Table 3.7, the low order numerical model is three orders of magnitude faster than ANSYS FEA,

indicating the computational efficiency of the proposed low order model once again. For case (a), the friction increase caused by ball-to-ball contact is 39.2% relative to that before ball-to-ball contact, according to the low order numerical model; while 60.2% friction increase is observed for case (b). Both results indicate the significance of ball-to-ball contact to the friction increase of ball screw.

Table 3.7: Comparison of ball-to-ball contact forces and computational time based on low order numerical model and ANSYS FEA for ball screw

		Low order numerical model	ANSYS FEA
Case (a)	B2B Contact force [N]	1.92	1.80
	Computational time	15.3 sec.	5.75 hr.
Case (b)	B2B Contact force [N]	2.89	2.71
	Computational time	14.7 sec.	5.35 hr.

3.4.4 Simulation of a Whole Ball Screw with Ball-to-ball Contact

Since the proposed low order numerical model of ball-to-ball contact in ball screw has been validated, it can be incorporated in the whole ball screw friction model to simulate the friction behavior of the whole ball screw. A ball screw with the same parameters as shown in Table 3.6 is used in the simulation. The ball screw is 800 mm long with the nut initially placed in the middle. A total time of 2s in 200 steps are simulated. The nut is confined to only rotate, while screw shaft is only allowed to translate in the axial direction at the two ends. Axial load of 1500 N is applied to the screw shaft on one end, and 37 balls in two loaded turns yields 97.8% occupation ratio of the active ball track. Recirculation of balls is modeled by connecting the start and end of the return tube. The same type of contact angle deviation in Figure 3.21 is adopted; the magnitude of contact angle deviation θ on the screw side is set to be sinusoidal with respect to azimuth angle as shown in Figure 3.23.

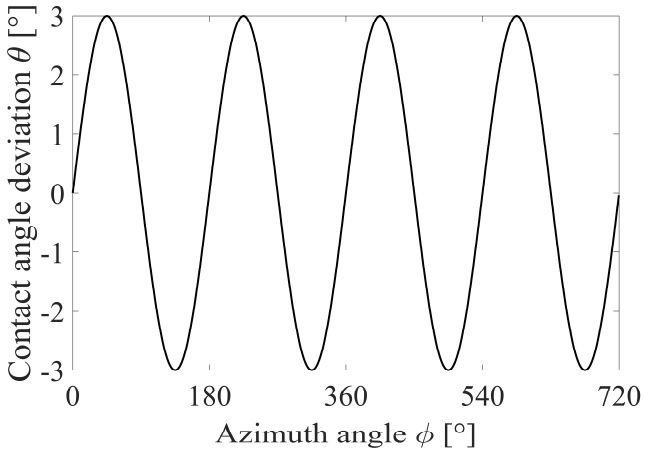

Figure 3.23: Contact angle deviation with respect to azimuth angle

The balls are evenly distributed at the start of the simulation. However, due to the sinusoidal contact angle deviation, the orbiting angular velocities of the balls differ, making the distance between balls to change over time. Figure 3.24 shows the angular distance between balls with respect to the nut rotation angle (i.e., which is proportional to time); balls in ball-to-ball contact are marked as black dots. Four groups of ball-to-ball contact form because of the velocity difference induced by the four cycles of contact angle deviations in Figure 3.23.

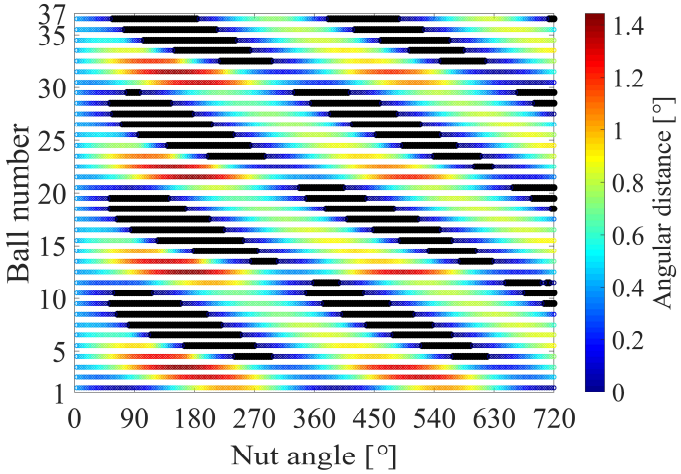

Figure 3.24: Angular distance between balls and ball-to-ball contact status (ball-to-ball contact is marked using black dots)

Figure 3.25 shows the total friction torque and the contribution of ball-to-groove and ball-to-ball contact. It is observed that ball-to-groove contact friction barely has variation in this case study, while ball-to-ball contact contributes to a maximum of 49.6% additional friction torque at 126° nut rotation angle. As the contacted balls gradually disengage, the friction torque contributed by ball-to-ball contact decreases and reaches its minimum value zero at 306° nut

rotation angle when there is no ball-to-ball contact. After that, ball-to-ball contact builds up again and gradually stabilizes. Thus ball-to-ball contact not only gives rise to significant friction increase, but also significant friction variation due to the engagement and disengagement of ball-to-ball contact.

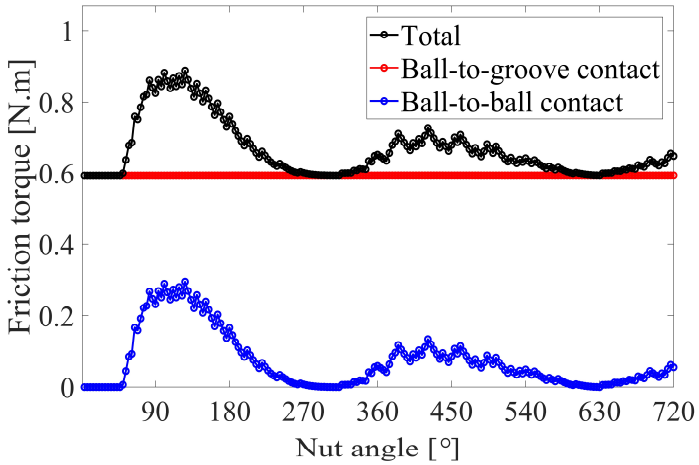

Figure 3.25: Total friction torque and the contribution of ball-to-groove and ball-to-ball contact

3.5 Summary

In this chapter, two sources of friction variation in ball bearings and ball screws related to rolling, sliding and spin of balls at the contact interface are discussed and modeled. A sensitivity analysis of friction to rolling, sliding and spin in a ball from four-point contact ball bearing is first conducted. To do this, the ball-to-groove contact friction of rotary ball bearing is modeled following a well-established procedure but with a simplifying assumption of planar contact area. In a case study, sliding and spin in four-point contact operation is shown to result in more than 10 times larger friction than two-point contact which mainly has rolling.

The sliding friction at ball-to-ball contact interface is another source of friction increase and variation, particularly in linear ball bearings and ball screws which typically do not use caged balls. In this chapter, low order velocity difference driven ball-to-ball contact models at steady state are proposed for both linear ball bearings and ball screws. Based on the friction analysis and relevant approximations, analytical formulas for velocity deviation of balls and ball-to-ball contact friction are derived for four-point contact linear ball bearing. Compared to ball-to-ball friction predictions from FEA models developed in ANSYS, the proposed numerical models are shown in case studies to be accurate within 7%, while computing at least three orders of magnitude faster. Using the insights gained from the analytical model, ball-to-ball contact is

shown to be mitigated by reducing the velocity difference of balls in four-point contact linear ball bearings. Significant friction increase and variation due to ball-to-ball contact are demonstrated in a case study of ball screw, highlighting the importance of modeling ball-to-ball contact. However, the velocity-difference driven ball-to-ball contact models presented in this chapter have limitations. They only model the steady state conditions of the ball-to-ball contact, the transient process of ball-to-ball contact is not captured.

Chapter 4 Application of the Developed Load Distribution and Friction Models to Rack EPAS

4.1 Overview

Four-point contact ball bearing and ball screw are the two key mechanical components in rack EPAS gear. They are subjected to large multi-directional load and manufacturing errors in EPAS, making it hard to accurately calculate their load distribution for the purpose of sizing. The EPAS gear also suffers from "stick-slip" problem (i.e., sticky feel sensed by the driver) mainly due to the friction variation of ball bearing and ball screw.

This chapter applies the developed load distribution model for ball screw (presented in Chapter 2), friction model for four-point contact ball bearing and ball-to-ball contact model for ball screw (presented in Chapter 3) to rack EPAS in a few realistic scenarios. Important insights for ball bearing and ball screw design, inspection and manufacturing tolerance specification are derived based on the developed models.

The chapter is organized as follows: two applications of the developed load distribution model are presented in Section 4.2. The robustness of two stiffness tests for ball screw are compared. Then the developed models are applied to the sizing of ball bearing and ball screw in rack EPAS under different tie rod angles. Section 4.3 presents the applications of the developed friction models to ball bearing and ball screw in rack EPAS. The friction variation of four-point contact ball bearing and double-row angular contact ball bearing are compared. Finally, the effect of different ball screw manufacturing errors on ball-to-ball contact are demonstrated. Section 4.4 provides a summary of the chapter.

4.2 Applications of the Developed Load Distribution Model to Rack EPAS

4.2.1 Lash Tests of Ball Screw

Lash tests are important to characterize the stiffness of ball screws where they usually serve as the end of line check for stiffness. There are two types of lash tests: axial lash test and

conical lash test whose setups are shown in Figure 4.1 (a) and (b) respectively. In both tests, the ball nuts are fixed. In axial lash test, axial force F_{axial} ranging from −200 to 200 N is applied to one end of the screw shaft which is constrained from rotating and the axial displacement is measured in the case of Figure 4.1 (a) at the end of the screw shaft. While in conical lash test, lateral force $F_{lateral}$ is applied from a certain distance to the ball nut and lateral displacement is measured.

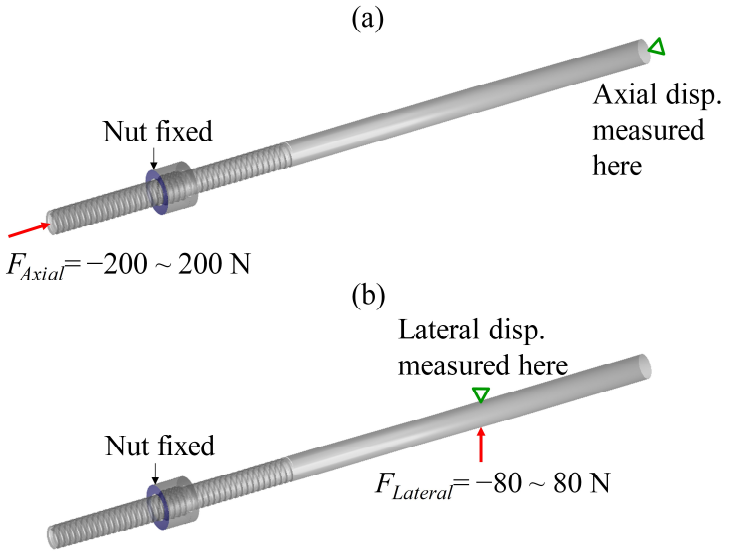

Figure 4.1: Setup for (a) axial lash test; (b) conical lash test

Based on the proposed static low order load distribution model for ball screw, the load distribution and elastic deformation of the ball screw under external loads can be calculated, thus stiffness curves can be generated for both axial and conical lash tests. To compare the robustness of the two lash tests, the only variable here is the location of balls inside the active ball track. Four patterns of ball distribution are studied as shown in Figure 4.2. The parameters for ball screw used in the case study are shown in Table 4.1. They are chosen to be close to the actual parameters in rack EPAS.

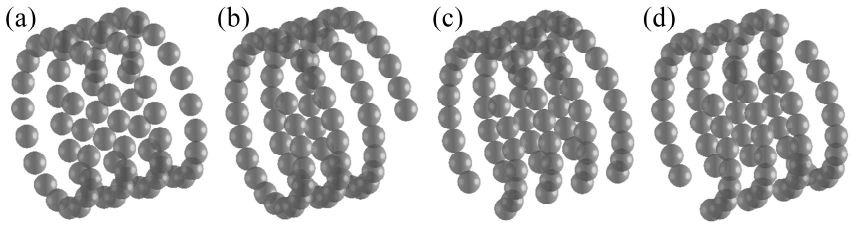

Figure 4.2: Patterns of ball locations: (a) evenly distributed; (b) stacked on one end; (c) stacked on one side; (d) half-half

Table 4.1: Parameters of ball screw in lash tests

Parameter (Symbol)	Value [Unit]
Length of screw shaft	750 [mm]
Location of the nut	154 [mm]
Nominal pitch circle radius ($\bar{R}_p$)	14.5 [mm]
Nominal pitch ($\bar{p}$)	7 [mm]
Nominal contact angle ($\bar{\beta}$)	45 [°]
Nominal ball radius ($\bar{r}_B$)	2 [mm]
Nominal radius of curvature of groove ($\bar{r}_G$)	2.16 [mm]
Number of loaded balls (N_B)	71
Number of rounds of balls	3.75
Young's modulus (E_S=E_N=E_B)	2.1×10^{11} [N/m^2]
Poisson's ratio (v_S=v_N=v_B)	0.28

The simulated stiffness curves of axial and conical lash tests are shown in Figure 4.3 (a) and (b) respectively. Observe that axial lash curves with the four different ball distribution patterns show more consistency than conical lash curves: there is only 3.72% difference in the axial lash curves; while there is 14.7% difference in the conical lash curves. The reason is that the load distribution under bending moment (in conical lash test) is more sensitive to the location of balls. Based on the results of the proposed load distribution model, axial lash test shows better robustness to ball locations than conical lash test given the same gauge repeatability and reproducibility (gauge R&R).

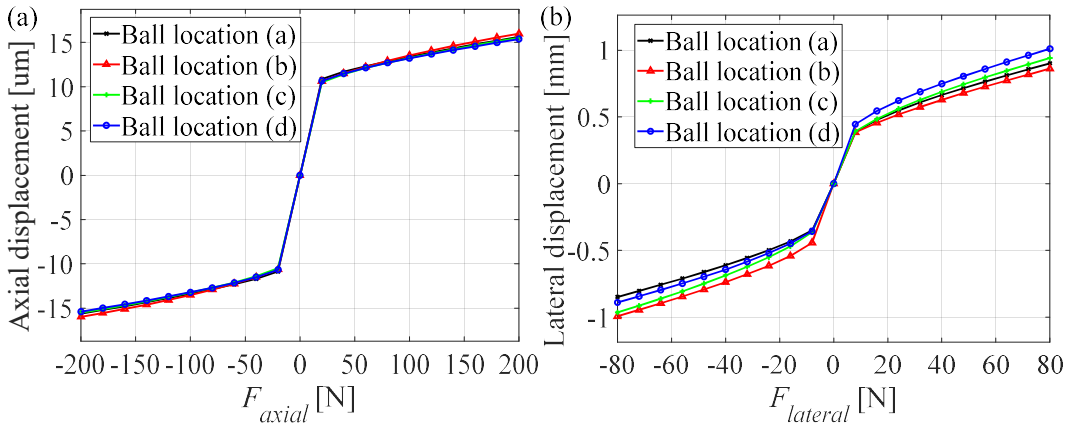

Figure 4.3: (a) Axial lash curves; (b) conical lash curves with four different ball locations

4.2.2 Sizing of Bearing and Ball Screw in EPAS

The developed static load distribution model for ball screw can be applied to ball bearing by treating ball bearing as ball screw with zero lead. Thus the developed load distribution models can be used for the sizing of bearing and ball screw in EPAS. In the simulation, the loading and boundary conditions are set to mimic the operating conditions of EPAS as shown in Figure 4.4: the outer ring of the four-point contact (4P) ball bearing is fixed, while the rack at the rack/pinion location is only allowed to translate; external force with magnitude $F/2$ is applied to both ends of the rack at the tie rod angle, θ, measured from the axis of the screw shaft.

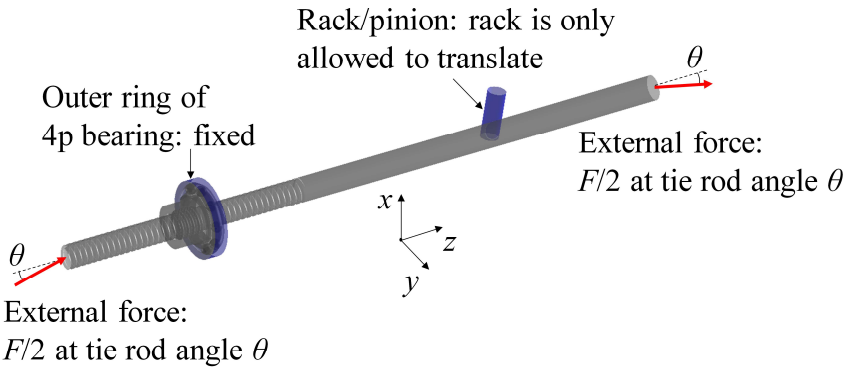

Figure 4.4: Loading and boundary conditions for rack EPAS

The load distribution on the 4P bearing and ball screw under four different tie rod angles are shown in Figure 4.5 when rack load F = 14500 N is applied. When tie rod angle is 0°, the contact loads are almost even in the 4P bearing as shown in Figure 4.5 (a). The contact loads in ball screw show variations due to the coupling effect of deformation discussed in Section 2.4.1.1, but they are almost evenly distributed. The tie rod angle introduces bending moment to the 4P bearing and ball screw, so the compressed sides of the bearing and ball screw have higher contact loads as shown in Figure 4.5 (a), (b) and the visualization in Figure 4.5 (c). With increasing tie rod angle, the maximum load on the balls also increases. At 18° tie rod angle, the maximum load on the 4P bearing is 1.47 times of the maximum load with 0° tie rod angle; while the ratio for ball screw is 3.32. If 4P bearing and ball screw are sized with 0° tie rod angle, their strength under large tie rod angle is undermined. The proposed static load distribution model is thus useful for sizing ball bearing and ball screw in EPAS.

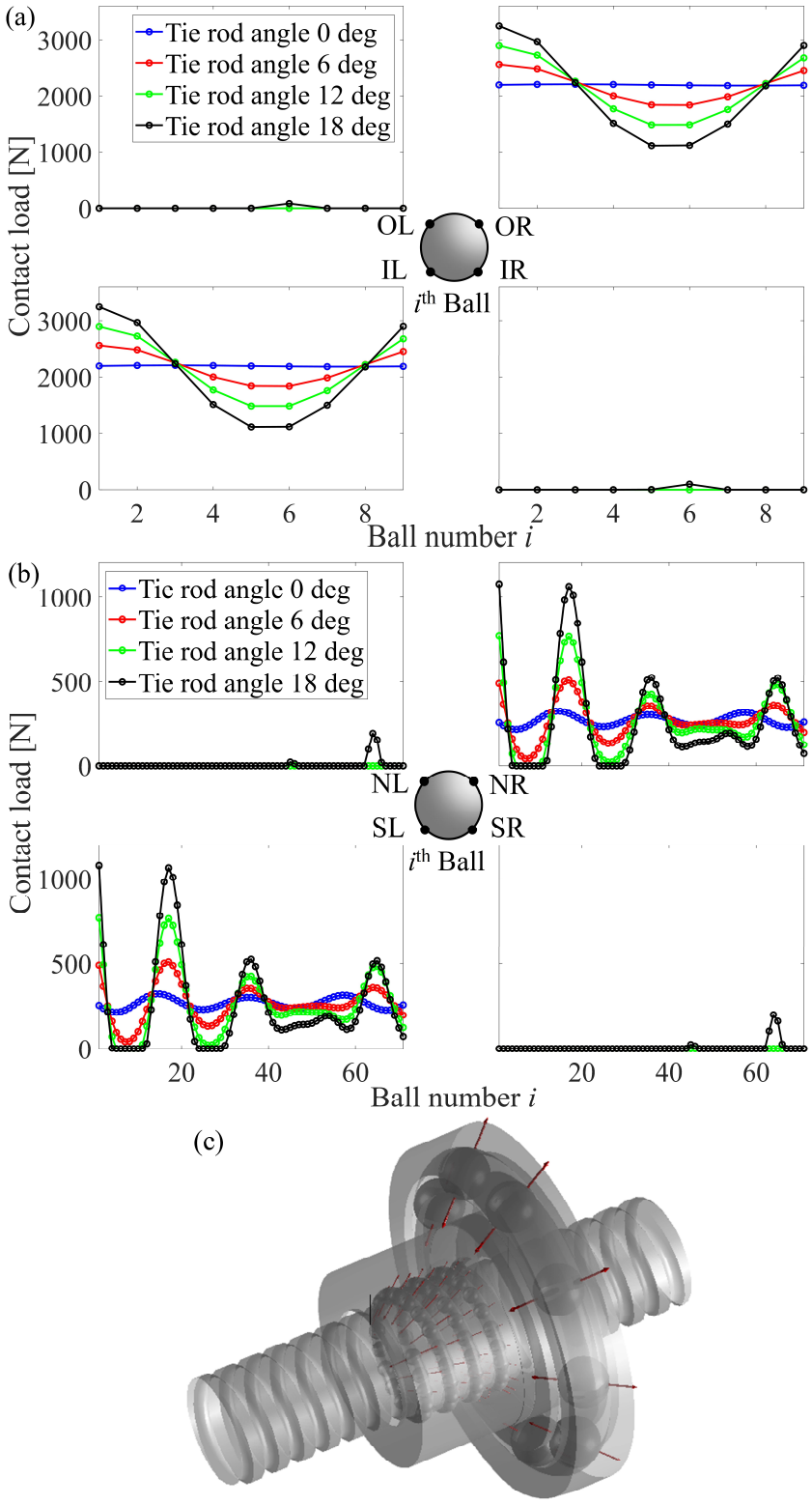

Figure 4.5: Load distribution on balls under different tie rod angles: (a) four-point contact ball bearing; (b) ball screw; (c) visualization of the 18° tie rod angle case (arrows represent contact forces)

4.3 Applications of the Developed Friction Models to Rack EPAS

Friction is another important characteristic for EPAS gear. “Stick-slip” is an extreme case of friction variation and is targeted to mainly come from the two key mechanical components: four-point contact ball bearing and ball screw. In this subsection, two sources of friction variation are examined based on the friction models presented in Chapter 3: transition of rolling, sliding and spin in four-point contact ball bearing; ball-to-ball contact in ball screw. Important insights for design and manufacturing tolerance specification are derived.

4.3.1 Four-point Contact Ball Bearing vs. Double-row Angular Contact Ball Bearing

Four-point contact ball bearings (4P bearing) are adopted in rack EPAS because of its capability of taking multi-directional loads in a compact configuration. However, the 4P bearings in rack EPAS usually comes with undersized balls to reduce the overall friction. Thus the balls are expected to operate with two-point contact like angular contact ball bearings. However, depending on the external load, the balls can also develop four-point contact as shown in Figure 4.6 (a). The transition between two-point contact and four-point contact in 4P bearing can induce significant friction variation as evidenced by the sensitivity analysis of friction to rolling, sliding and spin in a single ball from 4P bearing, discussed in Section 3.2. As an alternative, if double row angular contact ball bearing (DR bearing) is used, each ball is confined to move with two-point contact only by design as shown in Figure 4.6 (b).

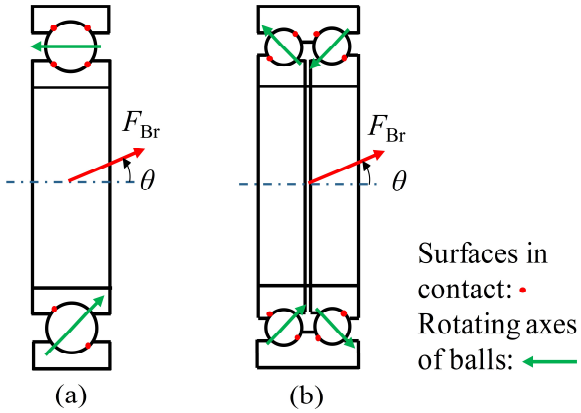

Figure 4.6: (a) Four-point contact bearing; (b) double row angular contact bearing

To compare the friction torque of 4P bearing and DR bearing, a case study is conducted with parameters presented in Table 4.2. These parameters are chosen to be close to the actual ones in rack EPAS. External force F_{Br}=3000N at various angles θ is applied to the inner ring of both ball bearings as shown in Figure 4.6. The outer ring of the bearings are fixed while the inner

ring of the bearings are set to rotate at 10 revolutions per second. The friction torque of both bearings is shown in Figure 4.7. As the external load changes direction with θ, the 4P bearing shows larger frictional variation due to the transition between four-point and two-point contact of some balls. In this case study, the maximum friction torque of the 4P bearing is 5.69 times the minimum even under the same magnitude of external force. While DR bearing has consistent friction torque under varying external load direction because there is always two-point contact. From the friction variation point of view, DR bearing is better than 4P bearing in rack EPAS application.

Table 4.2: Parameters of four-point (4P) contact ball bearings and double row (DR) ball bearings

	Parameter (Symbol)	**Value [Unit]**
Shared	Pitch circle diameter	70 [mm]
	Outer ring diameter	90 [mm]
	Inner ring diameter	50 [mm]
	Contact angle	45 [°]
	Young's modulus (E_S=E_N=E_B)	210 [N/mm^2]
	Poisson's ratio (ν_S=ν_N=ν_B)	0.28
4P Bearing	Ball radius ($\bar{r}_B$)	6.25 [mm]
	Radius of curvature of groove ($\bar{r}_G$)	6.75 [mm]
	Thickness of ball bearing	16 [mm]
	Number of balls	9
DR Bearing	Ball radius ($\bar{r}_B$)	4 [mm]
	Radius of curvature of groove ($\bar{r}_G$)	4.32 [mm]
	Thickness of ball bearing	24 [mm]
	Number of balls	9×2

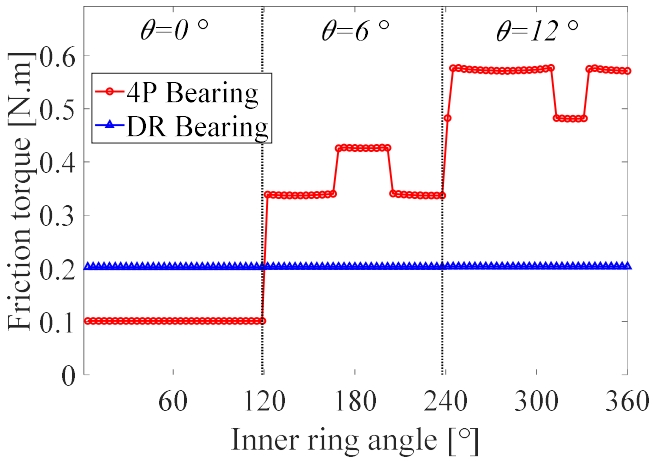

Figure 4.7: Comparison of the friction torque from 4P bearing and DR bearing under changing external load direction

4.3.2 Effect of Different Manufacturing Errors on Ball-to-ball Contact

Geometric errors are common in ball screw especially in the slender screw shaft (see Figure 4.8 (a)) due to manufacturing errors. The proposed model can be used to analyze different types of geometric errors and their effects on ball-to-ball contact. The first type of common geometric errors in the screw shaft of ball screw is pitch error as shown in Figure 4.8 (b), where the actual ball center pathway deviates from the nominal one (see Figure 4.8 (a)) in z-direction. Assume sinusoidal pitch error with magnitude e_p occurs one cycle per revolution, the SL groove surface is described as

$$\mathbf{S}_{\mathrm{SL}}(\varphi,\gamma)=\mathrm{rot}_z(\varphi)\cdot\mathrm{rot}_x(\bar{\alpha})\cdot\begin{Bmatrix}-\bar{r}_{\mathrm{G}}\cos\gamma+\left(\bar{r}_{\mathrm{G}}-\bar{r}_{\mathrm{B}}\right)\cos\bar{\beta}\\0\\-\bar{r}_{\mathrm{G}}\sin\gamma+\left(\bar{r}_{\mathrm{G}}-\bar{r}_{\mathrm{B}}\right)\sin\bar{\beta}\end{Bmatrix}+\begin{Bmatrix}\bar{R}_P\cos\varphi\\\bar{R}_P\sin\varphi\\\dfrac{\bar{p}}{2\pi}\varphi+e_p\sin\varphi\end{Bmatrix} \tag{4.1}$$

The equivalent error of the SL groove surface at the contact point along the nominal contact normal direction is calculated as

$$e_{\mathrm{eqv,SL}}(\varphi)=\cos\bar{\alpha}\sin\bar{\beta}\cdot e_p\sin\varphi \tag{4.2}$$

which can be measured by Coordinate Measurement Machine (CMM) in practice.

The second common type of geometric errors is roundness error as shown in Figure 4.8 (c); the actual ball center pathway deviates from the nominal one in both x- and y-direction. The oval shape of the groove with roundness error in Figure 4.8 (c) indicates that roundness error

shows a pattern of two cycles per revolution. Assume the roundness error is sinusoidal with magnitude e_R, the groove surface is described as

$$\mathbf{S}_{SL}(\varphi,\gamma)=\mathrm{rot}_z(\varphi)\cdot\mathrm{rot}_x(\bar{\alpha})\cdot\begin{Bmatrix}-\bar{r}_G\cos\gamma+(\bar{r}_G-\bar{r}_B)\cos\bar{\beta}\\0\\-\bar{r}_G\sin\gamma+(\bar{r}_G-\bar{r}_B)\sin\bar{\beta}\end{Bmatrix}+\begin{Bmatrix}(\bar{R}_P+e_R\sin 2\varphi)\cos\varphi\\(\bar{R}_P+e_R\sin 2\varphi)\sin\varphi\\\dfrac{\bar{p}}{2\pi}\varphi\end{Bmatrix} \tag{4.3}$$

The equivalent error at the contact point (measured by CMM) along the nominal contact normal direction is

$$e_{eqv,SL}(\varphi)=\cos\bar{\beta}\cdot e_R\sin 2\varphi \tag{4.4}$$

The equivalent errors of sinusoidal pitch error in Eq. (4.2) with e_p = 5 μm are plotted in Figure 4.9 (a). Similarly, the equivalent errors of sinusoidal roundness error in Eq. (4.4) with e_R = 5 μm is plotted in Figure 4.9 (b). It is obvious that different geometric errors have different patterns.

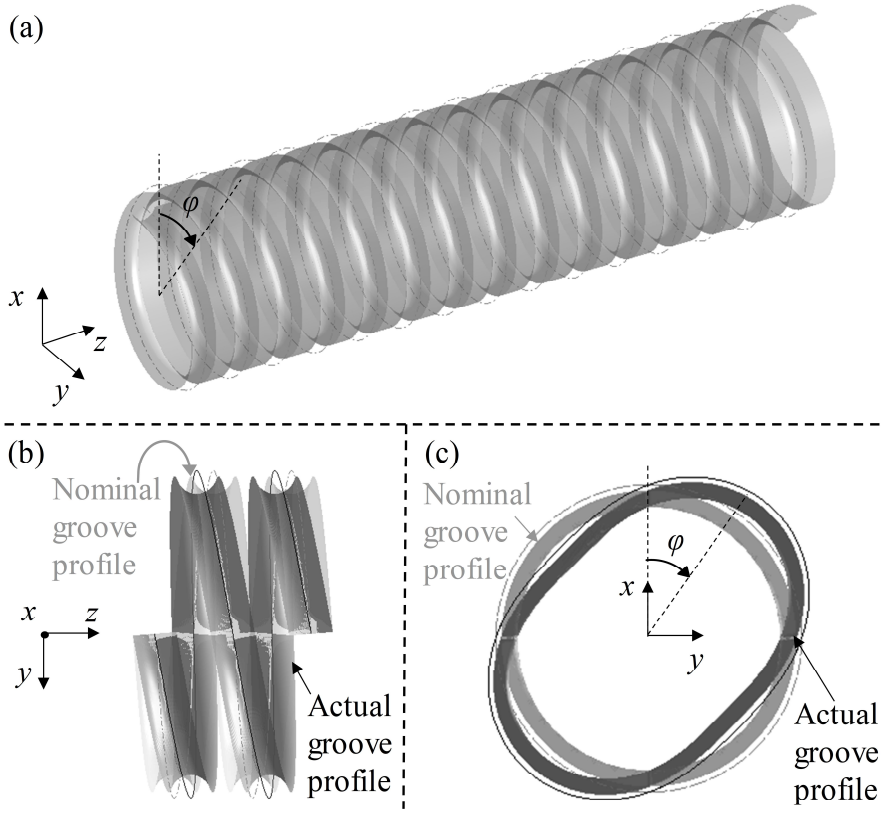

Figure 4.8: (a) Nominal groove profile; (b) demonstration of pitch error (exaggerated); (b) demonstration of roundness error (exaggerated)

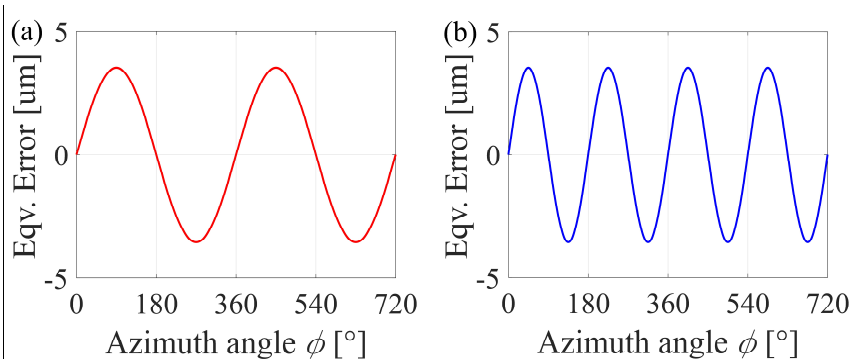

Figure 4.9: Equivalent errors for: (a) pitch error with e_p =5μm; (b) roundness error with e_R =5μm

Since ball nut is sturdy, it is less susceptible to manufacturing errors compared to ball screw. It is assumed that ball nut does not have any geometric error in this case study. With the same boundary condition in Figure 4.10 (a) and axial force F_{axial} = 1000 N, the load distribution in the ball screw with the described pitch error and roundness error are shown in Figure 4.10 (a), and visualized in (b) and (c) respectively. It is worth noticing that due to the applied axial load, the balls are in two-point contact at SL and NR contact points. The two types of manufacturing errors show very different effect on load distribution. The load distribution in balls with roundness error is less uniform than that with pitch error. From Figure 4.10 (c), it can be observed that some balls lose contact with the groove, which corresponds to the pattern of roundness error in Figure 4.9 (c).

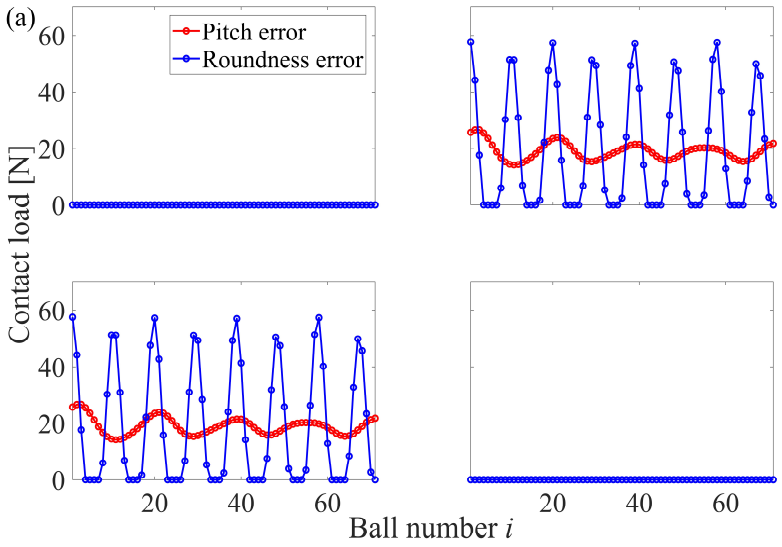

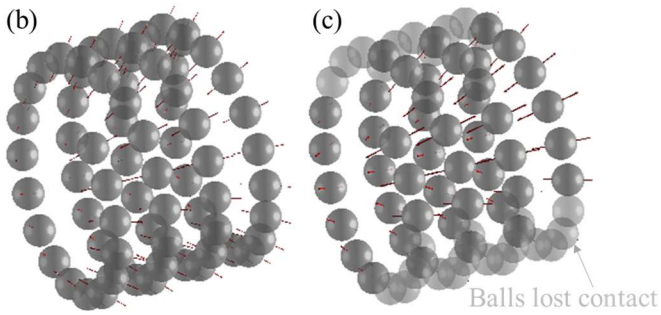

Figure 4.10: (a) Comparison of contact load distribution; (b) visualization of load distribution with pitch error; (c) visualization of load distribution with roundness error

As a result of the load distribution pattern, pitch error and roundness error have different effect on ball-to-ball contact. It is obvious that ball screw with roundness error develops ball-to-ball contact quicker if the balls lost contact are assumed to not move or move at a lower velocity than the nominal velocity, which makes the BNA in rack EPAS gear to have higher possibility of developing "stick-slip".

Due to the cost limit, manufacturing errors of ball screw cannot be eliminated. But based on the insights derived from the developed models, roundness error with two cycles per revolution pattern needs to have tighter tolerance than pitch error with one cycle per revolution pattern.

4.4 Summary

In this chapter, the developed low order load distribution and friction models for ball bearing and ball screw are applied to various case studies related to rack EPAS. Using the load distribution model, it is found that axial lash test for ball screw stiffness inspection is more robust (i.e., shows less variation under the same gauge R&R) than conical lash test. The maximum contact loads on ball bearing and ball screw under non-zero tie rod angle are also shown to be much larger than those with 0° tie rod angle, indicating that sizing of ball bearing and ball screw must be done carefully to ensure the strength of both parts. Thus the developed static load distribution model is proven to be a good analytical design verification tool for sizing the ball bearing and ball screw in rack EPAS.

In terms of friction, the four-point contact ball bearing shows much larger friction variation than double row angular contact ball bearing under changing external load direction, indicating that double row angular contact ball bearing is better for rack EPAS application from

friction variation point of view. Ball-to-ball contact in ball screw gives rise to significant friction increase and variation, thus it is always desirable to mitigate ball-to-ball contact from happening. It is found out that, under the same magnitude of manufacturing errors, balls are more likely to lose contact with groove under roundness error on ball screw than pitch error, causing the ball screw to have higher chance of developing ball-to-ball contact and “stick-slip”.

The developed models not only provide useful tools for sizing the ball bearing and ball screw in rack EPAS, but also provide important insights for the inspection, optimal design and manufacturing tolerance specification of ball bearings and ball screws in rack EPAS.

Chapter 5 Conclusion and Future Work

5.1 Conclusions

In this dissertation, low order models of load distribution and friction for ball bearings and ball screws are proposed. Load distribution and friction variation under the effect of multi-directional loading and manufacturing errors are the main topics of focus.

In Chapter 2, a low order static load distribution model for ball screw is proposed incorporating geometric errors and elastic deformations. A new and comprehensive way of describing the ball screw groove surfaces with geometric errors using multivariate functions is proposed. A ball-to-groove contact model based on Hertzian Contact Theory including geometric errors is developed. Low order finite element method (FEM) is adopted to incorporate axial, torsional and lateral elastic deformations of the ball screw into the contact model. Benchmarked against high order finite element analysis (FEA) model created in ANSYS Workbench 16.2, the proposed model is shown in simulation studies to be accurate in predicting load distribution in a ball screw with and without geometric error. However, an existing low order model, which considers only axial deformation but not lateral deformation effects, exhibits significant errors in predicting load distribution, even when only axial loads are applied to the ball screw. Moreover, compared to the ANSYS model, the proposed model is shown to be over 6800 times faster, while providing versatility in describing and analyzing different types of geometric errors. It is therefore more convenient for use in parametric studies and design optimization of ball screws.

In Chapter 3, two sources of contact-related friction variation in ball bearings and ball screws are investigated and modeled. A sensitivity analysis of friction to rolling, sliding and spin in a ball from four-point contact ball bearing is first conducted. To do this, the ball-to-groove contact friction of rotary ball bearing is modeled following a well-established procedure but with planar contact area assumption. In a case study, sliding and spin in four-point contact operation is shown to result in much higher friction than two-point contact which mainly has rolling. Ball-to-ball contact is another source of friction variation. In this work, low order numerical models for ball-to-ball contact friction in linear ball bearings and ball screws are proposed. Furthermore,

an analytical model for ball-to-ball contact friction in four-point contact linear ball bearing is derived by making simplifications to its low-order numerical model. Compared to ball-to-ball friction predictions from FEA models developed in ANSYS, the proposed numerical models are shown in case studies to be accurate within 7% difference, while computing at least three orders of magnitude faster. Using the insights gained from the analytical model, ball-to-ball contact is shown to be mitigated by reducing the velocity difference of balls in four-point contact linear ball bearings. Significant friction increase and variation due to ball-to-ball contact are demonstrated in a case study of ball screw, highlighting the importance of modeling ball-to-ball contact. However, the velocity-difference driven ball-to-ball contact models presented in this work do have limitations: they only model the steady state conditions of the ball-to-ball contact, the transient process of ball-to-ball contact is not captured.

The developed load distribution and friction models are then applied to rack EPAS gear in a few realistic scenarios in Chapter 4. Important insights are gained, e.g., axial lash test is more robust to ball locations than conical lash test as stiffness inspection of ball screws; double row angular contact ball bearings show much less friction variation than four-point contact ball bearings because they are constrained to always have two-point contact operation; manufacturing errors with two cycles per revolution pattern (e.g., roundness error) are more likely to cause balls to lose contact with grooves than pitch error with one cycle per revolution pattern, causing the ball screw to have higher chance of developing ball-to-ball contact and "stick-slip". The developed models not only provide useful tools for rack EPAS sizing and analysis, but could also provide important insights for inspection, optimal design and manufacturing tolerance specification of ball bearings and ball screws in rack EPAS.

The work presented in this dissertation has be published in several journal and conference articles. The low order load distribution model has been published in [70,84]. The proposed ball-to-ball contact friction models have been published in [71–73]. The application of the developed load distribution and friction models to rack EPAS gear is published in [74].

5.2 Future Work

Although the proposed static load distribution models for ball screw, ball-to-ball contact models of linear ball bearing and ball screws are validated against ANSYS FEA, it is desirable to have experimental validations for them. Measurement of contact forces is hard due to sensing

difficulties, however, the insight gained from the static load distribution model: axial lash test is more robust to ball locations than conical lash test as stiffness inspection of ball screws, can be experimentally tested. Experiments can be carried out to validate the other two important insights derived from friction modeling: (1) double row angular contact ball bearing shows much less friction variation than four-point contact ball bearing; (2) manufacturing errors with two cycles per revolution pattern (e.g., roundness error) are more likely to cause balls to lose contact with grooves than pitch error of the same magnitude, causing the ball screw to have higher chance of developing ball-to-ball contact and "stick-slip".

The developed friction models can be expanded to include more factors, e.g., transient process of ball-to-ball contact, realistic stick region treatment, lubricant, thermal effects. The developed friction models can be extended to include dynamic (i.e., centrifugal and gyroscopic) effect for high-speed applications of ball bearings and ball screws.

As a versatile tool, the developed models can be applied to aid the analysis and design optimization of ball bearing and ball screw in rack EPAS. The static load distribution model can be utilized to conduct fatigue analysis of rack EPAS; design optimization of parameters can be conducted to minimize number of balls losing contact while ensuring the strength of the ball bearing and ball screw in rack EPAS.

Appendices

Appendix A: Current Frame Rotation Matrix

The current frame rotation operator $\mathrm{rot}_{x/y/z}(\theta)$ performs a rotation of angle θ around $x/y/z$-axis. Their elements are given as

$$\mathrm{rot}_x(\theta)=\begin{bmatrix}1 & 0 & 0\\ 0 & \cos\theta & -\sin\theta\\ 0 & \sin\theta & \cos\theta\end{bmatrix},\mathrm{rot}_y(\theta)=\begin{bmatrix}\cos\theta & 0 & -\sin\theta\\ 0 & 1 & 0\\ -\sin\theta & 0 & \cos\theta\end{bmatrix},\mathrm{rot}_z(\theta)=\begin{bmatrix}\cos\theta & -\sin\theta & 0\\ \sin\theta & \cos\theta & 0\\ 0 & 0 & 1\end{bmatrix}$$

Appendix B: Hertzian Contact Theory

Hertzian Contact Theory enables the calculation of contact deformation, area and stress in the vicinity of the contact region [77]. Without loss of generality, Hertzian Contact Theory is explained here with respect to the SL ball-to-groove contact interface, but the procedure can be generalized to other contact interfaces as well. The Hertzian constant, $C_{\mathrm{SL}i}$, occurring in Eq. (2.14), is given by the general expression in Eq. (4.31) in [77] as

$$C_{\mathrm{SL}i} = F_1(e_{\mathrm{SL}i})\left(\frac{9}{16E_{\mathrm{S,eq}}^2\rho_{\mathrm{SL}i,\mathrm{eq}}}\right)^{\frac{1}{3}} \tag{B.1}$$

where $\rho_{\mathrm{SL}i,\mathrm{eq}}$ denotes the equivalent radius of curvature at the SL contact point of ball i, given by

$$\rho_{\mathrm{SL}i,\mathrm{eq}} = \sqrt{R'_{\mathrm{SL}i} \cdot R''_{\mathrm{SL}i}} \tag{B.2}$$

where

$$R'_{\mathrm{SL}i} = \frac{1}{\frac{1}{r_{\mathrm{B}i}} + \frac{1}{\rho'_{\mathrm{SL}i}}}, R''_{\mathrm{SL}i} = \frac{1}{\frac{1}{r_{\mathrm{B}i}} + \frac{1}{\rho''_{\mathrm{SL}i}}} \tag{B.3}$$

$R'_{\mathrm{SL}i}$ and $R''_{\mathrm{SL}i}$ are the relative principal radii of curvature with variables $\rho'_{\mathrm{SL}i}$ and $\rho''_{\mathrm{SL}i}$ representing principal radii of curvature of the SL groove surface at its contact point with ball i; they are given by the eigenvalues of the matrix of the second fundamental form of $\mathbf{S}_{\mathrm{SL}}(\varphi, \gamma)$ as [85]

$$\rho'_{\mathrm{SL}i}, \rho''_{\mathrm{SL}i} = \mathrm{eig}\left(\left[\begin{array}{cc} \frac{\partial^2 \mathbf{S}_{\mathrm{SL}}}{\partial\varphi^2} \cdot \hat{\mathbf{m}}_{\mathrm{SL}i} & \frac{\partial^2 \mathbf{S}_{\mathrm{SL}}}{\partial\varphi\partial\gamma} \cdot \hat{\mathbf{m}}_{\mathrm{SL}i} \\ \frac{\partial^2 \mathbf{S}_{\mathrm{SL}}}{\partial\varphi\partial\gamma} \cdot \hat{\mathbf{m}}_{\mathrm{SL}i} & \frac{\partial^2 \mathbf{S}_{\mathrm{SL}}}{\partial\gamma^2} \cdot \hat{\mathbf{m}}_{\mathrm{SL}i} \end{array}\right]\Bigg|_{\varphi=\varphi_{\mathrm{SL}i}, \gamma=\gamma_{\mathrm{SL}i}}\right) \tag{B.4}$$

where $\hat{\mathbf{m}}_{\mathrm{SL}i}$ represents the groove surface contact normal unit vector. Since the groove surface is parameterized as a multivariate function of real-valued angles, φ and γ, its surface contact normal unit vector can be expressed as a cross product of partial derivatives given by

$$\hat{\mathbf{m}}_{\mathrm{SL}i}=\left.\frac{\dfrac{\partial \mathbf{S}_{\mathrm{SL}}}{\partial \varphi}\times\dfrac{\partial \mathbf{S}_{\mathrm{SL}}}{\partial \gamma}}{\left|\dfrac{\partial \mathbf{S}_{\mathrm{SL}}}{\partial \varphi}\times\dfrac{\partial \mathbf{S}_{\mathrm{SL}}}{\partial \gamma}\right|}\right|_{\varphi=\varphi_{\mathrm{B}i},\gamma=\gamma_{\mathrm{SL}i}} \tag{B.5}$$

Notice that $\rho'_{\mathrm{SL}i}$ and $\rho''_{\mathrm{SL}i}$ can be positive or negative, thus are able to represent convex, concave or saddle-like surfaces. A convex surface is taken to have a positive radius. Continuing with Eq. (B.1), $E_{\mathrm{S,eq}}$, represents the equivalent Young's modulus of the screw, given as functions of Poisson's ratios (ν_{B}, ν_{S}) and Young's moduli (E_{B}, E_{S}) of ball and screw by the equation

$$E_{\mathrm{S,eq}}=\frac{1}{\dfrac{(1-\nu_{\mathrm{B}}^2)}{E_{\mathrm{B}}}+\dfrac{(1-\nu_{\mathrm{S}}^2)}{E_{\mathrm{S}}}} \tag{B.6}$$

Note that the constant $F_1(e_{\mathrm{SL}i})$ in Eq. (B.1) can be regarded as a correction factor for the eccentricity $e_{\mathrm{SL}i}$ of the SL contact ellipse at the contact point; it can be obtained from lookup tables (like the one found in Ref. [22]) as a function of ball radius $r_{\mathrm{B}i}$ and principal radii of curvature $\rho'_{\mathrm{SL}i}$ and $\rho''_{\mathrm{SL}i}$, or, for simplicity, it may be set equal to unity [77].

The maximum contact pressure in the contact area is given by

$$p_{0,\mathrm{SL}i}=F_1(e_{\mathrm{SL}i})^{-2}\left(\frac{6F_{\mathrm{SL}i}E_{\mathrm{S,eq}}^2}{\pi^3\rho_{\mathrm{SL}i,\mathrm{eq}}^2}\right)^{\frac{1}{3}} \tag{B.7}$$

For friction calculation, the length of semi-major axis $a_{\mathrm{SL}i}$ and semi-minor axis $b_{\mathrm{SL}i}$ of the contact region needs to be determined. In order to do that, the ratio between them needs to be calculated first. According to Eq. (4.28) in [77],

$$\frac{R'_{\mathrm{SL}i}}{R''_{\mathrm{SL}i}}-\frac{\left(a_{\mathrm{SL}i}/b_{\mathrm{SL}i}\right)^2\mathbf{E}\left(e_{\mathrm{SL}i}\right)-\mathbf{K}\left(e_{\mathrm{SL}i}\right)}{\mathbf{K}\left(e_{\mathrm{SL}i}\right)-\mathbf{E}\left(e_{\mathrm{SL}i}\right)}=0 \tag{B.8}$$

where $\mathbf{K}(e_{\mathrm{SL}i})$ and $\mathbf{E}(e_{\mathrm{SL}i})$ are complete elliptical integrals of the first and second kind as functions of eccentricity $e_{\mathrm{SL}i}$ which is given as

$$e_{\mathrm{SL}i}=\sqrt{1-\frac{b_{\mathrm{SL}i}^2}{a_{\mathrm{SL}i}^2}} \tag{B.9}$$

It is worth noticing when calculating **K** and **E** using the *ellipke* function in MATLAB®, the input should be square of eccentricity. Given the relative principle radii of curvature $R'_{\mathrm{SL}i}$ and $R''_{\mathrm{SL}i}$, the

ratio $a_{\mathrm{SL}i}/b_{\mathrm{SL}i}$ can be calculated first according to Eq. (B.8). On the other hand, the product of $a_{\mathrm{SL}i}$ and $b_{\mathrm{SL}i}$ can be calculated according to Eq. (4.30) in [77] as

$$\left(a_{\mathrm{SL}i}b_{\mathrm{SL}i}\right)^{1/2} = F_1\left(e_{\mathrm{SL}i}\right)\left(\frac{3F_{\mathrm{SL}i}\rho_{\mathrm{SL}i,\mathrm{eq}}}{4E_{\mathrm{S,eq}}}\right)^{1/3} \tag{B.10}$$

Combine Eqs. (B.8) and (B.10), the semi-major and semi-minor axes can be calculated individually. Given surface geometry and material properties, the semi-major and semi-minor axes are only dependent on contact forces as

$$\begin{aligned} a_{\mathrm{SL}i} &= C_{a\mathrm{SL}i}F_{\mathrm{SL}i}^{2/3}, \\ b_{\mathrm{SL}i} &= C_{b\mathrm{SL}i}F_{\mathrm{SL}i}^{2/3} \end{aligned} \tag{B.11}$$

The values for all the parameters related to Hertzian Contact Theory based on the nominal ball screw parameters in Table 2.1 are shown in Table B.1. Although geometric errors and elastic deformation changes the results, their effect are minimal due to their small quantity. Since nominal ball screw parameters are used, the parameters are not ball number i dependent anymore; there is no difference between SL and SR, NL and NR as well. Thus all the subscripts in Table B.1 are simplified.

Table B.1: Parameters for Hertzian Contact Theory with nominal ball screw parameters

Parameter (Symbol)	**Value [Unit]**
Eccentricity of the contact area for the screw side (e_{S})	0.978
Eccentricity of the contact area for the nut side (e_{N})	0.967
Correction factor for the eccentricity ($F_1(e_{\mathrm{S}})$, $F_1(e_{\mathrm{N}})$)	1
Hertzian Constant of contact deformation for the screw side (C_{S})	1.812×10^{-7} [m/N$^{2/3}$]
Hertzian Constant of contact deformation for the nut side (C_{N})	1.628×10^{-7} [m/N$^{2/3}$]
Hertzian Constant of semi-major axis for the screw side (C_{aS})	7.962×10^{-5} [m/N$^{1/3}$]
Hertzian Constant of semi-minor axis for the screw side (C_{bS})	1.657×10^{-5} [m/N$^{1/3}$]
Hertzian Constant of semi-major axis for the nut side (C_{aN})	8.030×10^{-5} [m/N$^{1/3}$]
Hertzian Constant of semi-minor axis for the nut side (C_{bN})	2.036×10^{-5} [m/N$^{1/3}$]
Principal radius of curvature 1 for the screw side ($\rho_{\mathrm{S}}^{'}$)	−3.137 [mm]
Principal radius of curvature 2 for the screw side ($\rho_{\mathrm{S}}^{''}$)	10.254 [mm]
Principal radius of curvature 1 for the nut side ($\rho_{\mathrm{N}}^{'}$)	−13.141 [mm]

Principal radius of curvature 2 for the nut side ($\rho_{\mathrm{N}}^{''}$)	−3.077 [mm]
Relative principal radius of curvature 1 for the screw side ($R_{\mathrm{S}i}^{'}$)	2.186 [mm]
Relative principal radius of curvature 2 for the screw side ($R_{\mathrm{S}i}^{''}$)	24.254 [mm]
Relative principal radius of curvature 1 for the nut side ($R_{\mathrm{N}i}^{'}$)	3.523 [mm]
Relative principal radius of curvature 2 for the nut side ($R_{\mathrm{N}i}^{''}$)	28.612 [mm]
Equivalent radius of curvature for the screw side ($\rho_{\mathrm{S,eq}}$)	7.281 [mm]
Equivalent radius of curvature for the nut side ($\rho_{\mathrm{N,eq}}$)	10.040 [mm]

Appendix C: Timoshenko Beam Shape Function Matrix

The shape function matrix $\mathbf{T}_{\text{S-}\xi}$ describes the relationship between the generalized displacements/forces of a point along the centerline within the element and generalized displacements/forces acting on the adjacent nodal points. The elements of $\mathbf{T}_{\text{S-}\xi}$ are all functions of ξ, a dimensionless number indicating the relative location of the point within the nodal points. The shape function matrix is given as

$$\mathbf{T}_{\text{S}-\xi}^{\text{T}}(\xi)=\begin{bmatrix} N_{ux1} & 0 & 0 & 0 & N_{ux2} & 0 & N_{ux3} & 0 & 0 & 0 & N_{ux4} & 0 \\ 0 & N_{uy1} & 0 & N_{uy2} & 0 & 0 & 0 & N_{uy3} & 0 & N_{uy4} & 0 & 0 \\ 0 & 0 & N_{uz1} & 0 & 0 & 0 & 0 & 0 & N_{uz2} & 0 & 0 & 0 \\ 0 & N_{\theta x1} & 0 & N_{\theta x2} & 0 & 0 & 0 & N_{\theta x3} & 0 & N_{\theta x4} & 0 & 0 \\ N_{\theta y1} & 0 & 0 & 0 & N_{\theta y2} & 0 & N_{\theta y3} & 0 & 0 & 0 & N_{\theta y4} & 0 \\ 0 & 0 & 0 & 0 & 0 & N_{\theta z1} & 0 & 0 & 0 & 0 & 0 & N_{\theta z2} \end{bmatrix} \tag{C.1}$$

where

$$\begin{aligned} N_{ux1} &= N_{uy1} = \frac{1}{1+\Phi}(2\xi^3 - 3\xi^2 - \Phi\xi + (1+\Phi)), \\ N_{ux2} &= -N_{uy2} = \frac{L_{\text{Elm}}}{1+\Phi}(\xi^3 - (2+\frac{\Phi}{2})\xi^2 + (1+\frac{\Phi}{2})\xi), \\ N_{ux3} &= N_{uy3} = -\frac{1}{1+\Phi}(2\xi^3 - 3\xi^2 - \Phi\xi), \\ N_{ux4} &= -N_{uy4} = \frac{L_{\text{Elm}}}{1+\Phi}(\xi^3 - (1-\frac{\Phi}{2})\xi^2 - \frac{\Phi}{2}\xi), \\ N_{\theta x1} &= -N_{\theta y1} = -N_{\theta x3} = N_{\theta y3} = -\frac{6}{(1+\Phi)L_{\text{Elm}}}(\xi^2 - \xi), \\ N_{\theta x2} &= N_{\theta y2} = \frac{1}{1+\Phi}(3\xi^2 - (4+\Phi)\xi + (1+\Phi)), \\ N_{\theta x4} &= N_{\theta y4} = \frac{1}{1+\Phi}(3\xi^2 - (2-\Phi)\xi), \\ N_{z1} &= N_{\theta z1} = 1-\xi,\ N_{z2} = N_{\theta z2} = \xi,\ \Phi = \frac{12EI}{\kappa GAL_{\text{Elm}}^2} \end{aligned} \tag{C.2}$$

For a circular cross section,

$$\kappa = \frac{6(1+\nu)}{7+6\nu} \tag{C.3}$$

is usually used. In Eq. (C.2), E is the Young's modulus, v is the Poisson's ratio, G is the shear modulus; A is the cross sectional area of the element and I is the second moment of area. In calculating A and I, the indentation of the groove on the cylindrical screw is factored in as an adjustment factor to the outer diameter/radius of screw. It is calculated in the following process. The cross sectional area ΔS of the Gothic-arch-type groove in Figure C.1 can be calculated as

$$\bar{\mathbf{q}}_{\mathrm{B}}(\varphi) = \begin{Bmatrix} \bar{R}_{\mathrm{p}}\cos\varphi \\ \bar{R}_{\mathrm{p}}\sin\varphi \\ \bar{r}_{\mathrm{g}}\varphi \end{Bmatrix} \Delta S = 2\left(\pi r_{\mathrm{G}}^2 \frac{\gamma_2 - \gamma_1}{2\pi} - \frac{1}{2}(r_{\mathrm{G}}\sin\gamma_2 - D_1)\cdot D_2 - \frac{1}{2}(r_{\mathrm{G}}\cos\gamma_1 - D_2)\cdot D_1 \right) \tag{C.4}$$

where

$$\begin{aligned} D_1 &= (r_{\mathrm{G}} - r_{\mathrm{B}})\sin\beta_0, \\ D_2 &= (r_{\mathrm{G}} - r_{\mathrm{B}})\cos\beta_0 + R_{\mathrm{P}} - D_{\mathrm{S,out}}/2, \\ \gamma_1 &= \operatorname{asin}\frac{D_1}{r_{\mathrm{G}}}, \\ \gamma_2 &= \frac{\pi}{2} - \operatorname{asin}\frac{D_2}{r_{\mathrm{G}}} \end{aligned} \tag{C.5}$$

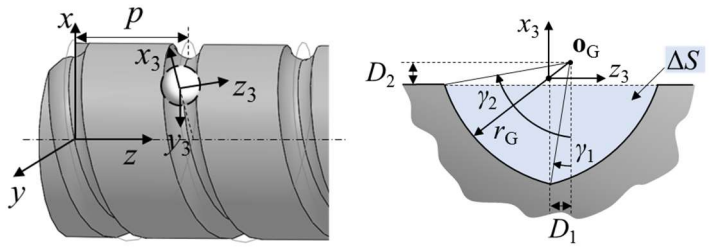

Figure C.1: Cross sectional area of Gothic-arch-type groove

The cross-sectional area is swept along the helix, thus in the span of one lead p, the cut volume is

$$\Delta V = \Delta S \cdot \sqrt{(2\pi R_{\mathrm{P}})^2 + p^2} \tag{C.6}$$

On the other hand, the original volume of the screw shaft in the span of one lead p is

$$V_{\mathrm{org}} = \pi\left(\frac{D_{\mathrm{S,out}}}{2}\right)^2 p \tag{C.7}$$

The factor k_r can be factored in to the outer diameter/radius of screw as

$$k_r = \sqrt{\frac{V_{\text{org}} - \Delta V}{V_{\text{org}}}} \tag{C.8}$$

in calculating A and I of the cross section of ball screw.

Appendix D: Stiffness Matrix of Individual Timoshenko Beam Element

The detail of stiffness matrix of a Timoshenko beam can be found in [86][87]. The global stiffness matrix is assembled from the individual stiffness matrices of each Timoshenko finite element [80], $\mathbf{K}_{\text{Elm}}$, given by

$$\mathbf{K}_{\text{Elm}} = \begin{bmatrix} \mathbf{K} & -\mathbf{K} \\ -\mathbf{K} & \mathbf{K} \end{bmatrix}_{12\times 12} \tag{D.1}$$

with $\mathbf{K}$ defined as

$$\mathbf{K} = \begin{bmatrix} \frac{12EI}{L_{\text{Elm}}^3(1+\varphi)} & 0 & 0 & 0 & \frac{6EI}{L_{\text{Elm}}^2(1+\Phi)} & 0 \\ 0 & \frac{12EI}{L_{\text{Elm}}^3(1+\Phi)} & 0 & -\frac{6EI}{L_{\text{Elm}}^2(1+\Phi)} & 0 & 0 \\ 0 & 0 & \frac{AE}{L_{\text{Elm}}} & 0 & 0 & 0 \\ 0 & -\frac{6EI}{L_{\text{Elm}}^2(1+\Phi)} & 0 & \frac{EI(4+\Phi)}{L_{\text{Elm}}(1+\Phi)} & 0 & 0 \\ \frac{6EI}{L_{\text{Elm}}^2(1+\varphi)} & 0 & 0 & 0 & \frac{6EI}{L_{\text{Elm}}^2(1+\Phi)} & 0 \\ 0 & 0 & 0 & 0 & 0 & \frac{JG}{L_{\text{Elm}}} \end{bmatrix} \tag{D.2}$$

where most of the notations are defined in Appendix C, J is the polar moment of inertia. In calculating J, the indentation of the groove on the cylinder is also factored in as an adjustment factor.

Appendix E: Explicit Jacobian for the Static Load Distribution Model

Explicit Jacobian helps speed up the computation of Eq. (2.26) in the iterative solution process. All the variables and equations are listed here for references. The variables for the static load distribution model are

$$\mathbf{x}=\left\{\cdots,\underbrace{\mathbf{p}_{3\mathrm{B}i}^{\mathrm{T}},\gamma_{\mathrm{SL}i},\gamma_{\mathrm{SR}i},\gamma_{\mathrm{NL}i},\gamma_{\mathrm{NR}i}}_{i^{\mathrm{th}}\text{ ball}},\cdots,\mathbf{U}_{\mathrm{S}}^{\mathrm{T}}\right\}^{\mathrm{T}}_{(6\times N_{\mathrm{B}}+6\times N_{\mathrm{S}})\times 1} \tag{E.1}$$

And the equations for load distribution model are

$$\mathbf{\Phi}(\mathbf{x})=\left\{\begin{array}{c}\vdots\\ \left.\begin{array}{c}\hat{\mathbf{n}}_{\mathrm{SL}i}\cdot\mathbf{t}_{\mathrm{SL}i}\\ \vdots\end{array}\right\}\\ \left.\mathbf{F}_{\mathrm{SL}i}+\mathbf{F}_{\mathrm{SR}i}+\mathbf{F}_{\mathrm{NL}i}+\mathbf{F}_{\mathrm{NR}i}\right\}_{2\times 1}\end{array}\right\}i^{\mathrm{th}}\text{ ball}\\ \vdots\\ \mathbf{K}_{\mathrm{S}}\mathbf{U}_{\mathrm{S}}-\mathbf{F}_{\mathrm{S}}\end{array}\right\}_{(6\times N_{\mathrm{B}}+6\times N_{\mathrm{S}})\times 1}=\mathbf{0} \tag{E.2}$$

where

$$\hat{\mathbf{n}}_{\mathrm{SL}i}=\frac{\mathbf{p}_{3\mathrm{B}i}-\tilde{\mathbf{A}}_{\mathrm{SL}i}}{\left\|\mathbf{p}_{3\mathrm{B}i}-\tilde{\mathbf{A}}_{\mathrm{SL}i}\right\|} \tag{E.3}$$

$$\tilde{\mathbf{A}}_{\mathrm{SL}i}=\mathbf{A}_{\mathrm{SL}i}+\mathbf{d}_{\mathrm{SL}i} \tag{E.4}$$

$$\mathbf{t}_{\mathrm{SL}i}=\frac{\partial\tilde{\mathbf{A}}_{\mathrm{SL}i}}{\partial\gamma_{\mathrm{SL}i}}=\frac{\partial\mathbf{A}_{\mathrm{SL}i}}{\partial\gamma_{\mathrm{SL}i}}+\frac{\partial\mathbf{d}_{\mathrm{SL}i}}{\partial\gamma_{\mathrm{SL}i}} \tag{E.5}$$

$$\mathbf{d}_{\mathrm{SL}i}=\underbrace{\mathbf{T}_{3-2}^{\mathrm{T}}\cdot\left(\mathrm{rot}_z(\varphi_{\mathrm{B}i})\cdot\mathrm{rot}_x(\bar{\alpha})\right)^{-1}}_{\mathbf{T}_{\text{d-u}}}\cdot\mathbf{u}_{\mathrm{SL}i} \tag{E.6}$$

$$\mathbf{u}_{\mathrm{SL}i}=\underbrace{\mathbf{T}_{\xi}\left(\mathbf{r}_{\xi\mathrm{SL}i}\right)\mathbf{T}_{\mathrm{S}-\xi}^{\mathrm{T}}\left(\xi_{\mathrm{SL}i}\right)}_{\mathbf{T}_{\mathrm{S}}\left(\mathbf{r}_{\xi\mathrm{SL}i},\xi_{\mathrm{SL}i}\right)}\left\{\begin{array}{c}\mathbf{U}_{\mathrm{S}j}\\ \mathbf{U}_{\mathrm{S}(j+1)}\end{array}\right\} \tag{E.7}$$

$$\mathbf{r}_{\xi \mathrm{SL}i} = \begin{bmatrix} 1 & 0 & 0 \\ 0 & 1 & 0 \\ 0 & 0 & 0 \end{bmatrix} \cdot \mathbf{S}_{\mathrm{SL}}(\varphi_{\mathrm{B}i}, \gamma_{\mathrm{SL}i}) \tag{E.8}$$

$$\xi_{\mathrm{SL}i} = \frac{\begin{bmatrix} 0 & 0 & 1 \end{bmatrix} \cdot \mathbf{S}_{\mathrm{SL}}(\varphi_{\mathrm{B}i}, \gamma_{\mathrm{SL}i}) - z_j}{L_{\mathrm{Elm}j}} \tag{E.9}$$

$$\mathbf{F}_{\mathrm{SL}i} = F_{\mathrm{SL}i} \cdot \hat{\mathbf{n}}_{\mathrm{SL}i} \tag{E.10}$$

$$F_{\mathrm{SL}i} = \begin{cases} \left(\dfrac{1}{C_{\mathrm{S}}} \delta_{\mathrm{SL}i} \right)^{\frac{3}{2}} & \text{if} \quad \delta_{\mathrm{SL}i} > 0, \delta_{\mathrm{SL}i} = r_{\mathrm{B}i} - \left\| \mathbf{p}_{3\mathrm{B}i} - \tilde{\mathbf{A}}_{\mathrm{SL}i} \right\| \\ 0 & \text{if} \quad \delta_{\mathrm{SL}i} \le 0 \end{cases} \tag{E.11}$$

In Eq. (E.5),

$$\frac{\partial \mathbf{d}_{\mathrm{SL}i}}{\partial \gamma_{\mathrm{SL}i}} = \mathbf{T}_{\mathrm{d\text{-}u}} \cdot \frac{\partial \mathbf{u}_{\mathrm{SL}i}}{\partial \gamma_{\mathrm{SL}i}} \tag{E.12}$$

where

$$\begin{aligned} \frac{\partial \mathbf{u}_{\mathrm{SL}i}}{\partial \gamma_{\mathrm{SL}i}} &= \mathrm{d}\mathbf{T}_{\xi}\left(\frac{\partial \mathbf{r}_{\xi \mathrm{SL}i}}{\partial \gamma_{\mathrm{SL}i}} \right) \cdot \mathbf{T}_{\mathrm{S}-\xi}^{\mathrm{T}}\left(\xi_{\mathrm{SL}i} \right) \begin{Bmatrix} \mathbf{U}_{\mathrm{S}j} \\ \mathbf{U}_{\mathrm{S}(j+1)} \end{Bmatrix} + \mathbf{T}_{\xi}\left(\mathbf{r}_{\xi \mathrm{SL}i} \right) \cdot \frac{\partial \left(\mathbf{T}_{\mathrm{S}-\xi}^{\mathrm{T}}\left(\xi_{\mathrm{SL}i} \right) \begin{Bmatrix} \mathbf{U}_{\mathrm{S}j} \\ \mathbf{U}_{\mathrm{S}(j+1)} \end{Bmatrix} \right)}{\partial \gamma_{\mathrm{SL}i}}, \\ \frac{\partial \mathbf{r}_{\xi \mathrm{SL}i}}{\partial \gamma_{\mathrm{SL}i}} &= \begin{bmatrix} 1 & 0 & 0 \\ 0 & 1 & 0 \\ 0 & 0 & 0 \end{bmatrix} \cdot \frac{\partial \mathbf{S}_{\mathrm{SL}i}}{\partial \gamma_{\mathrm{SL}i}}, \\ \frac{\partial \xi_{\mathrm{SL}i}}{\partial \gamma_{\mathrm{SL}i}} &= \frac{\begin{bmatrix} 0 & 0 & 1 \end{bmatrix} \cdot \dfrac{\partial \mathbf{S}_{\mathrm{SL}i}}{\partial \gamma_{\mathrm{SL}i}}}{L_{\mathrm{Elm}j}}, \\ \frac{\partial \left(\mathbf{T}_{\mathrm{S}-\xi}^{\mathrm{T}}\left(\xi_{\mathrm{SL}i} \right) \begin{Bmatrix} \mathbf{U}_{\mathrm{S}j} \\ \mathbf{U}_{\mathrm{S}(j+1)} \end{Bmatrix} \right)}{\partial \gamma_{\mathrm{SL}i}} &= \frac{\partial \mathbf{T}_{\mathrm{S}-\xi}^{\mathrm{T}}\left(\xi_{\mathrm{SL}i} \right)}{\partial \xi_{\mathrm{SL}i}} \frac{\partial \xi_{\mathrm{SL}i}}{\partial \gamma_{\mathrm{SL}i}} \begin{Bmatrix} \mathbf{U}_{\mathrm{S}j} \\ \mathbf{U}_{\mathrm{S}(j+1)} \end{Bmatrix} \end{aligned} \tag{E.13}$$

where

$$\mathrm{d}\mathbf{T}_{\xi}(\mathbf{r}) = \begin{bmatrix} \mathbf{0}_{3\times 3} & -\mathbf{D}(\mathbf{r}) \end{bmatrix} \tag{E.14}$$

The Jacobian is calculated for each item with respect to each variable in the following equations.

$$\frac{\partial\left(\hat{\mathbf{n}}_{\mathrm{SL}i}\cdot\mathbf{t}_{\mathrm{SL}i}\right)}{\partial\mathbf{p}_{3\mathrm{B}i}}=\hat{\mathbf{n}}_{\mathrm{SL}i}{}^{\mathrm{T}}\cdot\underbrace{\frac{\partial\mathbf{t}_{\mathrm{SL}i}}{\partial\mathbf{p}_{3\mathrm{B}i}}}_{\mathbf{0}}+\mathbf{t}_{\mathrm{SL}i}{}^{\mathrm{T}}\cdot\frac{\partial\hat{\mathbf{n}}_{\mathrm{SL}i}}{\partial\mathbf{p}_{3\mathrm{B}i}}=\mathbf{t}_{\mathrm{SL}i}{}^{\mathrm{T}}\cdot\frac{\partial\hat{\mathbf{n}}_{\mathrm{SL}i}}{\partial\mathbf{p}_{3\mathrm{B}i}},$$

$$\frac{\partial\hat{\mathbf{n}}_{\mathrm{SL}i}}{\partial\mathbf{p}_{3\mathrm{B}i}}=\frac{\partial\hat{\mathbf{n}}_{\mathrm{SL}i}}{\partial\left(\mathbf{p}_{3\mathrm{B}i}-\tilde{\mathbf{A}}_{\mathrm{SL}i}\right)}=\frac{1}{\left\|\mathbf{p}_{3\mathrm{B}i}-\tilde{\mathbf{A}}_{\mathrm{SL}i}\right\|}\left(\mathbf{I}-\left(\mathbf{p}_{3\mathrm{B}i}-\tilde{\mathbf{A}}_{\mathrm{SL}i}\right)\left(\mathbf{p}_{3\mathrm{B}i}-\tilde{\mathbf{A}}_{\mathrm{SL}i}\right)^{\mathrm{T}}\right) \tag{E.15}$$

$$\frac{\partial\left(\hat{\mathbf{n}}_{\mathrm{SL}i}\cdot\mathbf{t}_{\mathrm{SL}i}\right)}{\partial\gamma_{\mathrm{SL}i}}=\hat{\mathbf{n}}_{\mathrm{SL}i}{}^{\mathrm{T}}\cdot\frac{\partial\mathbf{t}_{\mathrm{SL}i}}{\partial\gamma_{\mathrm{SL}i}}+\mathbf{t}_{\mathrm{SL}i}{}^{\mathrm{T}}\cdot\frac{\partial\hat{\mathbf{n}}_{\mathrm{SL}i}}{\partial\gamma_{\mathrm{SL}i}},$$

$$\frac{\partial\mathbf{t}_{\mathrm{SL}i}}{\partial\gamma_{\mathrm{SL}i}}=\frac{\partial^2\tilde{\mathbf{A}}_{\mathrm{SL}i}}{\partial\gamma_{\mathrm{SL}i}{}^2}=\frac{\partial^2\mathbf{A}_{\mathrm{SL}i}}{\partial\gamma_{\mathrm{SL}i}{}^2}+\frac{\partial^2\mathbf{d}_{\mathrm{SL}i}}{\partial\gamma_{\mathrm{SL}i}{}^2},$$

$$\frac{\partial^2\mathbf{d}_{\mathrm{SL}i}}{\partial\gamma_{\mathrm{SL}i}{}^2}=\mathbf{T}_{\mathrm{d\text{-}u}}\cdot\frac{\partial^2\mathbf{u}_{\mathrm{SL}i}}{\partial\gamma_{\mathrm{SL}i}{}^2}$$

$$\frac{\partial^2\mathbf{u}_{\mathrm{SL}i}}{\partial\gamma_{\mathrm{SL}i}{}^2}=\mathrm{d}\mathbf{T}_{\xi}\left(\frac{\partial^2\mathbf{r}_{\xi\mathrm{SL}i}}{\partial\gamma_{\mathrm{SL}i}{}^2}\right)\cdot\mathbf{T}_{\mathrm{S}-\xi}^{\mathrm{T}}\left(\xi_{\mathrm{SL}i}\right)\begin{Bmatrix}\mathbf{U}_{\mathrm{S}j}\\ \mathbf{U}_{\mathrm{S}(j+1)}\end{Bmatrix}+2\mathrm{d}\mathbf{T}_{\xi}\left(\frac{\partial\mathbf{r}_{\xi\mathrm{SL}i}}{\partial\gamma_{\mathrm{SL}i}}\right)\frac{\partial\left(\mathbf{T}_{\mathrm{S}-\xi}^{\mathrm{T}}\left(\xi_{\mathrm{SL}i}\right)\begin{Bmatrix}\mathbf{U}_{\mathrm{S}j}\\ \mathbf{U}_{\mathrm{S}(j+1)}\end{Bmatrix}\right)}{\partial\gamma_{\mathrm{SL}i}}$$
$$+\mathbf{T}_{\xi}\left(\mathbf{r}_{\xi\mathrm{SL}i}\right)\cdot\frac{\partial^2\left(\mathbf{T}_{\mathrm{S}-\xi}^{\mathrm{T}}\left(\xi_{\mathrm{SL}i}\right)\begin{Bmatrix}\mathbf{U}_{\mathrm{S}j}\\ \mathbf{U}_{\mathrm{S}(j+1)}\end{Bmatrix}\right)}{\partial\gamma_{\mathrm{SL}i}{}^2},$$

$$\frac{\partial^2\mathbf{r}_{\xi\mathrm{SL}i}}{\partial\gamma_{\mathrm{SL}i}{}^2}=\begin{bmatrix}1&0&0\\0&1&0\\0&0&0\end{bmatrix}\cdot\frac{\partial^2\mathbf{S}_{\mathrm{SL}i}}{\partial\gamma_{\mathrm{SL}i}{}^2}, \tag{E.16}$$

$$\frac{\partial^2\left(\mathbf{T}_{\mathrm{S}-\xi}^{\mathrm{T}}\left(\xi_{\mathrm{SL}i}\right)\begin{Bmatrix}\mathbf{U}_{\mathrm{S}j}\\ \mathbf{U}_{\mathrm{S}(j+1)}\end{Bmatrix}\right)}{\partial\gamma_{\mathrm{SL}i}{}^2}=\frac{\partial^2\mathbf{T}_{\mathrm{S}-\xi}^{\mathrm{T}}\left(\xi_{\mathrm{SL}i}\right)}{\partial\xi_{\mathrm{SL}i}{}^2}\left(\frac{\partial\xi_{\mathrm{SL}i}}{\partial\gamma_{\mathrm{SL}i}}\right)^2\begin{Bmatrix}\mathbf{U}_{\mathrm{S}j}\\ \mathbf{U}_{\mathrm{S}(j+1)}\end{Bmatrix}$$
$$+\frac{\partial\mathbf{T}_{\mathrm{S}-\xi}^{\mathrm{T}}\left(\xi_{\mathrm{SL}i}\right)}{\partial\xi_{\mathrm{SL}i}}\frac{\partial^2\xi_{\mathrm{SL}i}}{\partial\gamma_{\mathrm{SL}i}{}^2}\begin{Bmatrix}\mathbf{U}_{\mathrm{S}j}\\ \mathbf{U}_{\mathrm{S}(j+1)}\end{Bmatrix}$$

$$\frac{\partial^2\xi_{\mathrm{SL}i}}{\partial\gamma_{\mathrm{SL}i}{}^2}=\frac{\begin{bmatrix}0&0&1\end{bmatrix}\cdot\frac{\partial^2\mathbf{S}_{\mathrm{SL}i}}{\partial\gamma_{\mathrm{SL}i}{}^2}}{L_{\mathrm{Elm}j}},$$

$$\frac{\partial\hat{\mathbf{n}}_{\mathrm{SL}i}}{\partial\gamma_{\mathrm{SL}i}}=\frac{\partial\hat{\mathbf{n}}_{\mathrm{SL}i}}{\partial\left(\mathbf{p}_{3\mathrm{B}i}-\tilde{\mathbf{A}}_{\mathrm{SL}i}\right)}(-\mathbf{I})\frac{\partial\tilde{\mathbf{A}}_{\mathrm{SL}i}}{\partial\gamma_{\mathrm{SL}i}}=\frac{\partial\hat{\mathbf{n}}_{\mathrm{SL}i}}{\partial\left(\mathbf{p}_{3\mathrm{B}i}-\tilde{\mathbf{A}}_{\mathrm{SL}i}\right)}(-\mathbf{I})\mathbf{t}_{\mathrm{SL}i}$$

$$
\begin{aligned}
&\frac{\partial\left(\hat{\mathbf{n}}_{\mathrm{SL}i}\cdot\mathbf{t}_{\mathrm{SL}i}\right)}{\partial\mathbf{U}_{\mathrm{S}}}=\hat{\mathbf{n}}_{\mathrm{SL}i}{}^{\mathrm{T}}\cdot\frac{\partial\mathbf{t}_{\mathrm{SL}i}}{\partial\mathbf{U}_{\mathrm{S}}}+\mathbf{t}_{\mathrm{SL}i}{}^{\mathrm{T}}\cdot\frac{\partial\hat{\mathbf{n}}_{\mathrm{SL}i}}{\partial\mathbf{U}_{\mathrm{S}}},\\
&\frac{\partial\mathbf{t}_{\mathrm{SL}i}}{\partial\mathbf{U}_{\mathrm{S}}}=\frac{\partial^2\tilde{\mathbf{A}}_{\mathrm{SL}i}}{\partial\mathbf{U}_{\mathrm{S}}\partial\gamma_{\mathrm{SL}i}}=\underbrace{\frac{\partial^2\mathbf{A}_{\mathrm{SL}i}}{\partial\mathbf{U}_{\mathrm{S}}\partial\gamma_{\mathrm{SL}i}}}_{\mathbf{0}}+\frac{\partial^2\mathbf{d}_{\mathrm{SL}i}}{\partial\mathbf{U}_{\mathrm{S}}\partial\gamma_{\mathrm{SL}i}}=\frac{\partial^2\mathbf{d}_{\mathrm{SL}i}}{\partial\mathbf{U}_{\mathrm{S}}\partial\gamma_{\mathrm{SL}i}},\\
&\frac{\partial^2\mathbf{d}_{\mathrm{SL}i}}{\partial\mathbf{U}_{\mathrm{S}}\partial\gamma_{\mathrm{SL}i}}=\mathbf{T}_{\mathrm{d\text{-}u}}\cdot\frac{\partial^2\mathbf{u}_{\mathrm{SL}i}}{\partial\mathbf{U}_{\mathrm{S}}\partial\gamma_{\mathrm{SL}i}},\\
&\frac{\partial^2\mathbf{u}_{\mathrm{SL}i}}{\partial\left[\mathbf{U}_{\mathrm{S}j};\mathbf{U}_{\mathrm{S}(j+1)}\right]\partial\gamma_{\mathrm{SL}i}}=\mathrm{d}\mathbf{T}_{\xi}\left(\frac{\partial\mathbf{r}_{\xi\mathrm{SL}i}}{\partial\gamma_{\mathrm{SL}i}}\right)\cdot\mathbf{T}_{\mathrm{S}-\xi}^{\mathrm{T}}\left(\xi_{\mathrm{SL}i}\right)+\mathbf{T}_{\xi}\left(\mathbf{r}_{\xi\mathrm{SL}i}\right)\cdot\frac{\partial\mathbf{T}_{\mathrm{S}-\xi}^{\mathrm{T}}\left(\xi_{\mathrm{SL}i}\right)}{\partial\xi_{\mathrm{SL}i}}\frac{\partial\xi_{\mathrm{SL}i}}{\partial\gamma_{\mathrm{SL}i}}\\
&\frac{\partial\hat{\mathbf{n}}_{\mathrm{SL}i}}{\partial\mathbf{U}_{\mathrm{S}}}=\frac{\partial\hat{\mathbf{n}}_{\mathrm{SL}i}}{\partial\left(\mathbf{p}_{3\mathrm{B}i}-\tilde{\mathbf{A}}_{\mathrm{SL}i}\right)}\cdot\left(-\mathbf{I}\right)\cdot\frac{\partial\tilde{\mathbf{A}}_{\mathrm{SL}i}}{\partial\mathbf{U}_{\mathrm{S}}},\\
&\frac{\partial\tilde{\mathbf{A}}_{\mathrm{SL}i}}{\partial\mathbf{U}_{\mathrm{S}}}=\underbrace{\frac{\partial\mathbf{A}_{\mathrm{SL}i}}{\partial\mathbf{U}_{\mathrm{S}}}}_{\mathbf{0}}+\frac{\partial\mathbf{d}_{\mathrm{SL}i}}{\partial\mathbf{U}_{\mathrm{S}}}=\frac{\partial\mathbf{d}_{\mathrm{SL}i}}{\partial\mathbf{U}_{\mathrm{S}}},\\
&\frac{\partial\mathbf{d}_{\mathrm{SL}i}}{\partial\mathbf{U}_{\mathrm{S}}}=\mathbf{T}_{\mathrm{d\text{-}u}}\cdot\frac{\partial\mathbf{u}_{\mathrm{SL}i}}{\partial\mathbf{U}_{\mathrm{S}}},\\
&\frac{\partial\mathbf{u}_{\mathrm{SL}i}}{\partial\left[\mathbf{U}_{\mathrm{S}j};\mathbf{U}_{\mathrm{S}(j+1)}\right]}=\mathbf{T}_{\xi}\left(\mathbf{r}_{\xi\mathrm{SL}i}\right)\mathbf{T}_{\mathrm{S}-\xi}^{\mathrm{T}}\left(\xi_{\mathrm{SL}i}\right)
\end{aligned}
\tag{E.17}
$$

and

$$
\begin{aligned}
&\frac{\partial\left(\hat{\mathbf{n}}_{\mathrm{SL}i}\cdot P_{\mathrm{SL}i}\right)}{\partial\mathbf{p}_{3\mathrm{B}i}}=\frac{\partial\hat{\mathbf{n}}_{\mathrm{SL}i}}{\partial\mathbf{p}_{3\mathrm{B}i}}\cdot P_{\mathrm{SL}i}+\hat{\mathbf{n}}_{\mathrm{SL}i}\cdot\frac{\partial P_{\mathrm{SL}i}}{\partial\mathbf{p}_{3\mathrm{B}i}},\\
&\frac{\partial P_{\mathrm{SL}i}}{\partial\mathbf{p}_{3\mathrm{B}i}}=\frac{\partial P_{\mathrm{SL}i}}{\partial\left(\mathbf{p}_{3\mathrm{B}i}-\tilde{\mathbf{A}}_{\mathrm{SL}i}\right)}=\frac{3}{2}\left(\frac{r_{\mathrm{B}i}-\left\|\mathbf{p}_{\mathrm{B}i}-\tilde{\mathbf{A}}_{\mathrm{SL}i}\right\|}{C_{\mathrm{S}}}\right)^{1/2}\left(-\frac{1}{C_{\mathrm{S}}}\right)\frac{\left(\mathbf{p}_{3\mathrm{B}i}-\tilde{\mathbf{A}}_{\mathrm{SL}i}\right)^{\mathrm{T}}}{\left\|\mathbf{p}_{3\mathrm{B}i}-\tilde{\mathbf{A}}_{\mathrm{SL}i}\right\|}
\end{aligned}
\tag{E.18}
$$

$$
\begin{aligned}
&\frac{\partial\left(\hat{\mathbf{n}}_{\mathrm{SL}i}\cdot P_{\mathrm{SL}i}\right)}{\partial\gamma_{\mathrm{SL}i}}=\frac{\partial\hat{\mathbf{n}}_{\mathrm{SL}i}}{\partial\gamma_{\mathrm{SL}i}}\cdot P_{\mathrm{SL}i}+\hat{\mathbf{n}}_{\mathrm{SL}i}\cdot\frac{\partial P_{\mathrm{SL}i}}{\partial\gamma_{\mathrm{SL}i}},\\
&\frac{\partial P_{\mathrm{SL}i}}{\partial\gamma_{\mathrm{SL}i}}=\frac{\partial P_{\mathrm{SL}i}}{\partial\left(\mathbf{p}_{3\mathrm{B}i}-\tilde{\mathbf{A}}_{\mathrm{SL}i}\right)}\cdot\left(-\mathbf{I}\right)\cdot\frac{\partial\tilde{\mathbf{A}}_{\mathrm{SL}i}}{\partial\gamma_{\mathrm{SL}i}}=\frac{\partial P_{\mathrm{SL}i}}{\partial\left(\mathbf{p}_{3\mathrm{B}i}-\tilde{\mathbf{A}}_{\mathrm{SL}i}\right)}\cdot\left(-\mathbf{I}\right)\cdot\mathbf{t}_{\mathrm{SL}i}
\end{aligned}
\tag{E.19}
$$

$$
\begin{aligned}
&\frac{\partial\left(\hat{\mathbf{n}}_{\mathrm{SL}i}\cdot P_{\mathrm{SL}i}\right)}{\partial\mathbf{U}_{\mathrm{S}}}=\frac{\partial\hat{\mathbf{n}}_{\mathrm{SL}i}}{\partial\mathbf{U}_{\mathrm{S}}}\cdot P_{\mathrm{SL}i}+\hat{\mathbf{n}}_{\mathrm{SL}i}\cdot\frac{\partial P_{\mathrm{SL}i}}{\partial\mathbf{U}_{\mathrm{S}}},\\
&\frac{\partial P_{\mathrm{SL}i}}{\partial\mathbf{U}_{\mathrm{S}}}=\frac{\partial P_{\mathrm{SL}i}}{\partial\left(\mathbf{p}_{\mathrm{B}i}-\tilde{\mathbf{A}}_{\mathrm{SL}i}\right)}\cdot\left(-\mathbf{I}\right)\cdot\frac{\partial\tilde{\mathbf{A}}_{\mathrm{SL}i}}{\mathbf{U}_{\mathrm{S}}}=\frac{\partial P_{\mathrm{SL}i}}{\partial\left(\mathbf{p}_{\mathrm{B}i}-\tilde{\mathbf{A}}_{\mathrm{SL}i}\right)}\cdot\left(-\mathbf{I}\right)\cdot\frac{\partial\mathbf{d}_{\mathrm{SL}i}}{\mathbf{U}_{\mathrm{S}}}
\end{aligned}
\tag{E.20}
$$

Finally

$$\frac{\partial\left(\mathbf{K}_{\mathrm{S}}\mathbf{U}_{\mathrm{S}}-\mathbf{F}_{\mathrm{S}}\right)}{\partial\mathbf{p}_{3\mathrm{B}i}}=-\frac{\partial\mathbf{F}_{\mathrm{S}}}{\partial\mathbf{p}_{3\mathrm{B}i}} \tag{E.21}$$

$$\frac{\partial\left(\mathbf{K}_{\mathrm{S}}\mathbf{U}_{\mathrm{S}}-\mathbf{F}_{\mathrm{S}}\right)}{\partial\gamma_{\mathrm{SL}i}}=-\frac{\partial\mathbf{F}_{\mathrm{S}}}{\partial\gamma_{\mathrm{SL}i}} \tag{E.22}$$

$$\frac{\partial\left(\mathbf{K}_{\mathrm{S}}\mathbf{U}_{\mathrm{S}}-\mathbf{F}_{\mathrm{S}}\right)}{\partial\mathbf{U}_{\mathrm{S}}}=\mathbf{K}_{\mathrm{S}}-\frac{\partial\mathbf{F}_{\mathrm{S}}}{\partial\mathbf{U}_{\mathrm{S}}} \tag{E.23}$$

The basic derivatives used in the process are

$$\frac{\partial\hat{\mathbf{n}}}{\partial\mathbf{n}}=\frac{1}{\|\mathbf{n}\|}\left(\mathbf{I}-\hat{\mathbf{n}}\cdot\hat{\mathbf{n}}^{\mathrm{T}}\right),\hat{\mathbf{n}}=\frac{\mathbf{n}}{\|\mathbf{n}\|} \tag{E.24}$$

$$\frac{\partial\left(\mathbf{m}\cdot\mathbf{n}\right)}{\partial\mathbf{x}}=\mathbf{m}^{\mathrm{T}}\cdot\left(\frac{\partial\mathbf{n}}{\partial\mathbf{x}}\right)+\mathbf{n}^{\mathrm{T}}\cdot\left(\frac{\partial\mathbf{m}}{\partial\mathbf{x}}\right) \tag{E.25}$$

$$\frac{\partial\|\mathbf{n}\|}{\partial\mathbf{n}}=\frac{\mathbf{n}^{\mathrm{T}}}{\|\mathbf{n}\|} \tag{E.26}$$

Appendix F: Relative Velocity Field at the Contact Areas in Linear Ball Bearing and Ball Screw

The relative velocity field at the BR, TR and TL contact areas in linear ball bearing are formulated as

$$\begin{aligned}\begin{Bmatrix}\left(\Delta\mathbf{v}_{\mathrm{BR,B}}\right)_{\mathrm{BR},x}\\ \left(\Delta\mathbf{v}_{\mathrm{BR,B}}\right)_{\mathrm{BR},z}\end{Bmatrix}&=\begin{Bmatrix}\omega_{\mathrm{BR}}\left(-d_{\mathrm{BR}}+z_{\mathrm{BR}}\right)\\ \omega_{\mathrm{BR}}\left(c_{\mathrm{BR}}-x_{\mathrm{BR}}\right)\end{Bmatrix}\\ &=\begin{Bmatrix}\left(-\omega_x\sin\beta_{\mathrm{BR}}+\omega_y\cos\beta_{\mathrm{BR}}\right)z_{\mathrm{BR}}\\ v_{\mathrm{B}}-\left(\omega_x\cos\beta_{\mathrm{BR}}+\omega_y\sin\beta_{\mathrm{BR}}\right)R_{\mathrm{B}}-\left(-\omega_x\sin\beta_{\mathrm{BR}}+\omega_y\cos\beta_{\mathrm{BR}}\right)x_{\mathrm{BR}}\end{Bmatrix}\end{aligned} \tag{F.1}$$

$$\begin{aligned}\begin{Bmatrix}\left(\Delta\mathbf{v}_{\mathrm{TR,B}}\right)_{\mathrm{TR},x}\\ \left(\Delta\mathbf{v}_{\mathrm{TR,B}}\right)_{\mathrm{TR},z}\end{Bmatrix}&=\begin{Bmatrix}\omega_{\mathrm{TR}}\left(-d_{\mathrm{TR}}+z_{\mathrm{TR}}\right)\\ \omega_{\mathrm{TR}}\left(c_{\mathrm{TR}}-x_{\mathrm{TR}}\right)\end{Bmatrix}\\ &=\begin{Bmatrix}\left(-\omega_x\sin\beta_{\mathrm{TR}}-\omega_y\cos\beta_{\mathrm{TR}}\right)z_{\mathrm{TR}}\\ v_{\mathrm{B}}-v+\left(\omega_x\cos\beta_{\mathrm{TR}}-\omega_y\sin\beta_{\mathrm{TR}}\right)R_{\mathrm{B}}-\left(-\omega_x\sin\beta_{\mathrm{TR}}-\omega_y\cos\beta_{\mathrm{TR}}\right)x_{\mathrm{TR}}\end{Bmatrix},\end{aligned} \tag{F.2}$$

$$\begin{aligned}\begin{Bmatrix}\left(\Delta\mathbf{v}_{\mathrm{TL,B}}\right)_{\mathrm{TL},x}\\ \left(\Delta\mathbf{v}_{\mathrm{TL,B}}\right)_{\mathrm{TL},z}\end{Bmatrix}&=\begin{Bmatrix}\omega_{\mathrm{TL}}\left(-d_{\mathrm{TL}}+z_{\mathrm{TL}}\right)\\ \omega_{\mathrm{TL}}\left(c_{\mathrm{TL}}-x_{\mathrm{TL}}\right)\end{Bmatrix}\\ &=\begin{Bmatrix}\left(\omega_x\sin\beta_{\mathrm{TL}}-\omega_y\cos\beta_{\mathrm{TL}}\right)z_{\mathrm{TL}}\\ v_{\mathrm{B}}-v+\left(\omega_x\cos\beta_{\mathrm{TL}}+\omega_y\sin\beta_{\mathrm{TL}}\right)R_{\mathrm{B}}-\left(\omega_x\sin\beta_{\mathrm{TL}}-\omega_y\cos\beta_{\mathrm{TL}}\right)x_{\mathrm{TL}}\end{Bmatrix}\end{aligned} \tag{F.3}$$

The relative velocity field at the SR, NR and NL contact areas in ball screw are formulated as

$$\left(\Delta\mathbf{v}_{\mathrm{SR,B}}\right)_{\mathrm{SR}}=\begin{Bmatrix}\left(\Delta\mathbf{v}_{\mathrm{SR,B}}\right)_{\mathrm{SR},y}\\ \left(\Delta\mathbf{v}_{\mathrm{SR,B}}\right)_{\mathrm{SR},z}\end{Bmatrix}=\begin{Bmatrix}\omega_{\mathrm{SR}}\left(c_{\mathrm{SR}}+z_{\mathrm{SR}}\right)\\ \omega_{\mathrm{SR}}\left(d_{\mathrm{SR}}-y_{\mathrm{SR}}\right)\end{Bmatrix}$$

$$=\begin{Bmatrix}\dfrac{L^2-4\pi^2R_{\mathrm{B}}\bar{R}_{\mathrm{P}}\cos\beta_{\mathrm{SR}}}{2\pi L}\omega_{\mathrm{B}}-\left(\cos\beta_{\mathrm{SR}}\omega_z+\sin\beta_{\mathrm{SR}}\omega_x\right)R_{\mathrm{B}}+\omega_{\mathrm{SR}}z_{\mathrm{SR}}\\ R_{\mathrm{B}}\omega_y+\dfrac{R_{\mathrm{B}}\bar{p}}{L}\omega_{\mathrm{B}}-\omega_{\mathrm{SR}}y_{\mathrm{SR}}\end{Bmatrix},\tag{F.4}$$

$$\omega_{\mathrm{SR}}=\frac{2\pi\bar{R}_{\mathrm{P}}}{L}\omega_{\mathrm{B}}\sin\beta_{\mathrm{SR}}-\cos\beta_{\mathrm{SR}}\omega_x+\sin\beta_{\mathrm{SR}}\omega_z$$

$$\left(\Delta\mathbf{v}_{\mathrm{NR}}\right)_{\mathrm{NR}}=\begin{Bmatrix}\left(\Delta\mathbf{v}_{\mathrm{NR,B}}\right)_{\mathrm{NR},y}\\ \left(\Delta\mathbf{v}_{\mathrm{NR,B}}\right)_{\mathrm{NR},z}\end{Bmatrix}=\begin{Bmatrix}\omega_{\mathrm{NR}}\left(c_{\mathrm{NR}}+z_{\mathrm{NR}}\right)\\ \omega_{\mathrm{NR}}\left(d_{\mathrm{NR}}-y_{\mathrm{NR}}\right)\end{Bmatrix}$$

$$=\begin{Bmatrix}\dfrac{L^2+4\pi^2R_{\mathrm{B}}\bar{R}_{\mathrm{P}}\cos\beta_{\mathrm{NR}}}{2\pi L}\left(\omega_{\mathrm{B}}-\omega_{\mathrm{N}}\right)+\left(\cos\beta_{\mathrm{NR}}\omega_z-\sin\beta_{\mathrm{NR}}\omega_x\right)R_{\mathrm{B}}+\omega_{\mathrm{NR}}z_{\mathrm{NR}}\\ R_{\mathrm{B}}\omega_y+\dfrac{R_{\mathrm{B}}\bar{p}}{L}\left(\omega_{\mathrm{B}}-\omega_{\mathrm{N}}\right)-\omega_{\mathrm{NR}}y_{\mathrm{NR}}\end{Bmatrix},\tag{F.5}$$

$$\omega_{\mathrm{NR}}=\frac{2\pi\bar{R}_{\mathrm{P}}}{L}\left(\omega_{\mathrm{B}}-\omega_{\mathrm{N}}\right)\sin\beta_{\mathrm{NR}}+\omega_x\cos\beta_{\mathrm{NR}}+\omega_z\sin\beta_{\mathrm{NR}}$$

$$\left(\Delta\mathbf{v}_{\mathrm{NL}}\right)_{\mathrm{NL}}=\begin{Bmatrix}\left(\Delta\mathbf{v}_{\mathrm{NL,B}}\right)_{\mathrm{NL},y}\\ \left(\Delta\mathbf{v}_{\mathrm{NL,B}}\right)_{\mathrm{NL},z}\end{Bmatrix}=\begin{Bmatrix}\omega_{\mathrm{NL}}\left(c_{\mathrm{NL}}-z_{\mathrm{NL}}\right)\\ \omega_{\mathrm{NL}}\left(d_{\mathrm{NL}}+y_{\mathrm{NL}}\right)\end{Bmatrix}$$

$$=\begin{Bmatrix}\dfrac{L^2+4\pi^2R_{\mathrm{B}}\bar{R}_{\mathrm{P}}\cos\beta_{\mathrm{NL}}}{2\pi L}\left(\omega_{\mathrm{B}}-\omega_{\mathrm{N}}\right)+\left(\cos\beta_{\mathrm{NL}}\omega_z+\sin\beta_{\mathrm{NL}}\omega_x\right)R_{\mathrm{B}}-\omega_{\mathrm{NL}}z_{\mathrm{NL}}\\ R_{\mathrm{B}}\omega_y+\dfrac{R_{\mathrm{B}}\bar{p}}{L}\left(\omega_{\mathrm{B}}-\omega_{\mathrm{N}}\right)+\omega_{\mathrm{NL}}y_{\mathrm{NL}}\end{Bmatrix},\tag{F.6}$$

$$\omega_{\mathrm{NL}}=\frac{2\pi\bar{R}_{\mathrm{P}}}{L}\left(\omega_{\mathrm{B}}-\omega_{\mathrm{N}}\right)\sin\beta_{\mathrm{NL}}-\omega_x\cos\beta_{\mathrm{NL}}+\omega_z\sin\beta_{\mathrm{NL}}$$

Appendix G: The Magnitude of $\Delta\eta_i$ for the Linearized Region of Frictional Force

The magnitude of angular deviation $\Delta\eta_i$ in Eq. (3.34) is decomposed as

$$\left|\Delta\eta_i\right| = \left|\frac{c_i}{R_{\mathrm{B}}}\right| = \left|\frac{c_i}{a_i}\right| \cdot \left|\frac{a_i}{R_{\mathrm{B}}}\right| \tag{G.1}$$

In order for linear approximation of frictional force to be valid, $|c_i/a_i|<0.5$ has to be satisfied as shown in Figure 3.11. The ratio of the semi-major axis a_i to the ball radius R_{B} depends on the normal contact load F_i (or maximum contact stress σ_i over the contact area) and the conformity ratio of the groove. Figure G.1 plots a_i/R_{B} as a function of σ_i with four typical conformity ratios of ball bearings. The plot is cut off at maximum allowable stress of 1554 MPa for Hertzian contact, which is 4.2 times of typical carbon steel's yield strength (370 MPa) according to [88].

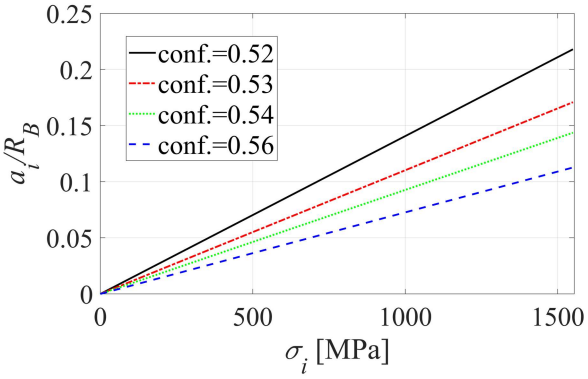

Figure G.1: The ratio of the semi-major axis a_i to the ball radius R_{B}

The maximum value of a_i/R_{B} is 0.218 achieved at the maximum allowable stress with conf.=0.52. The higher the conformity ratio, the smaller a_i/R_{B}; a_i/R_{B} also decreases with contact stress (or contact load). In the worst case scenario, $|\Delta\eta_i|<0.5\times0.218=0.109$, which is equivalent of 6.25°.

Bibliography

[1] Hong, S., and Tong, V.-C., 2016, "Rolling-Element Bearing Modeling : A Review," Int. J. Precis. Eng. Manuf., **17**(12), pp. 1729–1749.

[2] Abele, E., Altintas, Y., and Brecher, C., 2010, "Machine Tool Spindle Units," CIRP Ann. - Manuf. Technol., **59**(2), pp. 781–802.

[3] Cao, Y., and Altintas, Y., 2004, "A General Method for the Modeling of Spindle-Bearing Systems," J. Mech. Des., **126**(6), pp. 1089–1104.

[4] Altintas, Y., Verl, A., Brecher, C., Uriarte, L., and Pritschow, G., 2011, "Machine Tool Feed Drives," CIRP Ann. - Manuf. Technol., **60**(2), pp. 779–796.

[5] García Márquez, F. P., Tobias, A. M., Pinar Pérez, J. M., and Papaelias, M., 2012, "Condition Monitoring of Wind Turbines: Techniques and Methods," Renew. Energy, **46**, pp. 169–178.

[6] Azevedo, H. D. M. de, Araújo, A. M., and Bouchonneau, N., 2016, "A Review of Wind Turbine Bearing Condition Monitoring: State of the Art and Challenges," Renew. Sustain. Energy Rev., **56**, pp. 368–379.

[7] Aguirrebeitia, J., Plaza, J., Abasolo, M., and Vallejo, J., 2013, "General Static Load-Carrying Capacity of Four-Contact-Point Slewing Bearings for Wind Turbine Generator Actuation Systems," Wind Energy, **16**, pp. 759–774.

[8] Bertolaso, R., Cheikh, M., Barranger, Y., Dupré, J.-C., Germaneau, A., and Doumalin, P., 2014, "Experimental and Numerical Study of the Load Distribution in a Ball-Screw System," J. Mech. Sci. Technol., **28**(4), pp. 1411–1420.

[9] Qiao, G., Liu, G., Shi, Z., Wang, Y., Ma, S., and Lim, T. C., 2018, "A Review of Electromechanical Actuators for More/All Electric Aircraft Systems," Proc. Inst. Mech. Eng. Part C J. Mech. Eng. Sci., **232**(22), pp. 4128–4151.

[10] Tung, S. C., and Mcmillan, M. L., 2004, "Automotive Tribology Overview of Current Advances and Challenges for the Future," Tribiology Int., **37**, pp. 517–536.

[11] Baeuml, M., Dobre, F., Hochmuth, H., Kraus, M., Krehmer, H., Langer, R., and Reif, D.,

2014, *The Chassis of the Future*, Springer Fachmedien Wiesbaden.

[12] Cao, H., Zhang, X., and Chen, X., 2017, "The Concept and Progress of Intelligent Spindles: A Review," Int. J. Mach. Tools Manuf., **112**, pp. 21–52.

[13] Fernandes, C. M. C. G., Martins, R. C., and Seabra, J. H. O., 2013, "Friction Torque of Thrust Ball Bearings Lubricated with Wind Turbine Gear Oils," Tribiology Int., **58**, pp. 47–54.

[14] Zhang, D., Lin, B., Kirli, A., and Okwudire, C., 2017, "Reduction of Steering Effort in the Event of EPAS Failure Using Differential Braking Assisted Steering," SAE Int. J. Transp. Saf., **5**, pp. 227–233.

[15] Kim, J. H., and Song, J. B., 2002, "Control Logic for an Electric Power Steering System Using Assist Motor," Mechatronics, **12**(3), pp. 447–459.

[16] Robert Bosch Automotive Steering GmbH, 2015, "Servolectric Electromechanical Steering System for a Dynamic Driving Experience and Highly Automated Functions."

[17] Srivastava, P., Karle, M. L., Karle, U. S., and Deshpande, A. A., 2015, "Development of Electrical Power Assisted Steering (EPAS) Considering Safety and Reliability Aspects as per ISO 26262," *SAE Technical Paper*.

[18] Gao, X. H., Huang, X. D., Wang, H., and Chen, J., 2011, "Modelling of Ball – Raceway Contacts in a Slewing Bearing with Non-Linear Springs," Proc. Inst. Mech. Eng. Part C J. Mech. Eng. Sci., **225**(4), pp. 827–831.

[19] Aithal, S., Prasad, N. S., and Shunmugam, M. S., 2016, "Effect of Manufacturing Errors on Load Distribution in Large Diameter Slewing Bearings of Fast Breeder Reactor Rotatable Plugs," Proc. Inst. Mech. Eng. Part C J. Mech. Eng. Sci., **230**(9), pp. 1449–1460.

[20] Biehl, S., Lüthje, H., Bandorf, R., and Sick, J., 2006, "Multifunctional Thin Film Sensors Based on Amorphous Diamond-like Carbon for Use in Tribological Applications," Thin Solid Films, **515**(3), pp. 1171–1175.

[21] Biehl, S., Staufenbiel, S., Recknagel, S., Denkena, B., and Bertram, O., 2012, "Thin Film Sensors for Condition Monitoring in Ball Screw Drives," *1st Joint International Symposium on System-Integrated Intelligence*, pp. 27–29.

[22] Mohring, H.-C., and Bertram, O., 2012, "Integrated Autonomous Monitoring of Ball Screw Drives," CIRP Ann. Technol., **61**(1), pp. 355–358.

[23] Papadopoulos, G. A., 2005, “Experimental Study of the Load Distribution in Bearings by the Method of Caustics and the Photoelasticity Method,” J. Strain Anal. Eng. Des., **40**(4), pp. 357–365.

[24] Jones, A. B., 1960, “A General Theory for Elastically Constrained Ball and Radial Roller Bearings under Arbitrary Load and Speed Conditions,” J. Basic Eng., **82**(2), pp. 309–320.

[25] Smolnicki, T., and Rusin, E., 2007, “Superelement-Based Modeling of Load Distribution in Large-Size Slewing Bearings,” J. Mech. Des., **129**(4), pp. 459–463.

[26] Daidié, A., Chaib, Z., and Ghosn, A., 2008, “3D Simplified Finite Elements Analysis of Load and Contact Angle in a Slewing Ball Bearing,” J. Mech. Des., **130**(8), p. 082601.

[27] Potočnik, R., Göncz, P., and Glodež, S., 2013, “Static Capacity of a Large Double Row Slewing Ball Bearing with Predefined Irregular Geometry,” Mech. Mach. Theory, **64**, pp. 67–79.

[28] Sun, W., Kong, X., Wang, B., and Li, X., 2015, “Statics Modeling and Analysis of Linear Rolling Guideway Considering Rolling Balls Contact,” Proc. Inst. Mech. Eng. Part C J. Mech. Eng. Sci., **229**(1), pp. 168–179.

[29] Jones, A. B., 1959, “Ball Motion and Sliding Friction in Ball Bearings,” J. Basic Eng., **81**(3), p. 1.

[30] Liao, N. T., and Lin, J. F., 2001, “A New Method for the Analysis of Deformation and Load in a Ball Bearing with Variable Contact Angle,” J. Mech. Des., **123**(2), pp. 304–312.

[31] Zupan, S., and Prebil, I., 2001, “Carrying Angle and Carrying Capacity of a Large Single Row Ball Bearing as a Function of Geometry Parameters of the Rolling Contact and the Supporting Structure Stiffness,” Mech. Mach. Theory, **36**(10), pp. 1087–1103.

[32] Amasorrain, J. I., Sagartzazu, X., and Damián, J., 2003, “Load Distribution in a Four Contact-Point Slewing Bearing,” Mech. Mach. Theory, **38**(6), pp. 479–496.

[33] Kunc, R., and Prebil, I., 2004, “Numerical Determination of Carrying Capacity of Large Rolling Bearings,” J. Mater. Process. Technol., **155**, pp. 1696–1703.

[34] Lazovic, T., and Mitrovic, R., 2008, “Mathematical Model of Load Distribution in Rolling Bearing,” FME Trans., **36**(4), pp. 189–196.

[35] DIN, and ISO, 2011, *DIN ISO 3408-4*.

[36] Ricci, M. C., 2009, “Internal Loading Distribution in Statically Loaded Ball Bearings Subjected to an Eccentric Thrust Load,” Math. Probl. Eng., **2009**.

[37] Zhang, J., Fang, B., Hong, J., and Zhu, Y., 2017, "Effect of Preload on Ball-Raceway Contact State and Fatigue Life of Angular Contact Ball Bearing," Tribiology Int., **114**(April), pp. 365–372.

[38] Huang, H.-T. T., and Ravani, B., 1997, "Contact Stress Analysis in Ball Screw Mechanism Using the Tubular Medial Axis Representation of Contacting Surfaces," J. Mech. Des., **119**(1), p. 8.

[39] Cuttino, J. F., Dow, T. a., and Knight, B. F., 1997, "Analytical and Experimental Identification of Nonlinearities in a Single-Nut, Preloaded Ball Screw," J. Mech. Des., **119**(1), p. 15.

[40] Wei, C. C., and Lin, J. F., 2003, "Kinematic Analysis of the Ball Screw Mechanism Considering Variable Contact Angles and Elastic Deformations," J. Mech. Des., **125**(4), pp. 717–733.

[41] Shimoda, H., Ando, Y., and Izawa, M., 1976, "Study on the Load Distribution in the Ball Screw (1st Report)," J. Japan Soc. Precis. Eng., **41**(10), pp. 954–959.

[42] Yoshida, T., Tozaki, Y., and Matsumoto, S., 2003, "Study on Load Distribution and Ball Motion of Ball Screw," J. Japanese Soc. Tribol., **48**(8), pp. 659–666.

[43] Mei, X., Tsutsumi, M., Tao, T., and Sun, N., 2003, "Study on the Load Distribution of Ball Screws with Errors," Mech. Mach. Theory, **38**(11), pp. 1257–1269.

[44] Xu, S., Yao, Z., Sun, Y., and Shen, H., 2014, "Load Distribution of Ball Screw with Consideration of Contact Angle Variation and Geometry Errors," *Proceedings of the ASME 2014 International Mechanical Engineering Congress and Exposition (IMECE2014)*, pp. 1–7.

[45] Wei, C. C., Lin, J. F., and Horng, J. H., 2009, "Analysis of a Ball Screw with a Preload and Lubrication," Tribol. Int., **42**(11–12), pp. 1816–1831.

[46] Slocum, A. H., 1992, *Precision Machine Design*, Prentice-Hall, Inc.

[47] Okwudire, C. E., and Altintas, Y., 2009, "Hybrid Modeling of Ball Screw Drives With Coupled Axial, Torsional, and Lateral Dynamics," J. Mech. Des., **131**(7), p. 071002.

[48] Okwudire, C. E., 2011, "Improved Screw–Nut Interface Model for High-Performance Ball Screw Drives," J. Mech. Des., **133**(4), p. 041009.

[49] Okwudire, C. E., 2012, "Reduction of Torque-Induced Bending Vibrations in Ball Screw-Driven Machines via Optimal Design of the Nut," J. Mech. Des., **134**(11), p. 111008.

[50] Bosch Rexroth AG, 2009, “Precision Ball Screw Assemblies Catalogue,” **3301**(704).

[51] Majda, P., 2012, “Modeling of Geometric Errors of Linear Guideway and Their Influence on Joint Kinematic Error in Machine Tools,” Precis. Eng., **36**(3), pp. 369–378.

[52] Halpin, J. D., and Tran, A. N., 2016, “An Analytical Model of Four-Point Contact Rolling Element Ball Bearings,” J. Tribol., **138**(3), p. 031404.

[53] Hamrock, B. J., 1975, “Ball Motion and Sliding Friction in an Arched Outer Race Ball Bearing,” J. Lubr. Technol., **97**(2), pp. 202–210.

[54] Harris, T. A., and Kotzalas, M. N., 2006, *Advanced Concepts of Bearing Technology: Rolling Bearing Analysis*, CRC Press.

[55] Leblanc, A., and Nelias, D., 2007, “Ball Motion and Sliding Friction in a Four-Contact-Point Ball Bearing,” J. Tribol., **129**(4), pp. 801–808.

[56] Joshi, A., Kachhia, B., Kikkari, H., Sridhar, M., and Nelias, D., 2015, “Running Torque of Slow Speed Two-Point and Four-Point Contact Bearings,” Lubricants, **3**(2), pp. 181–196.

[57] Lin, M. C., Ravani, B., and Velinsky, S. a., 1994, “Kinematics of the Ball Screw Mechanism,” J. Mech. Des., **116**(3), pp. 849–855.

[58] Xu, N., Tang, W., Chen, Y., Bao, D., and Guo, Y., 2015, “Modeling Analysis and Experimental Study for the Friction of a Ball Screw,” Mech. Mach. Theory, **87**, pp. 57–69.

[59] Heras, I., Aguirrebeitia, J., Abasolo, M., and Plaza, J., 2017, “Friction Torque in Four-Point Contact Slewing Bearings : Applicability and Limitations of Current Analytical Formulations,” Tribol. Int., **115**, pp. 59–69.

[60] Lin, B., Duan, M., Okwudire, C. E., and Wou, J. S., 2018, “A Simplified Analytical Model for Rolling/Sliding Behavior and Friction in Four-Point-Contact Ball Bearings and Screws,” *Proceedings of the ASME 2017 International Mechanical Engineering Congress and Exposition*, pp. 1–9.

[61] Zhou, C. G., Feng, H. T., Chen, Z. T., and Ou, Y., 2016, “Correlation between Preload and No-Load Drag Torque of Ball Screws,” Int. J. Mach. Tools Manuf., **102**, pp. 35–40.

[62] Shimoda, H., and Izawa, M., 1987, “Characteristics of Oscillatory Ball Screws (1st Report, Oscillatory Friction Torque of Preloaded Ball Screws with Shim Plates),” Trans. Japan Soc. Mech. Eng. Ser. C., **53**(491), pp. 1495--1499.

[63] Ohta, H., Hanaoka, G., and Ueki, Y., 2017, “Sticking of a Linear-Guideway Type

Recirculating Ball Bearing," J. Tribol., **139**(3), p. 031103.

[64] Guddei, B., and Ahmed, S. I. U., 2013, "Rolling Friction of Single Balls in a Flat-Ball-Flat-Contact as a Function of Surface Roughness," Tribol. Lett., **51**(2), pp. 219–226.

[65] Cross, R., 2016, "Coulomb's Law for Rolling Friction," Am. J. Phys., **84**(3), pp. 221–230.

[66] Pettersson, U., and Jacobson, S., 2003, "Influence of Surface Texture on Boundary Lubricated Sliding Contacts," Tribol. Int., **36**(11), pp. 857–864.

[67] Ohta, H., Duenas, G. A. G., and Ueki, Y., 2019, "Reduction of Sticking in a Linear-Guideway Type Recirculating Ball Bearing," J. Tribol., **141**(2), pp. 1–6.

[68] Logan, W., 2018, "The Benefits of Caged Balls : Boosted Lifetime and Reduced Noise," Mach. Des. [Online]. Available: https://www.machinedesign.com/motion-control/benefits-caged-balls-boosted-lifetime-and-reduced-noise.

[69] Lin, B., and Okwudire, C. E., 2016, "Low-Order Contact Load Distribution Model for Ball Nut Assemblies," SAE Int. J. Passeng. Cars-Mechanical Syst., **9**(2).

[70] Lin, B., Okwudire, C. E., and Wou, J. S., 2018, "Low Order Static Load Distribution Model for Ball Screw Mechanisms Including Effects of Lateral Deformation and Geometric Errors," J. Mech. Des., **140**(2), p. 022301.

[71] Lin, B., Duan, M., Okwudire, C. E., and Wou, J. S., 2017, "A Simplified Analytical Model of Rolling/Sliding Behavior and Friction in Four-Point-Contact Ball Bearings and Screws," *Proceedings of the ASME 2017 International Mechanical Engineering Congress and Exposition*, p. V04AT05A054-V04AT05A054.

[72] Lin, B., Duan, M., Okwudire, C. E., and Wou, J. S., 2018, "An Improved Analytical Model of Friction and Ball Motion in Linear Ball Bearings - With Application to Ball-to-Ball Contact Prediction," *Proceedings of the ASME 2018 International Mechanical Engineering Congress and Exposition*.

[73] Lin, B., Duan, M., Okwudire, C., and Wou, J., 2018, "Analytical and Low-Order Numerical Modeling of Ball-to-Ball Contact Friction in Linear Ball Bearings and Ball Screws," J. Tribol.

[74] Lin, B., Wou, J., and Okwudire, C., 2019, "Modeling Static Load Distribution and Friction of Ball Bearings and BNAs : Towards Understanding the ' Stick-Slip ' of Rack EPAS," *SAE 2019 World Congress*, pp. 1–7.

[75] ISO, and DIN, 2011, *DIN ISO 3408-1*.

[76] Feng, H.-T., Wang, Y.-L., Li, C.-M., and Tao, W.-J., 2011, "An Automatic Measuring Method and System Using a Light Curtain for the Thread Profile of a Ballscrew," Meas. Sci. Technol., **22**(8), p. 085106.

[77] Johnson, K. L., 2003, *Contact Mechanics*, Cambridge University Press.

[78] Mei, X., Tsutsumi, M., Tao, T., and Sun, N., 2003, "Study on the Load Distribution of Ball Screws with Errors," Mech. Mach. Theory, **38**(11), pp. 1257–1269.

[79] Zaeh, M. F., Oertli, T., and Milberg, J., 2004, "Finite Element Modelling of Ball Screw Feed Drive Systems," CIRP Ann. - Manuf. Technol., **53**(1), pp. 289–292.

[80] Hutton, D., 2003, *Fundamentals of Finite Element Analysis*, McGraw-Hill.

[81] NSK Ltd., 2003, "NSK Precision Machine Components," NSK Cat., **No. E3162D**.

[82] ANSYS Inc., 2010, *Introduction to Contact: ANSYS Mechanical Structural Nonlinearities*.

[83] ANSYS Inc., 2013, *ANSYS Meshing User's Guide*.

[84] Lin, B., and Okwudire, C. E., 2016, "Low-Order Contact Load Distribution Model for Ball Nut Assemblies," *SAE 2016 World Congress*, Detroit.

[85] Spivak, M., 1979, *A Comprehensive Introduction to Differential Geometry Volume 1*, Publish or Perish, Inc.

[86] Yokoyama, T., 1990, "Vibrations of a Hanging Timoshenko Beam under Gravity," J. Sound Vib., **141**(2), pp. 245–258.

[87] Petyt, M., 1969, "Theory of Matrix Structural Analysis," J. Sound Vib., **10**(2), pp. 358–359.

[88] Kogut, L., and Etsion, I., 2002, "Elastic-Plastic Contact Analysis of a Sphere and a Rigid Flat," J. Appl. Mech., **69**(5), pp. 657–662.